Study on three-dimensional structures of impurity ion distribution in stochastic magnetic field layer of LHD using high spatial resolution EUV spectroscopy

ZHANG Hongming

Doctor of Philosophy

Department of Fusion Science
School of Physical Sciences
SOKENDAI (The Graduate University for Advanced Studies)

2016 School Year

Abstract

Impurity spectroscopy in magnetically confined toroidal plasmas for fusion research is essentially important not only for the plasma performance improvement but also for the impurity transport study. Extreme ultraviolet (EUV) spectroscopy in wavelength range of 10 to 500 Å is a unique tool for studying the impurity transport in both core and edge plasma regions. In Large Helical Device (LHD), a stochastic magnetic layer called "ergodic layer" intrinsically exists in the edge region outside the last closed flux surface (LCFS), which makes a specific character of the LHD plasma. The magnetic field structure in the ergodic layer is entirely three-dimensional (3-D) and resultant impurity spectral intensities emitted from the layer become fully non-uniform along poloidal and toroidal directions. In order to study the impurity transport in the ergodic layer, therefore, two-dimensional (2-D) diagnostics is at least necessary for estimation of the 3-D structure of impurity line emissions. For the purpose a space-resolved EUV spectrometer has been developed in LHD to observe the 2-D distribution of edge impurity line emissions in the wavelength range of 30 – 650 Å by horizontally scanning the optical axis of the spectrometer.

The 2-D distribution was successfully obtained from a steady phase in electron cyclotron heating (ECH) and ion cyclotron range of heating (ICRF) discharges with long pulse duration ($\tau_d \geq 10$ s). However, the performance of EUV spectrometer system was not sufficient for short pulse discharges ($\tau_d \sim 3$ s) with high-power neutral beam injection (NBI) due to a long time duration required for the horizontal scan. The space-resolved EUV spectrometer has been then upgraded through the present thesis work for 2-D distribution measurement applicable to the short pulse NBI discharge by newly installing a high-frame-rate charge-coupled detector (CCD) and increasing the horizontal scanning speed. As a result, a rapid 2-D distribution measurement system is completed for the high-power NBI discharge with improved horizontal spatial resolution. The 2-D distribution of impurity line emissions is usually measured twice at upper- and lower-half plasma positions using two identical discharges. A full vertical 2-D distribution is thus obtained by superimposing the two 2-D distributions. In this process, a signal normalization method is applied based on a temporal behavior of intensity signal from another EUV spectrometer with high time resolution of 5 ms to delete temporal and shot-by-shot intensity variations between the two discharges. A 0.5 μm polyethylene terephthalate (PET) filter is also installed in front of an entrance slit of the space-resolved EUV spectrometer to eliminate high-energy neutral particles originated in neutral beams for heating, since a lot of large spike noises are created in the CCD signal. The spike noise can be almost deleted with the filter, while it is specially enhanced in low-density NBI discharges due to the long slowing down time of neutral beams. Typical examples of the 2-D distribution with improved quality are

presented for several impurity species.

Poloidal distribution of the local emissivity is evaluated for various impurity species in the plasma edge including ergodic layer by analyzing the 2-D distribution with magnetic flux surfaces extended outside the LCFS based on a three-dimensional (3-D) equilibrium code, i.e., VMEC. In the present study, the poloidal emissivity distribution is analyzed for CIV, CVI, FeXV and FeXVIII with different ionization energies. A non-uniform poloidal distribution is clearly observed for such impurity ions staying at different plasma radii. It is then experimentally confirmed that the poloidal distribution becomes gradually uniform as the radial location of the impurity ions changes from the ergodic layer toward the plasma core. In addition, the non-uniform poloidal distribution of the CIV local emissivity is analyzed with a 3-D edge plasma transport code, EMC3-EIRENE. The result shows a good agreement with the experimentally evaluated distribution.

In LHD the plasma detachment has been steadily operated without external impurity gas feed by supplying the resonance magnetic perturbation (RMP) field with m/n = 1/1 mode at outwardly shifted plasma axis position of R_{ax} = 3.90 m where the magnetic resonance exists in the stochastic magnetic field layer. Since carbon released from graphite divertor plates is a dominant intrinsic impurity in high-density LHD discharges, the radiation from carbon ions also seems to play an important role in the plasma detachment, in particular, on the effective edge plasma cooling triggering the detachment. Therefore, the partial radiation power at each ionization stage in carbon ions of C^{2+} to C^{5+}, i.e., $P_{rad}(C^{q+})$, is analyzed from the absolute line intensity of CIII–CVI resonance lines measured by vacuum ultraviolet (VUV) and EUV spectrometers for attached and detached plasmas. For the analysis, the ratio of $P_{rad}(C^{q+})$ to resonance line intensity is calculated in advance as a function of the electron temperature using ADAS atomic code. The electron temperature at the radial location where the impurity ion exists is determined by the intensity ratio method. As a result, it is found that the radiation from C^{3+} ions existing near $\iota/2\pi = 1$ radial position in the ergodic layer largely increases during the plasma detachment phase against the total radiation power, P_{rad}, i.e., $P_{rad}(C^{3+})/P_{rad} \sim 40\%$, while it is only 8% to the P_{rad} in the attached plasma. Therefore, it is concluded that the $P_{rad}(C^{3+})$ plays a key role in the enhancement of edge radiation during the RMP-assisted detached plasma.

An effect of m/n = 1/1 island on the vertical profile of carbon line emissions is studied at the RMP-assisted plasma detachment phase. The vertical profile is measured at both the top edge near island O-point and the bottom edge near island X-point in the horizontally elongated plasma cross section of LHD plasmas. It is found from the analysis that the radial position of the top and bottom edge peaks appeared in both the CIII and CIV vertical profiles shifts radially inside after the detachment transition and the change in the radial position is different between the top and bottom edges, i.e., 8

cm inside at the top and 2 cm inside at the bottom. The differently changed positional shifts between the top and bottom edge peaks indicate a clear evidence of newly appeared m/n = 1/1 magnetic island in the plasma edge during the plasma detachment. The result concludes that a large magnetic island can be created by the RMP field during the plasma detachment, even if the magnetic resonance exists in the stochastic magnetic field layer.

Impurity behaviors in attached and RMP-assisted detached plasmas are studied by analyzing the vertical profile and 2-D distribution of edge impurity carbon emissions of CIII to CVI. For the purpose the 3-D structure of carbon ion distributions is analyzed based on the 2-D distribution measurement taking into account the magnetic field structure in stochastic magnetic field layer. It is found that the CIII and CIV emissions located in the ergodic layer are drastically increased near the island O-point and in the vicinity of both the inboard and outboard X-points during the RMP-assisted detachment phase, while those emissions are enhanced only in the vicinity of the outboard X-point in attached plasmas without RMP. The result clearly indicates an enhancement of edge carbon radiation and a considerable change in the magnetic field lines connecting to the divertor plates during the detachment phase. These obvious changes seen in the carbon emissions can be also supported from a big change in the edge temperature profile during the detachment phase, i.e., temperature flattening suggesting the appearance of a large magnetic island. The measured carbon distribution from attached plasmas without RMP is also analyzed with the EMC3-EIRENE. It is found that the cross-field particle diffusion of carbon ions is much larger (more than 5 times) than that of the bulk ions in the R_{ax} = 3.90 m configuration. At least the larger Gyro radius of partially ionized carbon ions may contribute to the enhanced diffusion coefficient. The simulations are also discussed for the carbon distribution in the RMP-assisted detached plasma.

Contents

List of Figures

List of Tables

Chapter 1

Introduction

1.1 Impurity in fusion plasmas

In the present fusion research, the magnetic confinement based on toroidal devices is one of the most promising solutions for the future fusion reactor. In the magnetic confinement fusion device, e.g., tokamak and stellarator, the following fusion reaction is used [1];

$$D^+ + T^+ \rightarrow {}^4He^{2+} + n + 17.6\ \text{MeV}, \tag{1.1}$$

where D is the deuterium, T is the tritium, ^{4}He the fusion product so-called alpha particle and n the neutron. This reaction gives the total energy output of 17.6 MeV, in which the kinetic energy of alpha particle, 3.5 MeV, is basically used for the maintenance of steady state discharge of the fusion plasma and the neutron energy, 14.1 MeV, can be used for output electric energy. In order to realize the fusion reactor, the fusion plasma has to be sufficiently hot and dense and the plasma energy in the toroidal device has to be confined as long as possible [2]. These critical conditions on the plasma performance necessary for the fusion reactor can be quantified by the fusion triple product, $n_i\tau_E T_i$. The fusion triple product has to satisfy the following condition well known as Lawson criterion:

$$n_i\tau_E T_i > 5\times10^{21}\ \text{m}^{-3}\ \text{s keV}, \tag{1.2}$$

where, n_i is the density of ions, T_i the temperature of ions and τ_E the energy confinement time. Over the past half century, many tokamaks and stellarators have been constructed for the fusion research, and the value of $n_i\tau_E T_i$ has been significantly improved. Some

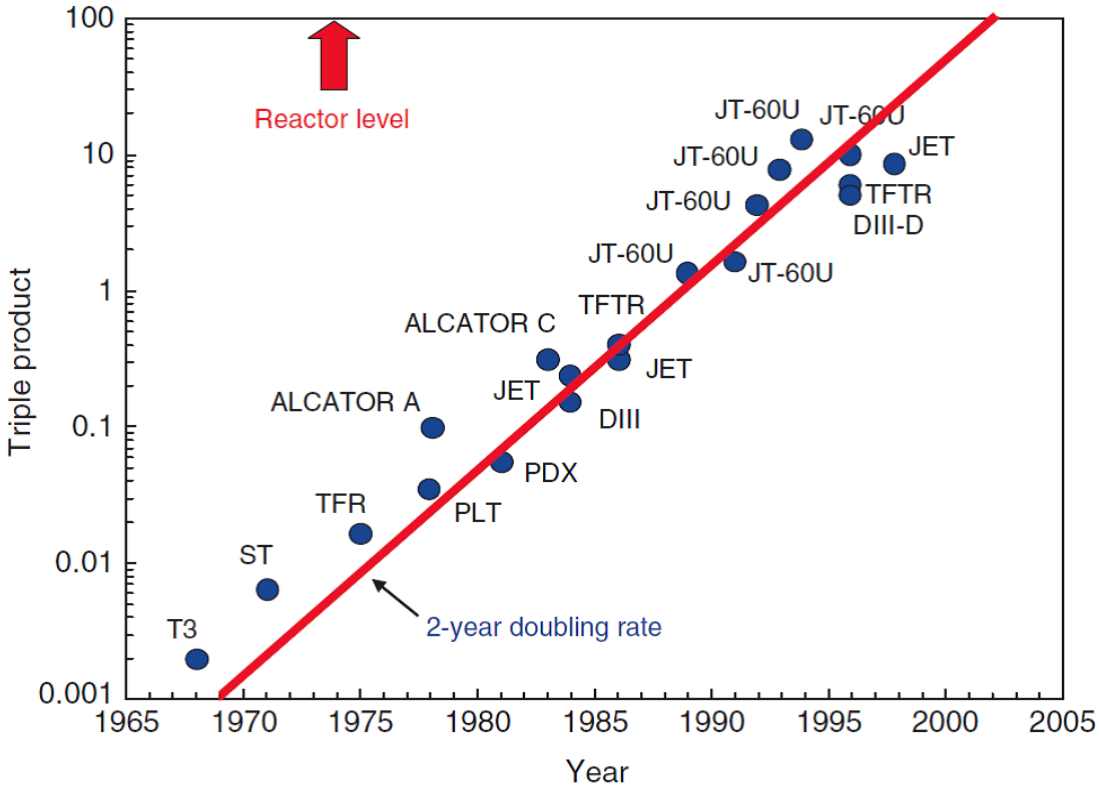

Fig. 1.1 Increase in the triple product $n_i\tau_E T_i$ against year. The points are labeled with the names of tokamaks [2].

of these are plotted in Fig. 1.1 as a function of year [2]. It is very clear from the figure that the fusion triple product has increased over 10,000 times during past four decades.

In loss term of the confined energy, on the other hand, radiation loss mainly originating in the impurity line emissions always plays an important role. The impurity in fusion plasmas is generally produced by an interaction between edge plasmas and plasma facing components in the vacuum vessel, e.g., divertor plates, first wall and radio-frequency antennas [3]. The impurity in fusion plasmas is usually divided into two groups, i.e., light and heavy impurities according to the atomic mass. The heavy impurity like iron and tungsten frequently break the energy balance through the huge radiation loss in the plasma core region since the radiation loss power is a function of the atomic number. The light impurity like carbon and oxygen, on the other hand, easily dilute the density of fuel ions and selectively cool down the edge plasma. In recent tokamak and stellarators, the content of heavy impurities is sufficiently reduced due to the usage of divertor configuration and the adoption of carbon first wall. The content of light impurities, in particular, oxygen, is also sufficiently suppressed by high-temperature baking of the plasma facing components and the execution of effective wall

conditioning. As a result, the carbon is uniquely remained as an intrinsic dominant impurity in recent fusion plasmas. In plasma experiments, however, the impurity is frequently introduced into the plasma for diagnostic purpose and active control of divertor heat flux [4]. It is discussed in Section 1.3 in detail.

1.2 Edge magnetic field structure in LHD

1.2.1 Ergodic layer in LHD

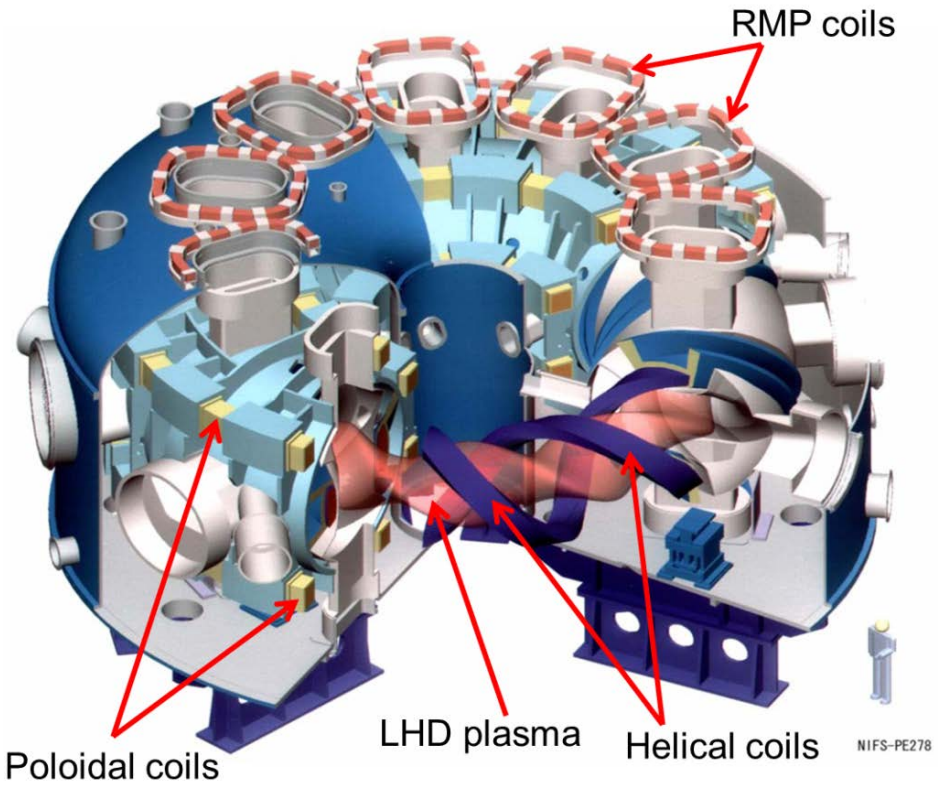

Fig. 1.2 Bird's-eye view of helical coils, poloidal coils, RMP coils and toroidal plasma shape in LHD.

The objectives of Large Helical Device (LHD) with superconducting coils are to conduct the fusion research in the world and to make deeper understanding on the plasma physics in the toroidal device in addition to the production of high-performance plasmas [5]. A bird's-eye view of LHD is illustrated in Fig. 1.2. The magnetic surface with elliptical shape for plasma confinement is created by a pair of superconducting helical coils with poloidal and toroidal pitch numbers of l = 2 and n = 10, respectively.

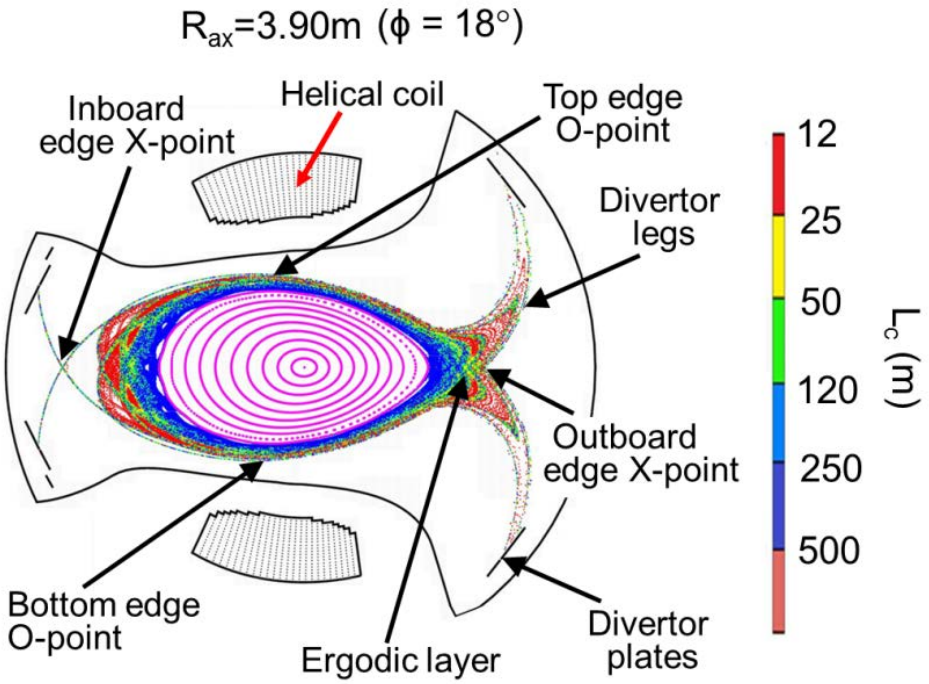

Fig. 1.3 Connection length L_c in ergodic layer at magnetic axis position of R_{ax} = 3.90 m.

The divertor configuration is intrinsically formed with relatively long divertor legs connecting to divertor plates. Three pairs of superconducting poloidal coils are used for cancelling the stray magnetic field, controlling the plasma position and shaping the plasma poloidal cross section. The magnetic axis position, R_{ax}, can be changed between R_{ax} = 3.50 m and 4.10 m in general operation. The averaged plasma minor radius, <a>, and plasma volume, V_p, defined by the last closed flux surface (LCFS) are a function of magnetic axis position. The best confinement is obtained at R_{ax} = 3.60 m where the plasma radius and the plasma volume take the maximum values, i.e., <a> = 0.64 m and V_p = 30 m^3.

A stochastic magnetic field layer called “ergodic layer” is formed outside the LCFS due to the presence of higher-order Fourier components in the magnetic field created by the helical coils. The presence of the ergodic layer surrounding the core plasma specially characterizes the LHD plasma in which the transport character is entirely different from that in scrape-off layer (SOL) of tokamaks. The magnetic field structure and resultant plasma parameters in the ergodic layer become fully three-dimensional (3-D) because the magnetic field connection length, L_c, poloidally and poloidally has a different distribution. The connection lengths in the ergodic layer at a horizontally elongated plasma cross section (ϕ = 18°) are shown in Figs. 1.3 with plasma axis positions of R_{ax} = 3.90 m. It indicates that the value of L_c varies in a wide

range of $10 \leq L_c \leq 2000$ m in the ergodic layer. Besides, two edge X-points appear at the inboard and outboard sides. In the present study, those are called the "inboard edge X-point" and the "outboard edge X-point". In contrast with this, two positions closed to the helical coil are called the "top edge O-point" and the "bottom edge O-point". The magnetic field line called "divertor leg" starting from the vicinity of the edge X-points is directly connected to the divertor plates. It is clear in the figures that the thickness of the ergodic layer, λ_{erg}, varies with poloidal angle, e.g., thicker at the edge X-points and thinner at the top and bottom O-points [6].

1.2.2 RMP field in LHD

Additional ten pairs of normal conducting coils are installed at the top and bottom of LHD to create a large magnetic island with m/n = 1/1 poloidal and toroidal modes in the plasma edge. The coil system originally used for the local island divertor experiment to demonstrate an efficient particle exhaust [7] is now called resonant magnetic perturbation (RMP) coils. The RMP coils at the top are indicated in Fig. 1.2. The width of m/n=1/1 RMP island can be enlarged so largely, e.g., 10 cm, at the maximum RMP coil current. In the present study the RMP coil current is kept constant at nearly the maximum value during the discharge. The m/n = 1/1 island structure formed by the RMP coil is discussed in Chapter 6 in detail.

1.3 Plasma detachment

1.3.1 High heat flux on divertor in next-generation fusion devices

International Thermonuclear Experimental Reactor (ITER) is an international joint nuclear fusion research project, which is a unique experimental device for fusion reactor feasibility study. The first operation is now scheduled in the middle of 2020s. The major and minor radii of the ITER plasma are 6.2 m and 2.0 m, respectively and the plasma volume is approximately 800 m^3. The toroidal magnetic field and plasma current are B_t = 5 T and I_p = 15 MA, respectively. ITER has been therefore expected to continuously produce 500 MW output power over 500 s. Figure 1.4 shows the plasma facing components of ITER, consisting of beryllium first wall and tungsten divertor plates. The divertor is mainly used to exhaust the plasma particles from the ITER. In the ITER the use of tungsten divertor plates has been decided because of its high melting point [8].

The most important issue in the ITER research is to demonstrate a steady-state operation of the burning plasma. For the purpose the heat load mitigation of divertor plates becomes one of critical issues [8]. Due to the radial transport induced by several

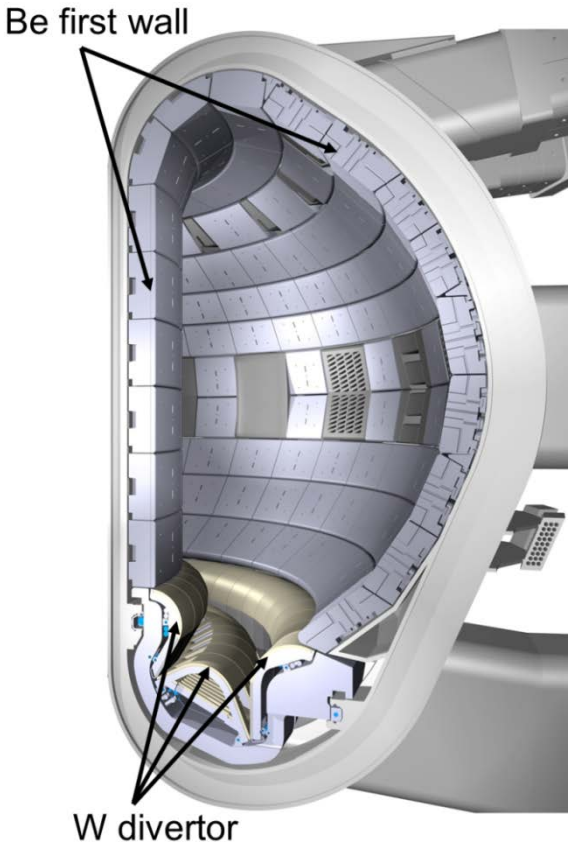

Fig. 1.4 Cross-sectional view of ITER vacuum vessel with beryllium first wall and tungsten divertor [8].

physical mechanisms like turbulence, drifts and inter particle collisions, the energy and particle across the LCFS and reach the SOL region. In the SOL, the parallel transport is entirely dominant compared to the cross-field transport. As a result, the thickness of SOL, λ_{SOL}, is very small, e.g., $\lambda_{SOL} \sim 1$ cm at the midplane, and the particles in the SOL are mainly transported along the magnetic field lines. Thus, the parallel power density in the SOL is estimated to be very huge, i.e., > 1000 MW/m^2 at the midplane. Although geometrical factors associated with the magnetic field and the divertor plate configuration can actually reduce the power coming on the divertor plates by a factor of ~ 100, the remained power density on the divertor plates is still too high for realistic heat removal scenarios. The sustainable heat flux of the ITER divertor is estimated to be >10 MW/m^2 during the steady state operation and >20 MW/m^2 during slow transient phases [9]. In order to reduce the divertor plate erosion and to achieve large lifetime of the divertor plate, the peak heat flux to the divertor plate should be reduced to ~ 5

MW/m^2. For this reason, the power flowing to the SOL must be mitigated before arriving at the divertor plates.

1.3.2 Plasma detachment in tokamaks

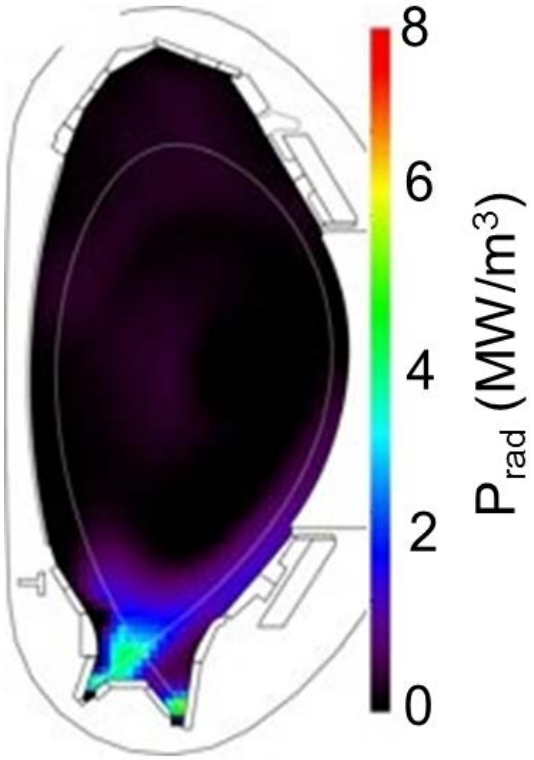

Fig. 1.5 Typical 2-D distribution of local radiation in ASDEX-Upgrade during plasma detachment triggered by nitrogen gas feed in the divertor region [9].

One of possible solutions for the heat load mitigation in the steady state operation of the ITER is to replace the edge heat flux by the impurity radiation [10]. The heat flux on the divertor plates can be thereby reduced by spreading the edge heat flux over the whole direction. The radiative divertor, i.e., plasma detachment, can be created by injection of working gas or gaseous impurities into divertor region. This scenario has demonstrated clear heat load mitigation on divertor plates with revealing a strong increase in radiation near the X-point in the divertor region. The result is shown in Fig. 1.5 [9]. Experimental results on plasma detachment in most divertor tokamaks [9] are characterized by

1) high energy radiation losses from the SOL region,

2) low plasma temperature near the divertor plates,

3) relatively high neutral gas density in the divertor volume,

4) strong decrease in the plasma particle and energy fluxes onto the plates

and

5) strong plasma pressure drop along magnetic field lines in the divertor volume.

On the other hand, most present tokamaks have been operated with the high confinement mode, i.e., H-mode [11]. It is therefore important to operate the plasma detachment with the H-mode. The H-mode plasma with detachment has been achieved with slight degradation of confinement in many tokamaks, e.g., ASDEX Upgrade [9], DIII-D [12], JT-60U [13], JET [11] and Alcator C-Mod [12]. It has been demonstrated that the heat load on divertor plates can be significantly mitigated during the plasma detachment. However, the operation window of plasma detachment is very narrow in all the results from the present tokamaks. In addition, the enhanced radiation layer in the divertor region frequently penetrates into the confinement region during the plasma detachment phase. The expanded radiation layer easily leads to a severe degradation of the global energy confinement or a termination of discharges due to a radiation collapse, which is often accompanied by a radiation instability called multifaceted asymmetric radiation from the edge (MARFE) [9,15]. Therefore, an alternative method has to be considered for extending the operation window for plasma detachment in future tokamaks with steady-state H-mode plasmas.

1.3.3 Plasma detachment assisted by RMP in LHD

Detached plasmas have been also studied in LHD and a steady discharge with plasma detachment has been energetically explored using external impurity gas feed as well as the case of tokamaks. However, extension of detached plasma phase in steady discharges was truly difficult because of the discharge termination by radiation collapse, of which the result was very similar to the tokamak detachment experiment using external impurity gases. Recently, on the other hand, a new technique for producing the detached plasma has been attempted in LHD using RMP coils toward a steady detached plasma discharge [15]. In this scenario, any additional impurity gas feed is not required. A successful discharge with a steady plasma detachment phase has been thus obtained using the RMP coils at outwardly shifted magnetic axis position of R_{ax} = 3.90 m. It is demonstrated that the heat load on divertor plates decreases by a factor of 3 to 10 during the steady detachment phase basically without degradation of energy confinement [15].

Dedicated experiments have been performed in LHD to investigate the operation window for the steady-state sustainment of detached plasmas [15]. A typical waveform of detached plasma discharge assisted by RMP coils, which is called "RMP-assisted

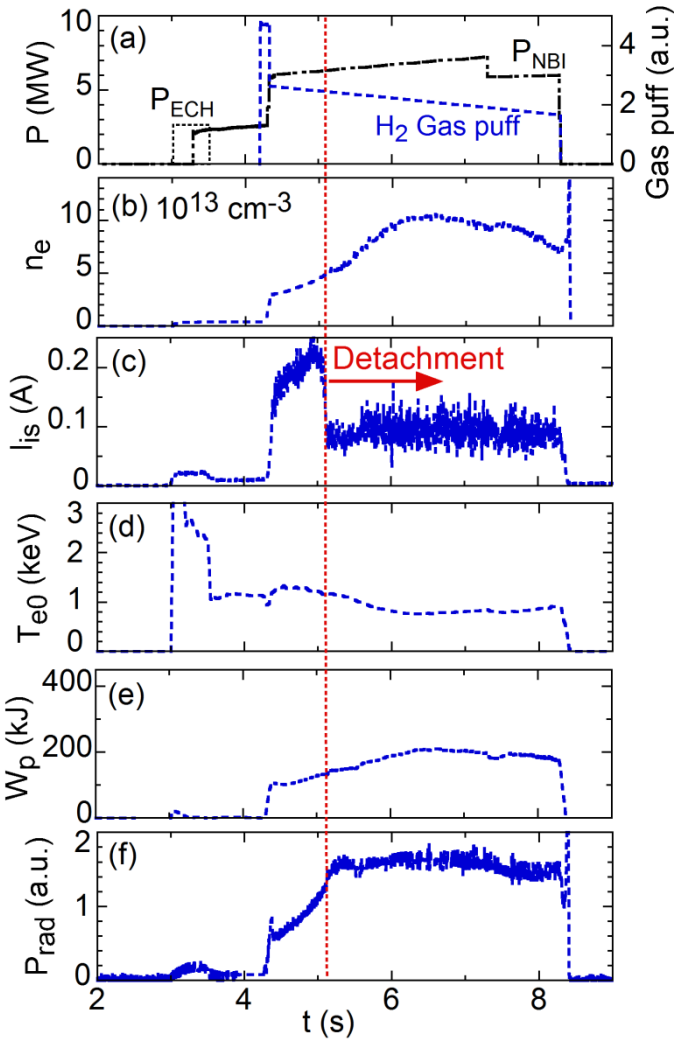

Fig. 1.6 Time behaviors of (a) NBI port-through power and H_2 gas puffing, (b) line-averaged electron density, (c) ion saturated current, (d) central electron temperature, (e) stored energy and (f) total radiation loss in discharge with RMP-assisted detached plasma. The timing of detachment transition is indicated with a vertical dotted line.

detachment", is shown in Fig. 1.6. The discharge initiated with electron cyclotron heating (ECH) at t = 3.0 s is maintained with negative-ion-source-based NBIs (n-NBIs) for 5 s from t = 3.3 to 8.3 s. The maximum RMP coil current of I_{coil} = 3340 A is constantly supplied during the discharge. The electron density gradually increases with hydrogen gas puffing and reaches a density threshold to trigger the plasma detachment, i.e., $n_e = 5 \times 10^{13}$ cm^{-3} in the present discharge condition. The transition to plasma detachment phase can be easily identified from a suddenly decrease in the ion saturated current (I_{is}) at t = 5.1 s. The plasma detachment is steadily maintained until the end of

discharge. It should be noticed here that the discharge is terminated at t = 8.3 s by switching off the NBI pulse instead of the radiation collapse. After the transition to the plasma detachment phase, the electron density continues to increase until t = 6.3 s and saturates at $n_e = 12 \times 10^{13}$ cm^{-3}. The central electron temperature starts to slightly decrease with the density increase. It finally stays at $T_{e0} \sim 0.8$ keV during the detachment phase. In contrast, the stored energy continues to increase even after the detachment transition mainly reflecting the density increase. The radiation power keeps a constant level during the whole plasma detachment phase.

1.4 History of EUV spectroscopy in LHD

Passive spectroscopy is a unique diagnostic method for the impurity transport study, in particular, at edge plasmas, in the fusion research with magnetically confined toroidal plasmas. Extreme ultraviolet (EUV) spectroscopy in wavelength range of 10 to 500 Å is a powerful tool for the impurity transport study in both core and edge regions. Various types of EUV spectrometers have been developed up to now to study the impurity transport in LHD, as listed in Table 1.1.

In the first step, two EUV spectrometers named EUV_Short and EUV_Long have been developed as a part of the impurity monitor system to routinely monitor the impurity behavior in LHD discharges [16,17]. Both spectrometers of EUV_Short and EUV_Long having no spatial resolution are working in wider wavelength ranges of 10–130 Å and 30–600 Å, respectively. Most of spectral lines from intrinsic impurities, e.g., helium, carbon, oxygen and iron, can be monitored in the EUV range based on the two spectrometers with a high temporal resolution of 5 ms.

In the second step, two space-resolved EUV spectrometers named EUV_Short2 and EUV_Long2 have been developed to observe vertical profiles and 2-D distributions of impurity line emissions, respectively [18,19]. Both spectrometers of EUV_Short2 and EUV_Long2 are installed on the same LHD port (#10-O) as the EUV_Short and EUV_Long. The EUV_Short2 is mainly used to measure the vertical profile of impurity line emissions in the core region in the wavelength range of 10–130 Å. The profile measurement with EUV_Short2 is very important for the impurity transport study in core plasmas based on the 1-D transport simulation with diffusion-convection model in addition to the spectroscopic study of highly ionized tungsten ions.

The EUV_Long2 is initially designed to measure the vertical profile of impurity line emissions in the wavelength range of 30–600 Å from plasma core and edge regions [18]. The impurity transport has been studied in LHD based on the profile measurement with the EUV_Long2 spectrometer [20]. It has been also used for Z_{eff} profile measurement using EUV bremsstrahlung continuum [21]. As the impurity transport

Table 1.1 Specifications of EUV spectrometers in LHD

Name	Grating (Grooves /mm)	Wavelength resolution (Å/mm)	Wavelength range (Å)	Profile measurement	Number of observation channels	Time resolution (ms)
EUV_Short	2400	3 - 11	10-130	no	1	5
EUV_Long	1200	1.3 - 4.3	30-600	no	1	5
EUV_Short2	2400	3 - 11	10-130	Vertical profile	204	50-100
EUV_Long2	1200	1.3 - 4.3	30-600	Vertical profile, 2-D	204	50-100

study in the ergodic layer with 3-D magnetic field structure progresses with measured vertical profiles, several vertical profiles have been remained unexplained. In order to make deeper understanding on the edge impurity transport, the EUV_Long2 has been then upgraded to measure the 2-D distribution of edge impurity line emissions by horizontally scanning the optical axis of the spectrometer with a stepping motor during a stable discharge [22]. The 2-D distribution of edge impurity line emissions has been successfully observed for various impurity species, e.g., helium, carbon, neon and iron [23-26]. For observation of the 2-D distribution, however, a long steady phase, e.g., 6–8 s, was necessary for the discharge due to several technical problems.

1.5 Objective and structure of this thesis

The objective of the thesis is to improve the performance of the EUV_Long2 spectrometer system for rapid 2-D measurement and to study the 3-D structure of edge impurity ions in high-power n-NBI discharges, in particular, RMP-assisted plasma detachment. The 2-D distribution measurement is crucially important for study on the

3-D structure of edge impurity ions and deeper understanding on the role of edge enhanced radiation in triggering the RMP-assisted plasma detachment. In LHD, however, the pulse length of high-power n-NBIs is limited to 3 s due to the high heat load on several components of the ion source, whereas the 2-D distribution measurement of impurity line emissions with the EUV_long2 spectrometer requires a longer pulse length of 6–8 s. Therefore, the performance improvement of the EUV_long2 is unavoidably necessary for studying the impurity transport at the RMP-assisted plasma detachment phase in high-power n-NBI discharges.

In Chapter 2 the performance improvement of the 2-D space-resolved EUV spectrometer is described. At first, the principle of 2-D distribution measurement of edge impurity emissions is introduced in detail. Then, several methods for the performance improvement of 2-D space-resolved EUV spectrometer system, which have been done in the present thesis work, are described, i.e., installations of a high frame rate CCD and a PET filter, increase in horizontal spectrometer scanning speed and adoption of an intensity normalization method. Typical 2-D distributions of different edge impurity spices are presented with a high spatial resolution.

In Chapter 3 the poloidal distribution of edge impurity emissions evaluated from 2-D distribution measurement is presented. The poloidal distribution of CIV, CVI, FeXV and FeXVIII with different ionization energies is reconstructed by analyzing the 2-D distribution against magnetic flux surfaces calculated with a three-dimensional (3-D) equilibrium code, VMEC. The poloidal distribution of the CIV emissivity is also simulated with 3-D edge plasma transport code, EMC3-EIRENE.

In Chapter 4 the partial carbon radiation at each ionization stage of C^{2+} to C^{5+} ions are analyzed in attached and detached plasmas. Resonance lines of CIII (977.02 Å), CIV (1548.2 Å), CV (40.27 Å) and CVI (33.73 Å) measured by vacuum ultraviolet (VUV) and EUV spectrometers are used to estimate the radiation power from C^{2+} to C^{5+} ions. In the analysis, the ratio of the partial carbon radiation to the resonance line is calculated with ADAS atomic code. Discussions are made on the partial carbon radiation from C^{2+} to C^{5+} ions in attached and detached plasmas.

In Chapter 5 the vertical profile of edge impurity ions measured during the RMP-assisted plasma detachment with the EUV_Long2 spectrometer is presented. The formation of m/n = 1/1 RMP magnetic island is investigated by analyzing the radial position at the top and bottom edge peaks appeared in CIII–CVI vertical profiles.

In Chapter 6 vertical profiles and 2-D distributions of edge impurity carbon emissions of CIII–CVI are studied in attached and detached plasmas. The 3-D structure of carbon ions is analyzed with magnetic field structure in the ergodic layer based on the 2-D distribution measurement. The role of edge impurity radiation in triggering the plasma detachment is studied by comparing the carbon distribution between attached

and detached plasmas. The measured carbon 2-D distribution is also analyzed with EMC3-EIRENE for attached plasmas without RMP. The cross-field diffusion of carbon ions in the stochastic magnetic field layer is discussed against different magnetic axis positions of R_{ax} = 3.75 m and 3.90 m.

In Chapter 7 the results and conclusions obtained through the present thesis work are summarized.

References

[1] J. Wesson, Tokamaks, 3rd edition, Oxford University Press, (2004).
[2] F. F. Chen, An indispensable truth: How fusion power can save the planet, Spring Press, (2011).
[3] G. M. McGraken, et al., Nucl. Fusion **19**, 889 (1979).
[4] J. F. Friichtenicht, Rev. Sci. Instr. **45**, 51 (1974).
[5] N. Ohyabu, et. al., Nucl. Fusion **34**, 387 (1994).
[6] S. Morita, et. al., Plasma Phys. Control. Fusion **56**, 094007 (2014).
[7] M. B. Chowdhuri, et. al., Phys. Plasmas **16**, 062502 (2009).
[8] ITER Team. ITER physics basis. Chapter 4: Power and particle control, Nucl. Fusion **39**, 2391 (1999).
[9] F. Reimold, et. al., Nucl. Fusion **55**, 033004 (2015).
[10] O. Gruber, et. al., Phys. Rev. Lett. **74**, 4217 (1995).
[11] A. Huber, et. al., J. Nucl. Mater. **438**, S139-S147 (2013).
[12] B. Lipschultz, et. al., Fusion Sci. Technol. 51 369–89 (2007).
[13] T. W. Petrie, et. al., J. Nucl. Mater. **363**, 416–420 (2007).
[14] T. Nakano, et. al., J. of Nucl. Mater. **438**, S291–S296 (2013).
[15] M. Kobayashi, et al., Phys. Plasmas **17**, 056111(2010).
[16] M. B. Chowdhuri, et al., Applied Optic. **47**, 135 (2008).
[17] M. B. Chowdhuri, et al., Rev. Sci. Instrum. **78**, 023501 (2007) and Erratum: **84**, 109901 (2013).
[18] C. F. Dong, et al., Rev. Sci. Instrum. **81**, 033107 (2010).
[19] X. L. Huang, et al., Rev. Sci. Instrum. **85**, 043511 (2014).
[20] C. F. Dong, et al., Jpn. J. Appl. Phys. **51**, 010205 (2012).
[21] X. L. Huang, et al., Plasma Fusion Res. **10**, 3402036 (2015).
[22] E. H. Wang, et al., Rev. Sci. Instrum. **83**, 043503 (2012).
[23] S. Morita, et. al., Nucl. Fusion **53**, 093017 (2013).
[24] S. Morita, et. al., Plasma Phys. Control. Fusion **56**, 094007 (2014).
[25] E. H. Wang, et al., Plasma Fusion Res. **8**, 2402176 (2013).
[26] E. H. Wang, et al., Plasma Sci. Technol. **15**, 106 (2013).

Chapter 2

Performance upgrade of 2-D space-resolved EUV spectrometer

2.1 Introduction

In the Large Helical Device (LHD), the elliptical magnetic surface with closed magnetic fields for plasma confinement is created by a pair of continuously wound superconducting helical coils, with a poloidal pitch number of $l = 2$ and a toroidal pitch number of $m = 10$, and three pairs of superconducting poloidal coils [1,2]. The LHD discharge then exhibits high-performance core plasmas in terms of both temperature and density. On the other hand, higher-order Fourier components in the magnetic field generated by the helical coil change the edge magnetic field structure into a stochastic magnetic field layer with open magnetic fields called the "ergodic layer". Therefore, the ergodic layer always intrinsically exists outside the core plasma in all the magnetic configurations of LHD. The stochastic magnetic field in the ergodic layer with a three-dimensional (3-D) structure consists of a mixture of small and large magnetic field connection lengths ($10 \leq L_c \leq 2000$ m) [3-7]. In particular, the magnetic field at the inner region of the ergodic layer is sufficiently long to confine the edge plasma, so that a high-density plasma can be easily maintained at a high temperature. Typical values of electron temperature and density in the ergodic layer are distributed in ranges of 10 – 500 eV and $(1 – 10) \times 10^{13}$ cm^{-3}, respectively. In the ergodic layer, therefore, impurity spectral lines are mainly emitted in the extreme ultraviolet (EUV) wavelength range of 10 to 500 Å [8]. Thus, two-dimensional (2-D) EUV spectroscopy is required to study the impurity transport in the ergodic layer [5].

A space-resolved EUV spectrometer has been developed for measuring a vertical profile of impurity line emissions in the wavelength range of 40 – 600 Å. The 2-D distribution of impurity emissions is measured by horizontally scanning the optical axis of the spectrometer during a discharge [9]. To date, the 2-D impurity emission distribution has been observed for various impurity species, e.g., helium, carbon, neon and iron [8-12]. By analyzing the 2-D distribution of CIV ($1s^2 3p – 1s^2 2s$: 312.4 Å)

emission, it is found that the emission is strongly enhanced along a diagonal X-point trajectory and that the emission location clearly depends on the magnetic axis position (R_{ax}). When R_{ax} is shifted from 3.60 m to 3.75 m, the strong-CIV-emission trace along the X-point moves from the inboard to outboard side [10]. The result is well explained with a small change in edge magnetic fields in the vicinity of X-points. The 2-D distribution of edge electron temperature is also obtained by analyzing the line intensity ratio of NeVIII (3p – 2s: 88.09, 88.13 Å) to NeVIII (3s – 2p: 102.91, 103.09Å) [8].

In LHD, two positive-ion-source-based neutral beam injections (p-NBI: 40 keV) and three negative-ion-source-based neutral beam injections (n-NBI: 180 keV) are mainly applied for ion and electron heating, respectively. High-density NBI discharges up to $n_e = 10^{15}$ cm^{-3} can be sustained by three tangentially injected n-NBIs with total input power of 20 MW. To avoid a breakdown of the n-NBI ion source due to an extremely high heat load, the pulse length of high-power n-NBIs is normally limited to 3 s [13-15], while the 2-D measurement of impurity emissions requires a larger pulse length of 6–8 s. The n-NBIs with reduced input power are then connected in tandem to extend the pulse length of discharge duration, e.g., 10 s in a previous study [9], while it is not easy to obtain the steady discharge in the tandem operation. Nevertheless, it is still difficult to observe the impurity emission structure in detail owing to a low spatial resolution in the 2-D measurement. Therefore, performance improvement of the 2-D EUV spectrometer system is necessary to measure the 2-D distribution of impurity emissions in high-power n-NBI discharges with good spatial resolution.

The space-resolved EUV spectrometer can be used to observe a roughly 50-cm-long vertical profile at a horizontally elongated plasma cross section whose length corresponds to one-half of the vertical plasma diameter. Therefore, two or three discharges with a relatively long steady phase, e.g., 5 s, are required to measure the full vertical distribution by changing the vertical angle of the spectrometer. When the full vertical 2-D distribution is observed during the steady phase of a few subsequent discharges, each discharge has a shot-to-shot intensity variation in EUV emission. The quality of 2-D impurity emission images is considerably affected by the shot-to-shot variation. In addition, a temporal intensity variation in the EUV emission during the horizontal scan of the spectrometer also deteriorates the quality of 2-D impurity emission images, particularly, the edge impurity emission images. A reduction of image quality due to the intensity variation is essentially important to improve the performance of the 2-D distribution measurement.

On the basis of the several reasons mentioned above, the 2-D space-resolved EUV spectrometer system is upgraded by installing a new high-frame-rate charge-coupled device (CCD) and increasing its horizontal scanning speed. A thin polyethylene terephthalate (PET) filter is also installed in front of an entrance slit of the space-resolved EUV spectrometer to reduce the CCD noise caused by high-energy

neutral particles in NBI discharges. In this paper, the EUV spectroscopy in LHD is described as well as the principle of the 2-D distribution measurement in Sect. 2.2. The absolute intensity calibration of the EUV spectrometer system is explained in Sect. 2.3. The performance improvement of 2-D EUV spectroscopy is shown in Sect. 2.4 in relation to spatial and temporal resolutions, the signal normalization method, and the filter method for the noise reduction. Typical results of the high-resolution 2-D distribution measurement are presented in Sect. 2.5. The study is summarized in Sect. 2.6.

2.2 Principle of 2-D EUV spectroscopy

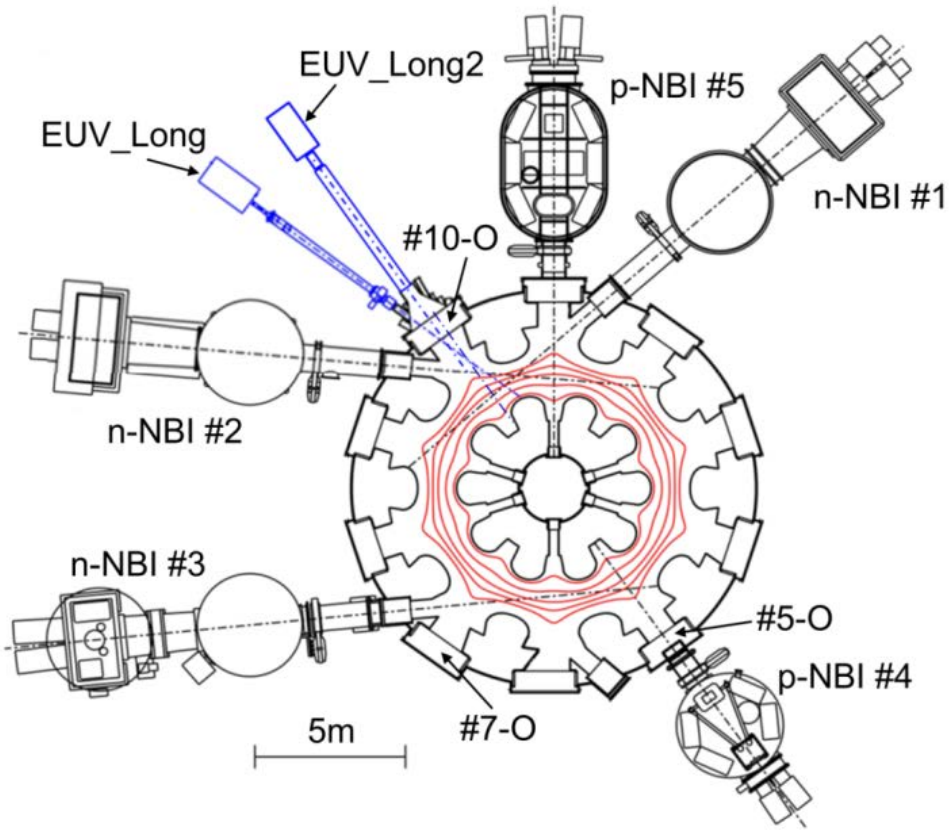

Fig. 2.1 Arrangement of space-resolved EUV spectrometer (EUV_Long2), high-time-resolution EUV spectrometer (EUV_Long), n-NBIs (#1–#3) and p-NBIs (#4 and #5) in LHD. n-NBI denotes negative-ion-source-based NBI with a beam energy of 180 keV and p-NBI denotes positive-ion-source-based NBI with a beam energy of 40 keV.

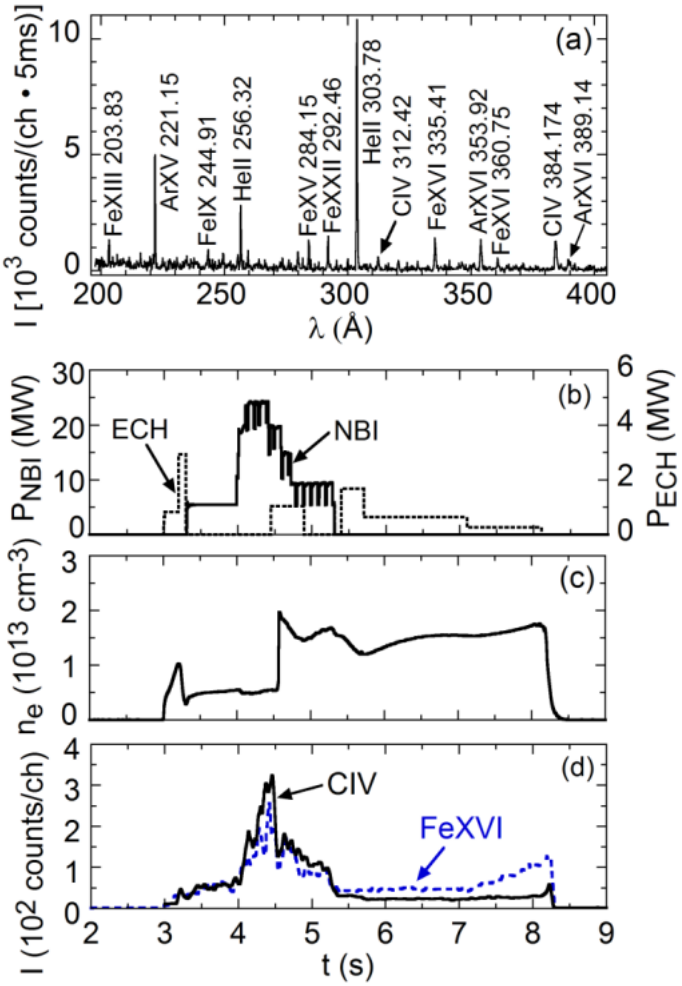

Fig. 2.2 (a) Typical spectra in wavelength range of 200–400 Å measured using EUV_Long spectrometer and time behaviors of (b) NBI port-through power, (c) line-averaged electron density and (d) FeXVI (335.407 Å: dashed line) and CIV (312.42 Å: solid line) measured using EUV_Long spectrometer.

The arrangement of the EUV spectroscopy and NBI in LHD is shown in Fig. 2.1. The three n-NBIs with a high beam energy of 180 keV are installed tangential to the toroidal magnetic field to maintain a central beam deposition. The two p-NBIs with a low energy of 40 keV are installed perpendicular to the toroidal magnetic field to achieve an efficient heating of bulk ions in low-density discharges. Two EUV spectrometers working in wide wavelength range of 30 to 650 Å named EUV_Long and EUV_Long2 are installed in the same diagnostic port, the #10-O LHD port [16]. The EUV_Long spectrometer is developed for core impurity diagnostics as a part of the impurity monitor system to routinely monitor the impurity behavior in LHD discharges.

The EUV_Long2 spectrometer is developed to observe a vertical profile of impurity line emissions. Then, the CCD of the EUV_Long spectrometer is usually operated in the full vertical binning (FVB) mode with a high temporal resolution of 5 ms.

A typical wavelength spectrum from the EUV_Long spectrometer is shown in Fig. 2.2 (a), which is observed in NBI discharges with an Ar puff for measuring ion temperature profiles plotted in Figs. 2.2 (b)–2.2 (d). Although the spectral profile is slightly broadened owing to the thermal motion of impurity ions, the Doppler broadening is negligibly smaller than the spectral resolution. The spectrum intensity remains constant, even when the Doppler broadening is considered. In the present analysis, therefore, the effect of Doppler broadening is not considered. Helium gas remains in the discharge as a residual effect of He glow discharges and ICRF heating with the majority of He ions. Iron originates from the first wall made of stainless steel. Figures 2.2 (b) and 2.2 (c) show the temporal behaviors of NBI port-through power and line-averaged electron density, respectively. A carbon pellet is injected at 4.55 s to increase the central ion temperature. The temporal behaviors of FeXVI at 335.407 Å and CIV at 312.42 Å in Fig. 2.2 (a) are plotted in Fig. 2.2 (d). The impurity intensity increases during high-power NBI for 4.0–5.5 s. The intensity behavior of impurity line emissions measured with the EUV_Long spectrometer is used for the intensity normalization of 2-D image data measured with a space-resolved EUV spectrometer (EUV_Long2), which is described in Sect. 2.4 in detail [17].

As shown in Fig. 2.1, the space-resolved EUV spectrometer named EUV_Long2 is installed on the same LHD port (#10-O) as the EUV_Long spectrometer. A schematic view of the space-resolved EUV spectrometer system is shown in Fig. 2.3 with the toroidal cross section of the LHD plasma at the magnetic axis position of R_{ax} = 3.75 m. A 5-m-long rectangular vacuum extension chamber is connected to the LHD diagnostic port through a rectangular swing valve, a rectangular bellow flange and an insulator plate. The space-resolved EUV spectrometer is connected to the backside of the extension chamber. In the present diagnostic system, a considerably big observation port with a vertical size of 1200 mm and a horizontal size of 700 mm is maintained for the 2-D image measurement. The space-resolved EUV spectrometer is then placed at a long distance of 9.3 m from the plasma center to increase the magnification of a vertical image of LHD plasmas observed with CCD. The spectrometer is equipped with two stepping motors, which independently rotate the optical axis of the space-resolved EUV spectrometer vertically and horizontally [18].

The vertical observation range can be freely chosen by changing the vertical angle of the spectrometer optical axis. The vertical profile can also be observed at any toroidal position by changing the horizontal angle of the spectrometer optical axis. The elliptical shape of the LHD plasma rapidly rotates in the poloidal direction as the toroidal angle is changed. The change in the poloidal cross section of LHD plasmas is

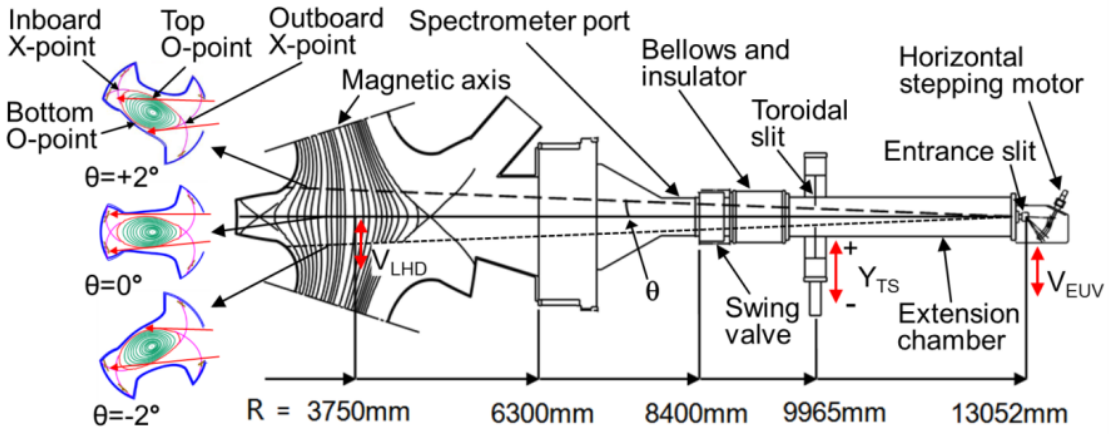

Fig. 2.3 Schematic view of space-resolved EUV spectrometer (EUV_Long2) connected to the end of a 3-m-long extension chamber. Three poloidal cross sections of the LHD plasma are also shown for observation chords with different toroidal angles of θ = +2° (long dashed line), 0° (solid line) and −2° (short dashed line). The top and bottom boundaries of the vertical observation range are indicated by two arrows (solid lines) in each poloidal cross section. Horizontal scanning speeds at the space-resolved spectrometer and plasma magnetic axis are denoted by V_{EUV} and V_{LHD}, respectively. Y_{TS} indicates the horizontal distance between the center of the movable toroidal slit and the central optical axis at θ = 0° denoted by a solid line. The toroidal slit consists of two horizontally movable flat panels with a horizontal size of 505 mm and a vertical size of 1050 mm.

shown on the left side of Fig. 2.3 at different horizontal angles of θ = +2°, 0° and –2°. The vertical profile of LHD elliptical plasmas in a horizontally elongated plasma cross section is observed when the spectrometer optical axis is perpendicular to the toroidal magnetic field, i.e., θ = 0°. The vertical size along the short axis of the elliptical plasma including the ergodic layer is nearly 1.0 m at θ = 0°, whereas the vertical observation range of the present spectrometer system is 550 mm at R_{ax} = 3.75 m. Therefore, the 2-D measurement has to be carried out at least two times, i.e., at the lower half (-550 ≤ Z ≤ 0 mm) and upper half (0 ≤ Z ≤ 550 mm), to complete the full vertical profile measurement from Z = –550 to 550 mm [9].

As shown in Fig. 2.3, the central observation chord at θ = 0° passes through both the outboard and inboard X-points. It is then difficult to separately study the edge impurity transport at inboard and outboard X-point regions, even when the vertical impurity profile is precisely measured at θ = 0°. Figure 2.4 shows the inboard and outboard X-point trajectories in the observation range of the space-resolved

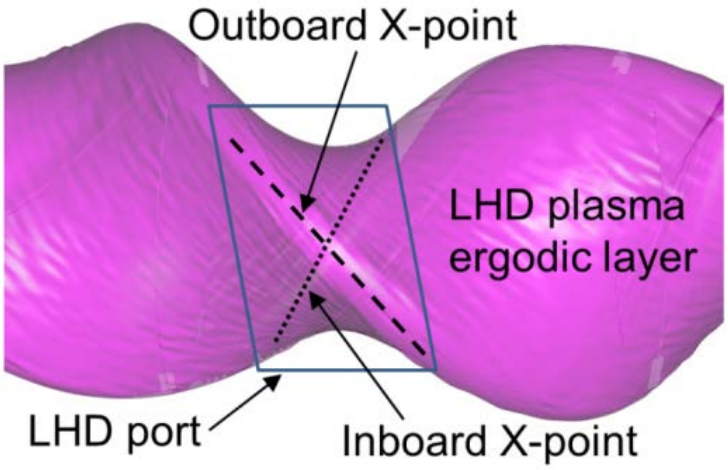

Fig. 2.4 Horizontal view of LHD plasmas with ergodic layer. The LHD port is indicated by a solid-line diamond. Inboard and outboard X-point trajectories are indicated by dotted and dashed lines, respectively.

spectrometer. Since the LHD elliptical plasma poloidally rotates five times during one toroidal turn, the position of two X-points represents a diagonal trajectory. In the figure, therefore, the inboard and outboard X-point trajectories can be separately shown with dotted and dashed lines, respectively. Therefore, when the vertical impurity profile is measured at a different horizontal angle from $\theta = 0°$, it becomes possible to study the edge impurity transport in detail because the two X-points can be separately measured. From the poloidal cross section at $\theta = +2°$ and $-2°$ in Fig. 2.3, it can be understood that a good separation is obtained in the impurity emission between the inboard and outboard X-point regions. This is one of the important motivations when the 2-D distribution is measured.

The space-resolved EUV spectrometer with horizontal dispersion consists of an entrance slit, a spatial resolution slit placed in front of the entrance slit, a gold-coated varied-line-spacing (VLS) grating and a CCD. The vertical profile of impurity emissions can be projected on the CCD using a narrow spatial resolution slit placed horizontally. A 200-μm-width entrance slit and a 1-mm-width spatial-resolution slit are used in this study, while a 30 μm entrance slit is usually used for a conventional spectrum measurement without spatial resolution to increase the spectral resolution. The signal intensity from LHD plasmas detected with the CCD is sufficiently high for observation of the 2-D distribution of impurity line emissions. A holographic laminar-type VLS grating (Shimadzu 30-002: 1200 grooves/mm) with an effective area of 26 mm in groove length and 46 mm in groove distance is used to increase the reflectivity of the

grating, particularly, in a shorter wavelength range of $\lambda \leq 100$Å and also to eliminate the contribution of higher-order light [17,18].

A back-illuminated CCD (Andor DO420-BN) with 1024 × 256 pixels has been used in the space-resolved EUV spectrometer to detect EUV impurity emissions until the 2012 LHD experimental campaign. The active area of the CCD is 26.7 × 6.7 mm^2 with a pixel size of 26 × 26 μm^2. Since the CCD is maintained at -20 °C in usual operation, the thermal noise can be sufficiently reduced. The binning mode is usually used to increase readout speed and signal-to-noise ratio. In the binning mode, the signal charge from adjacent pixels is accumulated in the shift register and the accumulated signal charge is transferred to a preamplifier for analog-to-digital conversion. In this study a sub-image with 51 × 204 channels, which is created by summing up 5 adjacent pixels and replaced into a single channel, is used for the profile measurement. The signal exposure time and sampling time per frame are 137 and 200 ms, respectively. The full image mode is only used for checking the spectral resolution to avoid errors in the spectral resolution measurement due to a small misalignment of the CCD angle [18]. In the full image mode, a CCD exposure time longer than the discharge duration is chosen so as not to affect the spectral resolution during relatively long signal readout.

In the 2013 LHD experimental campaign, on the other hand, the original CCD (Andor DO420-BN) with a 1 MHz clock frequency used until 2012 is replaced by a new CCD (Andor DO920P-BN) with a 2.5 MHz clock frequency. The vertical shift speed is significantly decreased in the new CCD and the readout time is sufficiently reduced from 63 to 16.8 ms under the same binning mode with 51 × 204 sub-images. As a result, it becomes possible to observe the vertical profile of impurity emissions with a sampling time of 50 ms or 100 ms per frame, and the time duration necessary for the 2-D distribution measurement can also be improved. The result is presented in Sect. 2.4.

2.3 Absolute intensity calibration

The absolute intensity calibration of the EUV spectrometer is necessary for quantitative analysis of impurity line emissions. The EUV spectrometer system can be absolutely calibrated on the basis of the radial profile measurement of bremsstrahlung continuum in EUV and visible ranges. This method is developed for the EUV spectroscopy for the first time in LHD [16,19]. Firstly, the chord-integrated visible bremsstrahlung profile measured with a visible spectrometer is reconstructed into the local emissivity profile as a function of magnetic flux surface using the Abel inversion technique. Then, the local emissivity profile of EUV bremsstrahlung is calculated from the local emissivity profile of visible bremsstrahlung taking into account the electron temperature profile. Finally, chord-integrated intensity profile of EUV bremsstrahlung

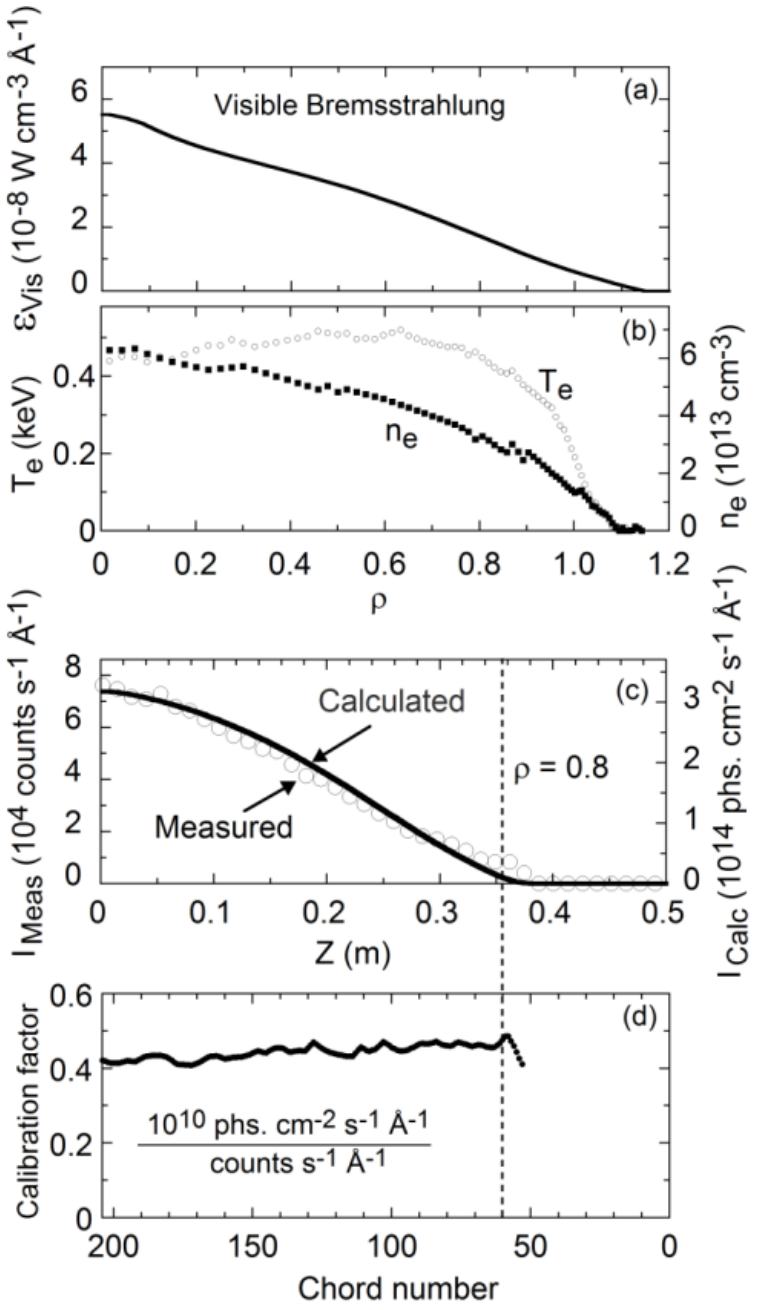

Fig. 2.5 (a) Local emissivity profile of visible bremsstrahlung at 5330 Å and (b) electron temperature (open circles) and density (solid squares) profiles measured using Thomson scattering system as a function of averaged plasma minor radius, (c) line-integrated profiles of calculated (solid line) and measured (open circles) EUV bremsstrahlung at 87 Å as functions of vertical position and (d) intensity calibration factor of space-resolved EUV spectrometer system as a function of chord number.

continuum is derived from the local emissivity profile on the basis of the geometric relationship between the observation chord of the space-resolved EUV spectrometer and the magnetic surface structure. The absolute intensity calibration factor of the space-resolved EUV spectrometer is thus obtained by directly comparing the calculated and measured EUV bremsstrahlung profiles.

In LHD, a Czerny-Turner-type visible spectrometer with a focal length of 30 cm is installed at the horizontally elongated plasma cross section to measure a full radial profile ($-0.6 \leq Z \leq 0.6$ m) of the visible bremsstrahlung and spectral lines in the range of 3000 – 9000 Å using 44 optical fibers with parallel observation chords. In the present calibration, the bremsstrahlung continuum at 5330 Å is used with a wavelength interval of 10 Å, i.e., 5325–5335 Å [20]. Figure 2.5 (a) shows the vertical emissivity profile reconstructed from the chord-integrated vertical profile of visible bremsstrahlung measured at 5330 Å. The horizontal axis is the normalized minor radius. Since high-density discharges in LHD generally have a peaked density profile, the bremsstrahlung profile also has a centrally peaked profile. Then, the analytical error in the local emissivity profile calculation based on the Abel inversion is entirely small. The magnetic surface used in the Abel inversion is calculated with the Variational Moments Equilibrium Code (VMEC), including the effect of finite plasma pressure [21,22]. The electron temperature and density profiles measured using the Thomson scattering system, which are taken from the same discharge as the visible bremsstrahlung shown in Fig. 2.5 (a), are plotted in Fig. 2.5 (b) [23]. In this plot, the presence of the magnetic surface is also assumed outside the last closed flux surface (LCFS) by extrapolating the magnetic surface at LCFS ($\rho = 1$).

The local emissivity profile of EUV bremsstrahlung at 87 Å can be calculated from the local emissivity profile of visible bremsstrahlung shown in Fig. 2.5 (a) with taking into account the electron temperature profile shown in Fig. 2.5 (b) based on the following equation:

$$\frac{\varepsilon_{EUV}}{\varepsilon_{\mathrm{Vis}}} = \left(\frac{\lambda_{\mathrm{Vis}}}{\lambda_{EUV}}\right)^2 \left(\frac{g_{\mathrm{ff\_EUV}}}{g_{ff\_Vis}}\right) \exp\left[-\frac{12400}{T_e}\left(\frac{1}{\lambda_{EUV}} - \frac{1}{\lambda_{Vis}}\right)\right], \tag{2.1}$$

where λ_{EUV} (Å) and λ_{Vis} (Å) denote the bremsstrahlung wavelength in the EUV and visible ranges, respectively. The variables ε (photons cm^{-3} s^{-1} $\mathrm{Å}^{-1}$), g_{ff} and T_e (eV) express the local emissivity of bremsstrahlung, the free-free gaunt factor and the electron temperature, respectively. The free-free gaunt factor is theoretically calculated for a hydrogenic system as functions of wavelength and electron temperature [24]. The chord-integrated intensity profile of EUV bremsstrahlung can then be calculated as a

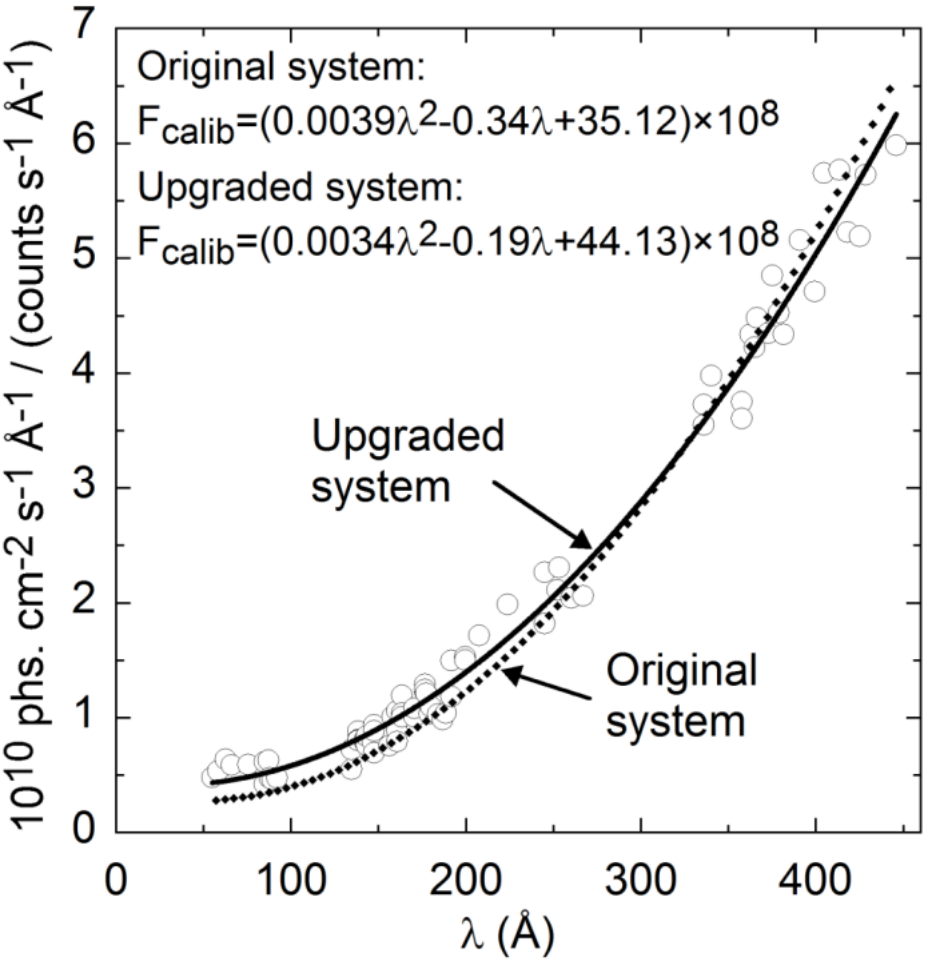

Fig. 2.6 Absolute intensity calibration factor (open circles) measured using the present upgraded system as a function of wavelength. Data points range between 60 and 440 Å. The calibration factor fitted with polynomial equation is compared between the upgraded system (solid line) and the original system (dotted line).

function of vertical position by integrating the local emissivity along each chord. The result is plotted in Fig. 2.5 (c) with a solid line. The chord-integrated profile of EUV bremsstrahlung measured at 87 Å at a wavelength interval of 10 Å is also plotted in the figure with open circles. Thus, the absolute intensity calibration factor is obtained by comparing the calculated [solid line in Fig. 2.5 (c)] and measured [open circles in Fig. 2.5 (c)] chord-integrated EUV bremsstrahlung profiles. The result is shown in Fig. 2.5 (d). The absolute intensity calibration factor is expressed as a function of the number of observation chords in range of #50 to #204. The calibration factor remains a constant for chord numbers #60 to #204, which correspond to the plasma radius of $0 \leq \rho \leq 0.8$.

The constant calibration factor indicates a uniform reflectivity on the holographic grating along the direction perpendicular to the wavelength dispersion. The uniform reflectivity also guarantees the reliability of the vertical profile measured using the present space-resolved EUV spectrometer. Since the EUV bremsstrahlung intensity is low at the plasma edge even in high-density discharges, the analyzed data include a large uncertainty at the plasma edge. Therefore, the calibration factor is not plotted at $\rho > 0.8$.

The absolute intensity calibration factor is obtained against the wavelengths from 60 to 440 Å. The result is plotted in Fig. 2.6: open circles indicate high throughput values in the short wavelength region. Since bremsstrahlung intensity decreases with wavelength, the obtained calibration factor scatters in the long wavelength region. To compare the calibration factor between the original and upgraded systems, the data are fitted with the polynomial function. The result is plotted with dotted and solid lines in the figure indicating the original and upgraded systems, respectively. The calibration factor of the upgraded system shows a somewhat flatter distribution against wavelength than that of the original system. Although the reason is entirely unclear, the decrease in the throughput of the upgraded system in the short wavelength range of 60 to 200 Å may originate from a material contamination of the grating by carbon particles coming from LHD plasmas during the discharge. The uncertainty of the intensity calibration factor is estimated to be 18.3% from the statistical deviation of the calibration factor distribution. However, it is possible to improve this uncertainty, by accumulating bremsstrahlung signals for a longer sampling time in the steady phase of high-density discharges.

2.4 Performance improvement of 2-D impurity distribution measurement

2.4.1 Horizontal spatial resolution

The 2-D distribution of impurity line emissions is measured by horizontally scanning the observation chord with a horizontal stepping motor, while the vertical scanning is carried out with a vertical stepping motor. The horizontal spatial resolution of the space-resolved EUV spectrometer system can be calculated at a horizontal stepping motor speed of $V_{EUV} = 0$ as functions of incidence angle and grating size and curvature. In this study, the resolution is also experimentally determined using a toroidal slit (TS) installed between the LHD port and the spectrometer (see Fig. 2.3) [18].

The TS is located 6215 mm from the LHD plasma with R_{ax} = 3.75 m and 3087 mm from the entrance slit of the space-resolved EUV spectrometer. The toroidal slit consists of two flat plates with 1250 mm long vertical size and 700 mm wide horizontal size. Slit width and the slit horizontal position of the TS can be freely determined by horizontally moving the two plates independently. The horizontal aperture of the toroidal slit reaches the maximum width of 480 mm when the two plates are fully opened, while the minimum aperture width is 10 mm when the two plates are closed. In addition, the toroidal slit can be horizontally moved in the range of –240 mm ≤ Y_{TS} ≤

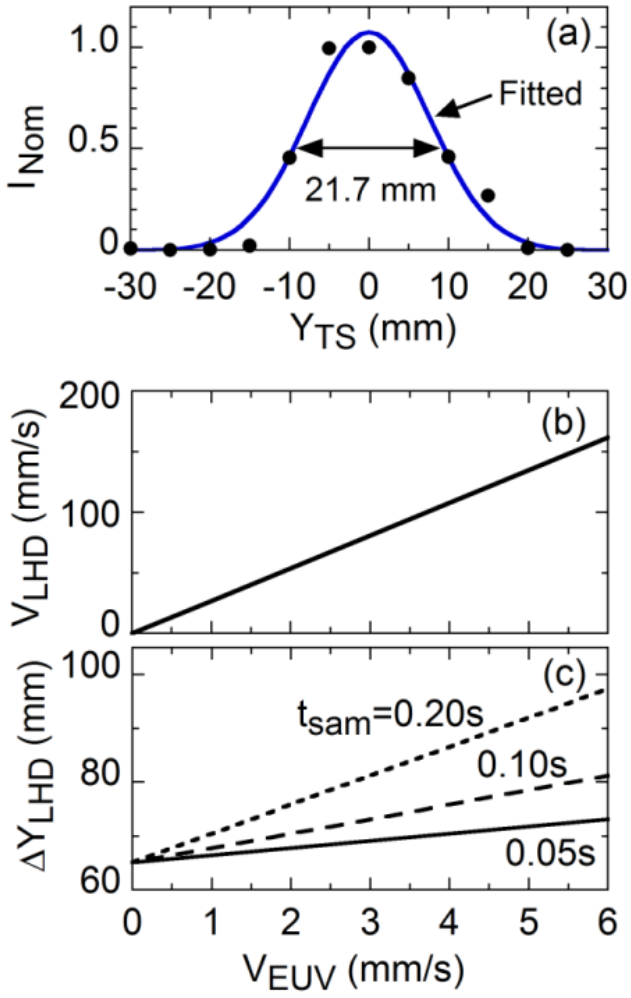

Fig. 2.7 (a) Normalized HeII (303.8 Å) intensity as a function of Y_{TS} measured by scanning the toroidal slit with the same horizontal aperture width, (b) horizontal scanning speed at plasma axis of R_{ax} = 3.75 m, V_{LHD}, and (c) horizontal spatial resolution (ΔY_{LHD}) as a function of V_{EUV}. ΔY_{LHD} is measured at three different CCD sampling times (t_{asm}). The horizontal spatial resolution of 21.7 mm at the toroidal slit position is obtained by fitting the data with the Gaussian curve.

240 mm during a discharge while keeping a constant aperture width, where Y_{TS} denotes the horizontal distance between the toroidal slit center and the central optical axis at θ = 0° (see Fig. 2.3). In the present calibration, the aperture width of 10 mm is used.

When the toroidal slit with a narrow aperture is horizontally scanned with the observation chord of the space-resolved EUV spectrometer fixed at θ = 0°, spectral intensity can be measured as a function of Y_{TS}. Figure 2.7 (a) shows the relative spectral intensity of HeII (303.8 Å) as a function of Y_{TS} in the range of $-30 \leq Y_{TS} \leq 30$ mm. The data are fitted with the Gaussian function, as denoted by the solid line. The full width at half maximum (FWHM) of 21.7 mm indicates a horizontal spatial resolution of the space-resolved EUV spectrometer system at the toroidal slit position. Since the distance between the entrance slit and the LHD plasma at R_{ax} = 3.75 m is 3.01 times larger than that between the entrance slit and the toroidal slit, the horizontal spatial resolution at R = 3.75 m in the LHD vacuum vessel is estimated to be 65.3 mm.

As the space-resolved EUV spectrometer has to be horizontally scanned to observe the 2-D distribution, the practical horizontal spatial resolution is slightly worse than that obtained above. The increment in horizontal spatial resolution can then be a function of the scanning speed of the observation chord. Therefore, the horizontal spatial resolution can be improved when the sampling time per frame is shorter [9]. The horizontal scanning speed of the observation chord at the plasma axis of LHD plasmas, V_{LHD}, is examined against V_{EUV}, as shown in Fig. 2.7 (b). The result confirms a good linear relationship between V_{EUV} and V_{LHD}. The horizontal spatial resolution during the 2-D distribution measurement is calculated as a function of V_{EUV} with the sampling time t_{sam}, as shown in Fig. 2.7 (c). It is clear that the horizontal spatial resolution is considerably lower when the sampling time of the CCD is reduced. A comparison of measured 2-D distributions between two CCDs with low and high frame rates is presented in Sect. 2.4.3.

2.4.2 Temporal evolution of impurity vertical profiles

The main impurity species in LHD plasmas are carbon and iron, which originate from the divertor plates and first wall, respectively. Helium emissions are always strong, which is affected by the ion cyclotron range of heating (ICRF) discharges with helium majority and the helium glow discharges [25]. The iron emission is considerably weaker than the carbon emission basically in all discharges owing to the effective impurity screening in the ergodic layer [5]. However, the iron emission from lower ionization stages obviously increases after hydrogen multi-pellet injection because the emission location moves from the plasma edge to the plasma core owing to a sudden temperature decrease [26,27].

To examine the temporal resolution of the upgraded EUV spectrometer system, the temporal behavior of FeXV (284.147 Å) vertical profiles is observed in n-NBI discharges with p-NBI modulation and hydrogen multi-pellet injection. The sampling time of the CCD is set to 50 ms. The space-resolved EUV spectrometer is fixed at θ = 0°, where the optical axis is perpendicular to the toroidal magnetic axis. A typical n-NBI discharge with p-NBI modulation and multi-pellet injection is shown in Fig. 2.8. The injection power of n-NBI is increased from 4.5 to 10 MW before injecting the pellet. Six hydrogen ice pellets are repetitively injected for t = 5.68 – 5.83 s. The electron

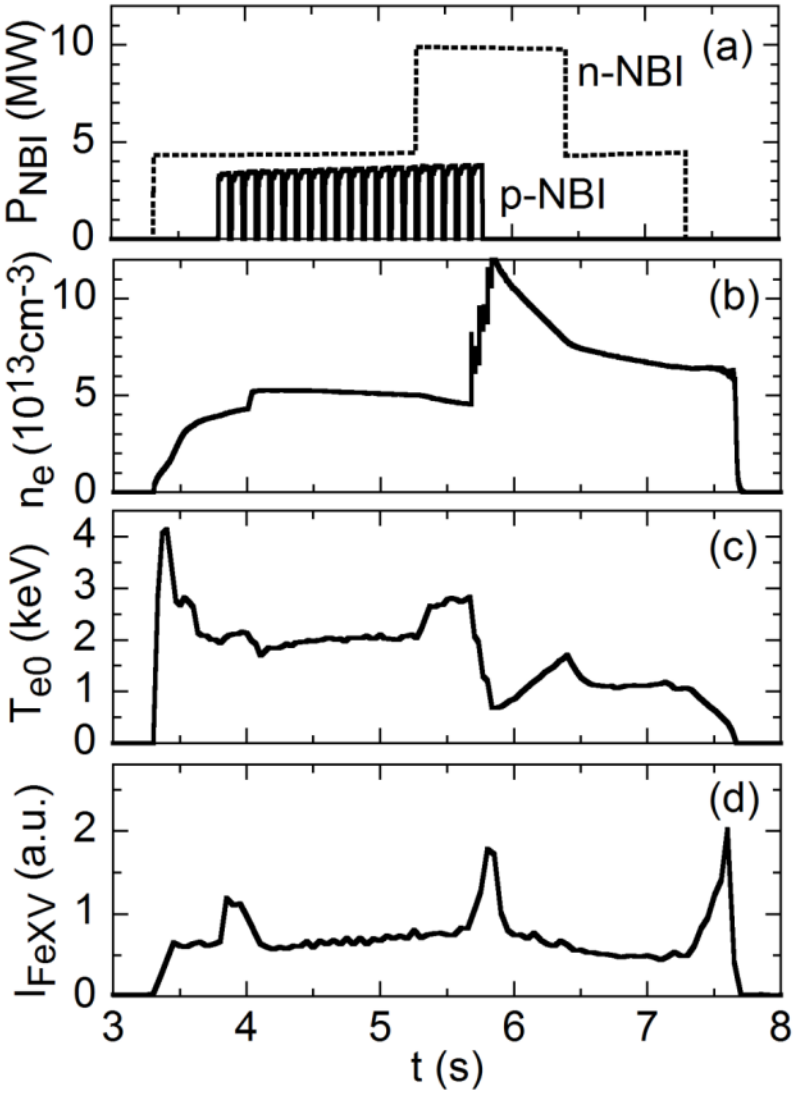

Fig. 2.8 Time behaviors of (a) n-NBI and p-NBI port-through power, (b) line-averaged electron density, (c) central electron temperature and (d) Fe XV (284.147 Å) intensity measured using space-resolved EUV spectrometer.

density sufficiently increases from 3.5×10^{13} to 1.3×10^{14} cm^{-3} after the final pellet injection [see Fig. 2.8 (b)]. In contrast, the electron temperature decreases step-by-step with each pellet injection and finally drops to 0.5 keV [see Fig. 2.8 (c)]. After the pellet injection, the electron temperature continuously recovers until the n-NBI power is reduced at t = 6.4 s. The time behavior of FeXV intensity is obtained by integrating the FeXV vertical profile along the whole vertical range of Z = 0 – 550 mm, as shown in Fig. 2.8 (d).

The p-NBI power is modulated by switching it off for 20 ms at time intervals of 100 ms until the pellet injection is finished. Figure 2.9 (a) shows an extended time

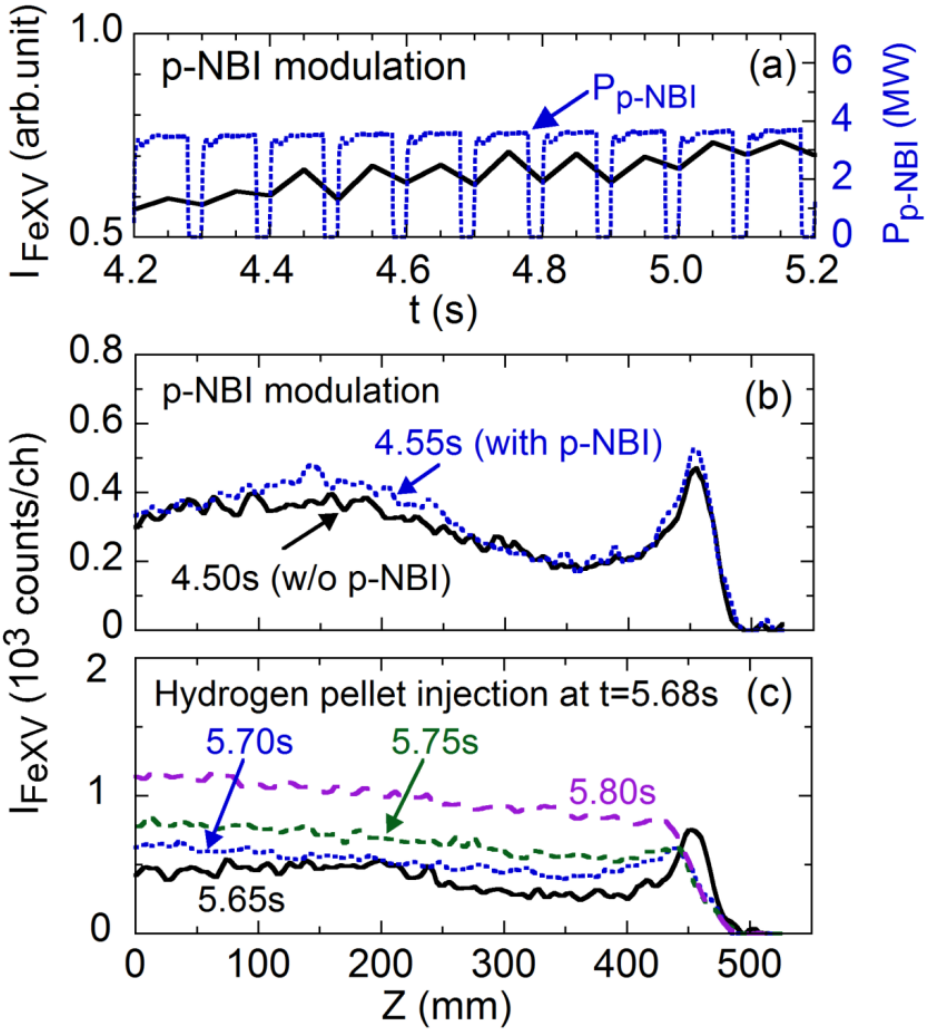

Fig. 2.9 (a) Time behavior of FeXV (284.147 Å) intensity measured using space-resolved EUV spectrometer during p-NBI modulation phase, vertical profiles of FeXV intensity (b) without (t = 4.50 s) and with (t = 4.55 s) p-NBI and (c) during hydrogen pellet injection phase (t = 5.65–5.80 s).

evolution of p-NBI port-through power and FeXV intensity. It is clear that the FeXV intensity responds to the p-NBI power modulation. The FeXV intensity quickly increases when the p-NBI power is switched on, suggesting an increased iron influx. The temporal behavior of FeXV vertical profiles during the p-NBI power modulation is shown in Fig. 2.9 (b) at t = 4.50 and 4.55 s. The two vertical profiles can be clearly distinguished from each other. This indicates a good time resolution in profile measurement. The edge peak of FeXV emission appearing at Z = 450 mm is enhanced by a relatively long emission volume along the observation chord, while the enhancement of FeXV emission at $0 \leq Z \leq 300$ mm is affected by the magnetic field structure in the vicinity of X-points (see Figs. 2.3 and 2.4).

As shown in Fig. 2.8 (d), the FeXV emission is slightly enhanced during the

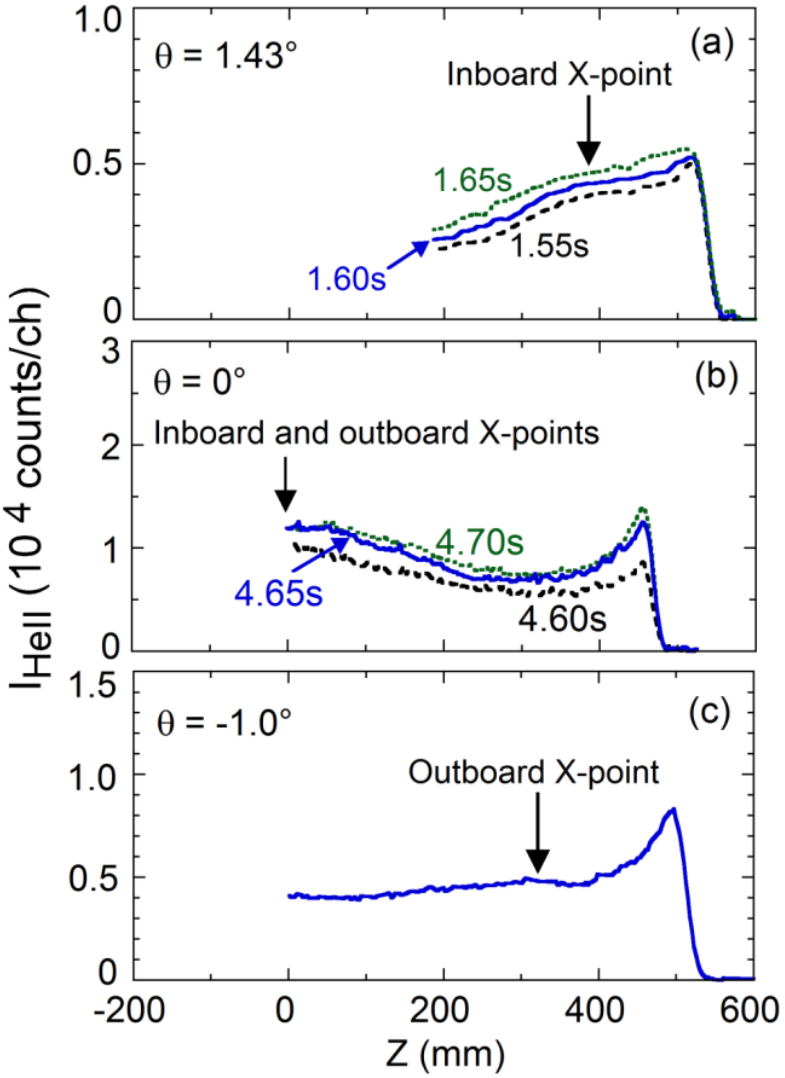

Fig. 2.10 Vertical profiles of HeII (303.78 Å) at (a) θ = 1.43, (b) 0 and (c) –1.0° at CCD sampling time of t_{sam} = 50 ms.

pellet injection. The time-developed vertical profile of FeXV during the pellet injection is shown in Fig. 2.9 (c) at t = 5.65 – 5.80 s with time intervals of 50 ms. After the pellet injection at t = 5.68 s the FeXV emission quickly starts to increase in the vicinity of the X-point, e.g., $0 \leq Z \leq 300$ mm, while the emission location from the O-point region at Z ~ 450 mm moves inside as a function of time, indicating that the plasma size is smaller. The temporal evolution of the vertical intensity profiles of FeXV with a sampling time of 50 ms can clearly exhibit a good time response during the pellet injection.

As mentioned in Sect. 2.2, the central observation chord in the full vertical profile passes through both the X-points in the inboard and outboard sides when the optical axis is perpendicular to the toroidal field ($\theta = 0°$). The observation of vertical profiles at different horizontal angles is required to distinguish the two X-points. The time evolution of HeII (303.78 Å) vertical profiles is measured at different horizontal angles. The result is shown in Figs. 2.10 (a) –2.10 (c) at different horizontal angles of θ = 1.43, 0 and –1.0°, respectively. Since the vertical profile is observed at different horizontal angles to measure the edge plasma boundary, the vertical observation range also changes as shown in the three figures. At $\theta = -1.0°$, unfortunately, the time evolution is not measured owing to lack of data. It is clear that the plasma boundary position shifts when the horizontal angle is changed. In particular, the plasma boundary largely shifts up to Z = 550 mm at $\theta = 1.43°$ owing to the poloidal turn of LHD elliptical plasmas (see Fig. 2.3). The position of X-points also changes at different toroidal angles, as denoted by arrows in the figures. Thus, it becomes possible to separately study the impurity structure at the outboard and inboard X-points.

2.4.3 2-D distribution measurement of impurity line emissions

In the previous study, the 2-D distribution in NBI discharges has been observed with the pulse length extended by connecting n-NBIs in tandem [9]. The waveform of tandem n-NBI discharges is shown in Fig. 2.11, which are operated with the magnetic axis position of R_{ax} = 3.75 m and the toroidal magnetic field of B_t = 2.64 T. As shown in Fig. 2.12 (a), the discharge is initiated by electron cyclotron heating (ECH) and maintained for approximately 8 s by connecting two n-NBIs (NBI#1 and #3) in tandem. Both these n-NBIs have a pulse length of 4 s and overlap for 200–500 ms at the middle of discharges. Another n-NBI (NBI#2) and two p-NBIs (NBI#4 and #5) are added at the end of discharges for ion source conditioning. The temporal evolutions of line-averaged electron density and central electron temperature are plotted in Figs. 2.12 (b) and 2.12 (c), respectively. The electron density gradually increases after replacing NBI#1 with NBI#3 reflecting a different input power, while it remains constant during the discharge duration of 0.5 to 4.0 s with NBI#1. As a result, the electron density changes with a slightly wide range of $4.5 \leq n_e \leq 6.5 \times 10^{13}$ cm^{-3} during t = 1.4–7.4 s

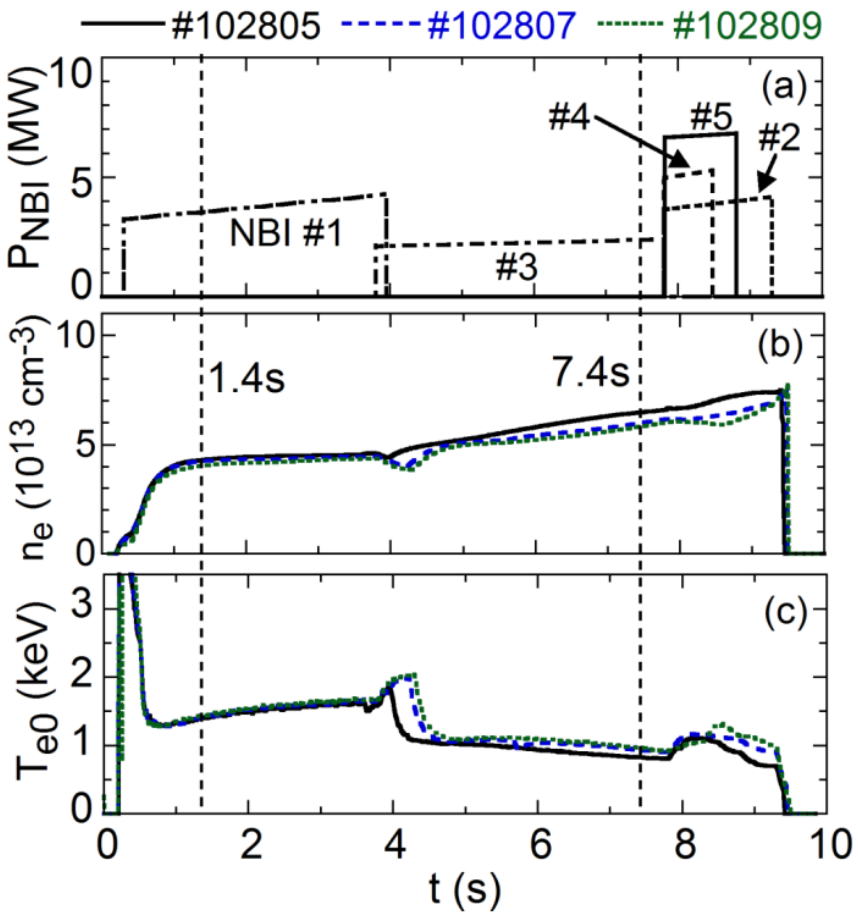

Fig. 2.11 Time behaviors of (a) NBI port-through power, (b) line-averaged electron density and (c) central electron temperature. The EUV spectrometer is horizontally scanned from t = 1.4 to 7.4 s in three successive discharges (solid, dashed and dotted lines) with n- and p-NBIs whose pulses are connected in tandem.

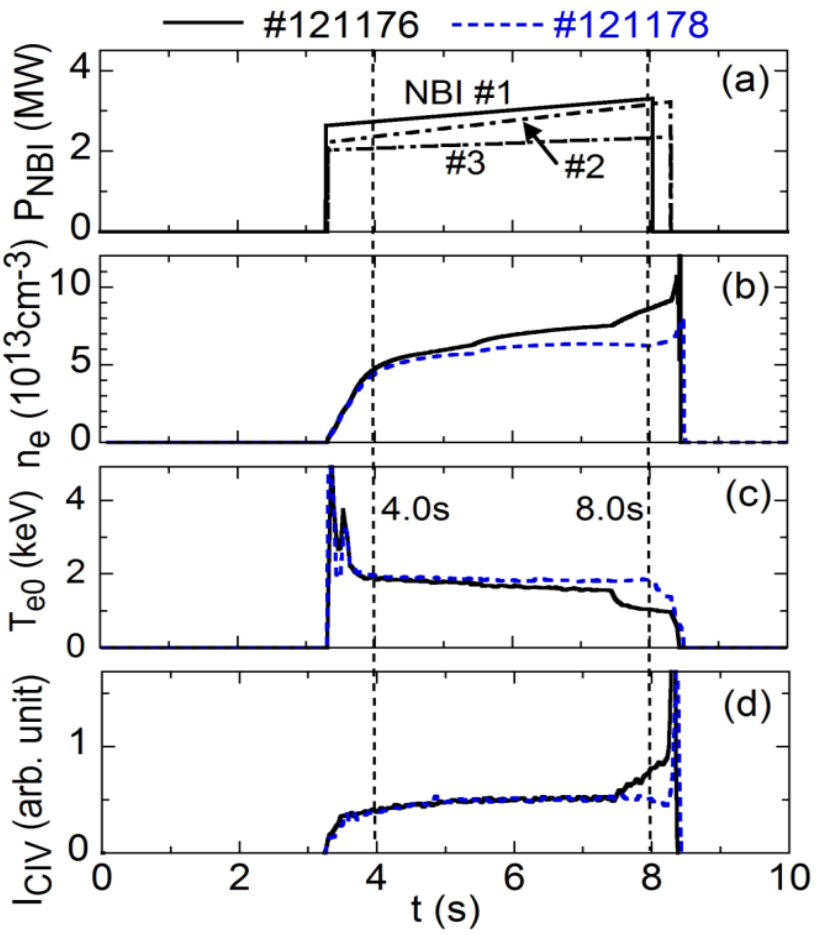

Fig. 2.12 Time behaviors of (a) NBI port-through power, (b) line-averaged electron density and NBI power, (c) central electron temperature and (d) CIV (384.02 Å) intensity measured using EUV_Long spectrometer in two successive NBI discharges (solid and dashed lines). The space-resolved EUV spectrometer is horizontally scanned from t = 4 to 8 s, denoted by two vertical dashed lines.

when the 2-D distribution is measured by scanning the spectrometer. However, the change in the density does not definitively affect the 2-D measurement compared with the change in electron temperature. It is quite difficult to maintain a constant electron temperature during the tandem NBI discharge, as plotted in Fig.2.11 (c). The n-NBI injection power must be reduced if the beam pulse is further extended, whereas the n-NBIs are usually operated at a pulse length of 2 s. The electron temperature in LHD is fairly sensitive to injection power when the density increases.

The 2-D distribution of CIV (312.4 Å: $1s^2 3p – 1s^2 2s$) is measured using the original system in the tandem-NBI discharge shown in Fig. 2.11 at a sampling time of 200 ms and V_{LHD} = 135 mm/s. The result is shown in Fig. 2.13 (a). Owing to the limited vertical observation range, the full vertical image of 2-D impurity distribution is completed by combining three partial images, which are taken at the upper ($100 \leq z \leq 600$ mm), middle ($-250 \leq z \leq 250$ mm) and lower ($-600 \leq z \leq -100$ mm) vertical

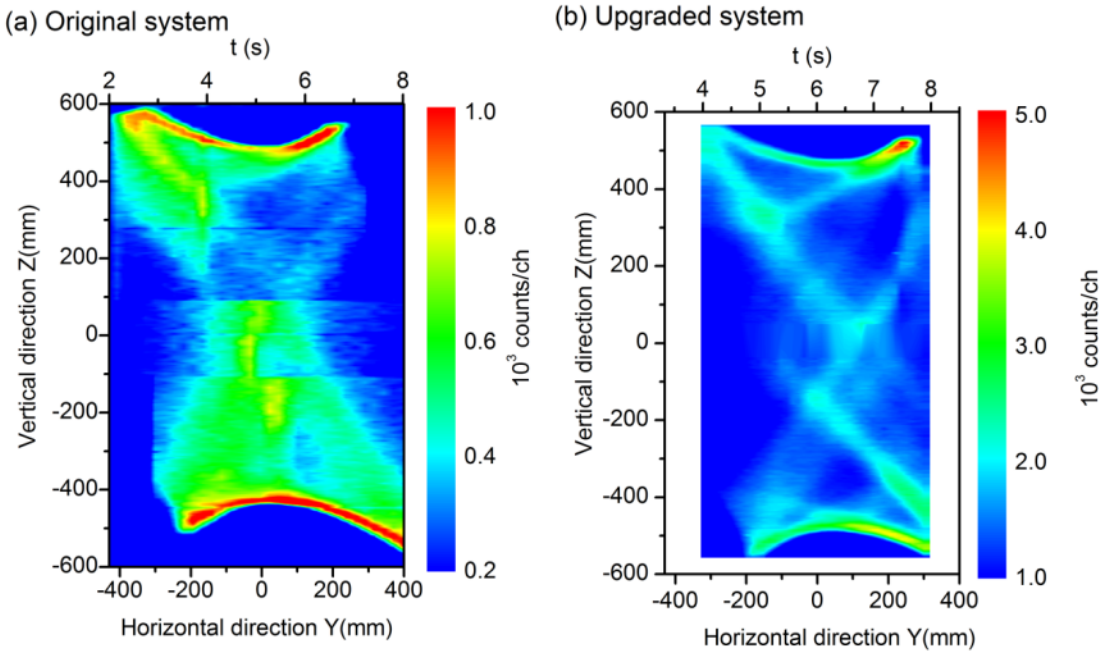

Fig. 2.13 2-D intensity distributions of (a) CIV (312.4 Å) reconstructed using three long-pulse NBI discharges (#102805, #102807 and 102809) in original system (t_{sam} = 200 ms) with lower scanning speed (V_{LHD} = 135 mm/s) and (b) CIV (384.02 Å) reconstructed using two short-pulse NBI discharges (#121176 and #121178) in upgraded system (t_{sam} = 100 ms) with higher scanning speed (V_{LHD} = 162 mm/s).

positions in three different discharges indicated by solid, dashed and dotted lines in Fig. 2.11, respectively. As shown in Fig. 2.13 (a), strong emissions are observed at the top ($500 \leq Z \leq 600$ mm) and bottom ($-400 \leq Z \leq -500$ mm) edges of plasmas. However, the structure of 2-D impurity distribution in the X-point region is entirely unclear owing to the poor spatial resolution in the horizontal direction, the emission variations among three discharges without good reproducibility and the temporal change in edge plasma parameters during discharges.

When the sampling time of the CCD is shortened and the horizontal scanning speed is increased, the 2-D distribution measurement from high-density NBI discharges with a short pulse is possible even when the tandem NBI discharge mentioned above is not adopted. Figure 2.12 shows the waveform of high-density NBI discharges of three overlapped n-NBIs. The same discharge conditions as those in Fig. 2.11 are chosen for direct comparison between the original and upgraded systems, i.e., R_{ax} = 3.75 m and B_t = 2.75 T. The three n-NBIs overlap during t = 3.3–8.0 s after initiating the plasma with ECH. The electron density shown in Fig. 2.12 (b) is slightly different between the two discharges denoted by solid and dashed lines, which are used for the 2-D distribution measurement, owing to a small breakdown in the negative ion source. The instant reduction in n-NBI power slightly increases the density and also decreases the temperature, as denoted by the solid line in Figs. 2.12 (b) and 2.12 (c). However, the discharge is relatively stable compared with the tandem NBI discharge shown in Fig. 2.11. Figure 2.12 (d) shows the temporal evolutions of CIV (384.02 Å, $1s^2 3d – 1s^2 2p$) measured using the EUV_Long spectrometer with a sampling time of 5 ms. It confirms a stable edge condition in the NBI discharge except at the end of the discharge after t = 7.4 s [see solid line in Fig. 2.12 (d)].

The 2-D distribution of CIV (384.02 Å) is measured using the upgraded system in the short-pulse NBI discharge shown in Fig. 2.12 with a shorter sampling time of 100 ms and a higher scanning speed of V_{LHD} = 162 mm/s. These operational parameters enable the horizontal scanning from Y = –340 mm to Y = 340 mm during the pulse duration of t = 4–8 s. For the purpose of reduction of scanning time, the scanning speed is increased by modifying a software setting. The result is shown in Fig. 2.13 (b). The 2-D measurement is completed with two discharges by optimizing the vertical observation range such as $-550 \leq Z \leq 0$ mm and $0 \leq Z \leq 550$ mm. The spatial resolution in the horizontal direction is significantly improved by reducing sampling time and increasing scanning speed. Compared with the image obtained using the original system, a detailed structure of the impurity emission is clearly shown, particularly, the diagonal structure of the X-point trajectory. The CIV emission traced from the top-left to bottom-right corner in Fig. 2.13 (b) indicates the X-point trajectory on the outboard side, while the X-point trajectory on the inboard side appears as the diagonal emission from the top-right to bottom-left corner. Thus, the image obtained using the upgraded

system clearly indicates the performance improvement of the space-resolved EUV spectrometer system.

The 2-D CIV distribution observed from low-density long-pulse ICRF discharges is also compared between the original and upgraded systems with sampling times of 200 and 50 ms, respectively. The result is shown in Fig. 2.14. Since the pulse length of ICRF discharges is large, e.g., 10 s, the 2-D distribution can be measured with a lower horizontal scanning speed of V_{LHD} = 108 mm/s and the horizontal observation range can also be extended to –430 ≤ Y ≤ 430 mm. Both the 2-D distributions in Fig. 2.14 are measured from ICRF discharges with identical plasma parameters of $n_e = 1 \times 10^{13}$ cm^{-3} and R_{ax} = 3.65 m. Since the density range in the ICRF discharge is considerably small, the observed X-point diagonal trajectory is entirely different from the result obtained in high-density NBI discharges (see Fig. 2.13). That is, the inboard X-point trajectory in high-density NBI discharges is split into two parts, while that in ICRF discharges simply shows a single trajectory. At present, the edge emission structure in the vicinity of X-points of the ergodic layer is not fully understood. A 3-D

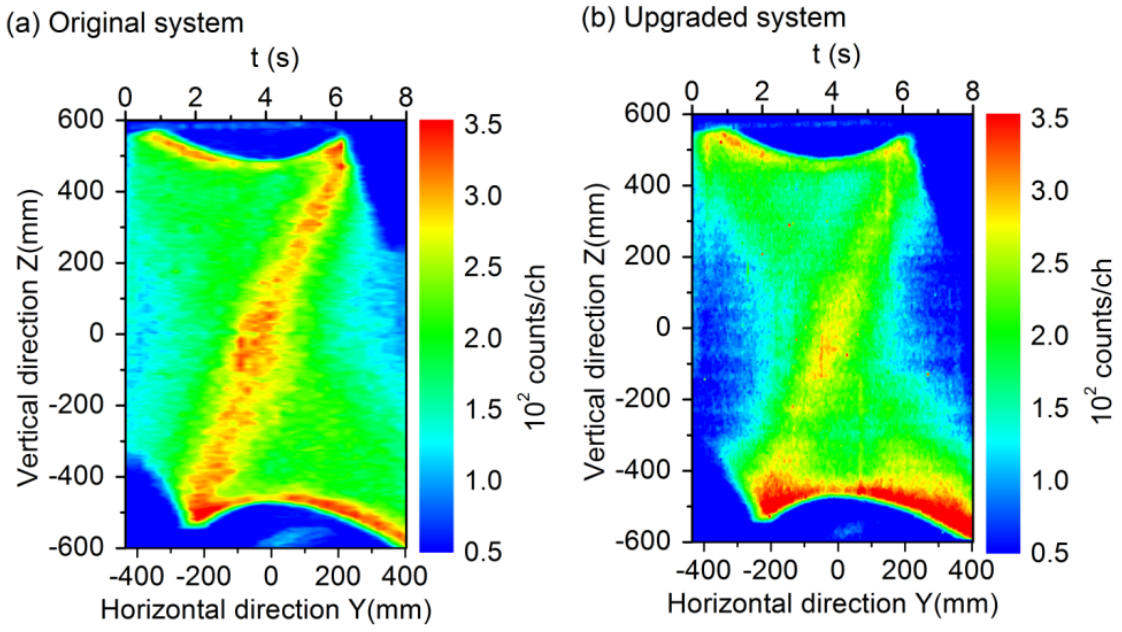

Fig. 2.14 2-D intensity distributions of (a) CIV (312.4 Å) reconstructed from two identical long-pulse ICRF discharges measured using original system (t_{sam} = 200 ms and V_{LHD} = 108 mm/s) and (b) CIV (384.02 Å) reconstructed from identical two long-pulse ICRF discharges measured using upgraded system (t_{sam} = 50 ms and V_{LHD} = 108 mm/s).

edge transport simulation code, EMC3-EIRENE, is being improved on the basis of the improved data obtained using the present upgraded spectrometer system.

2.4.4 Intensity normalization method

To reduce the effects of the shot-to-shot discharge variation on data reconstruction for plotting the 2-D distribution and temporal discharge variation during the horizontal scanning of the EUV spectrometer for measuring the toroidal distribution,

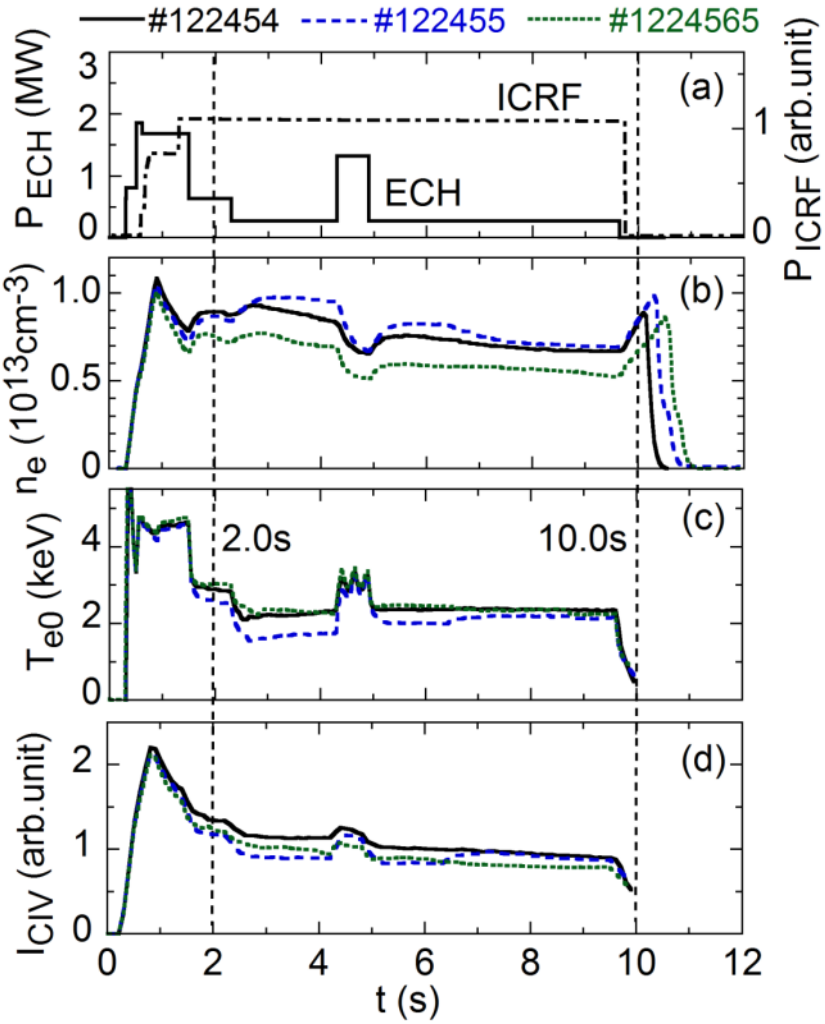

Fig. 2.15 Time behaviors of (a) ECH and ICRF pulses, (b) line-averaged electron density, (c) central electron temperature and (d) CIV (312.4 Å) intensity measured using EUV_Long spectrometer in three different ICRF discharges (solid, dashed and dotted lines). The EUV spectrometer is horizontally scanned from t = 2 to 10 s denoted by two vertical dashed lines.

an intensity normalization method is adopted in the 2-D image analysis. For this purpose, an impurity line emission recorded for the 2-D distribution is also simultaneously measured using the EUV_Long spectrometer with a high time resolution. Then, the raw data recorded for the 2-D distribution are normalized by the spectral intensity measured using the EUV_Long spectrometer before the 2-D distribution is reconstructed.

The intensity normalization method mentioned above is carried out in ICRF discharges associated with ECH heating at R_{ax} = 3.60 m and B_t = 2.75 T. Figure 2.15 shows the temporal behaviors of typical parameters in three consequent ICRF discharges. The full 2-D measurement of CIV (312.4 Å) is completed with the three discharges by changing the vertical angle, i.e., the upper half ($100 \leq z \leq 600$ mm: #122454), middle half ($-200 \leq z \leq 100$ mm: #122455) and lower half ($-600 \leq z \leq -200$ mm: #122456). A sudden increase in electron temperature appears during t = 4.3–4.9 s [see Fig. 2.15 (b)], which is caused by an increase in ECH injection power. With this increase, the CIV (312.4 Å) emission measured using the EUV_Long spectrometer with a sampling time of 5 ms also increases, as shown in Fig. 2.15 (d), while the density decreases, as shown in Fig. 2.15 (b). The space-resolved EUV spectrometer is horizontally scanned during t = 2–10 s to measure the 2-D distribution. During the spectrometer scanning, the CIV emission temporally changes the intensity and the intensity also varies among the three discharges [see Fig. 2.15 (d)].

The temporal CIV signal measured using the space-resolved EUV spectrometer, I_{SR_EUV}, is normalized by the temporal CIV signal measured using the EUV_Long spectrometer, I_{EUV_Long}. The I_{EUV_Long} shown in Fig. 2.15 (d) is already normalized by the maximum signal value observed during the scan, $I_{EUV\_Long\_max}$. Here, it is expressed by

$$I_{2D}(t,Z) = I_{SR\_EUV}(t,Z) / (I_{EUV\_Long}(t) / I_{EUV\_Long\_max}). \qquad (2.2)$$

The 2-D distribution analyzed without and with intensity normalization is shown in Figs. 2.16 (a) and 2.16 (b), respectively. The effect of a sudden increase in CIV intensity during t = 4.3–4.9 s entirely disappears in the 2-D distribution when the intensity normalization method is adopted [see Fig. 2.15 (b)], while the effect clearly appears at $-200 \leq Y \leq -150$ mm in Fig. 2.15 (a). The temporal intensity variation during a discharge can be effectively reduced when the intensity normalization method is applied. The effect of intensity normalization is also observed near the X-point trajectory enhanced at the inboard side, as shown in Fig. 2.16 (b) with a bright diagonal CIV trajectory from Z = 440 mm and Y = 200 mm to X = –500 mm and Y = –200 mm.

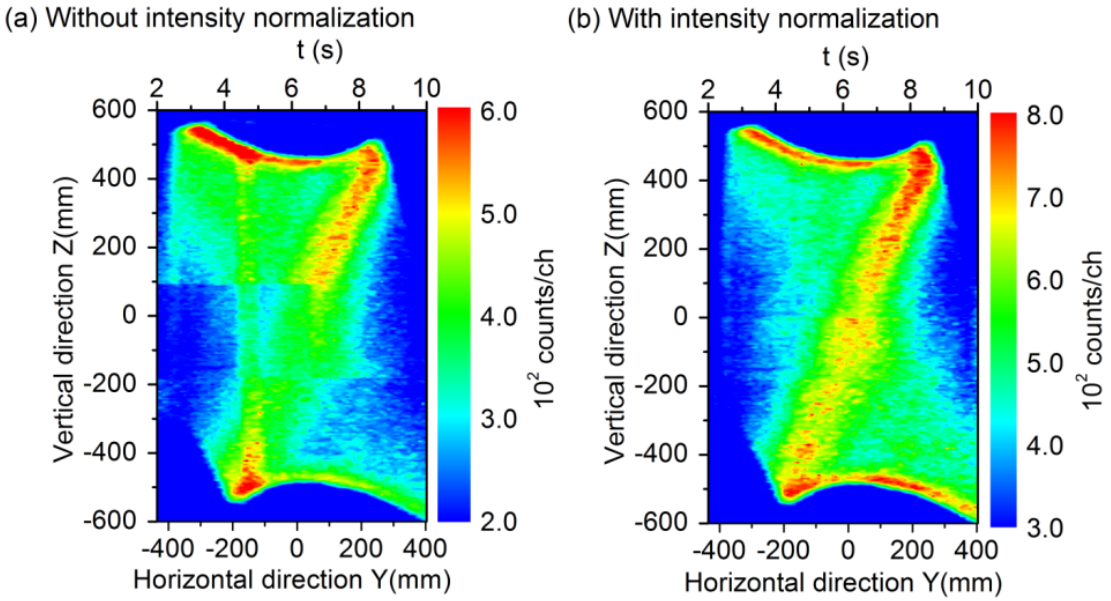

Fig. 2.16 2-D intensity distributions of CIV (312.4 Å) reconstructed from three long-pulse ICRF discharges (#122454, #122455 and #122456) (a) without and (b) with intensity normalization. The space-resolved EUV spectrometer system is operated with t_{sam} = 100 ms and V_{LHD} = 162 mm/s.

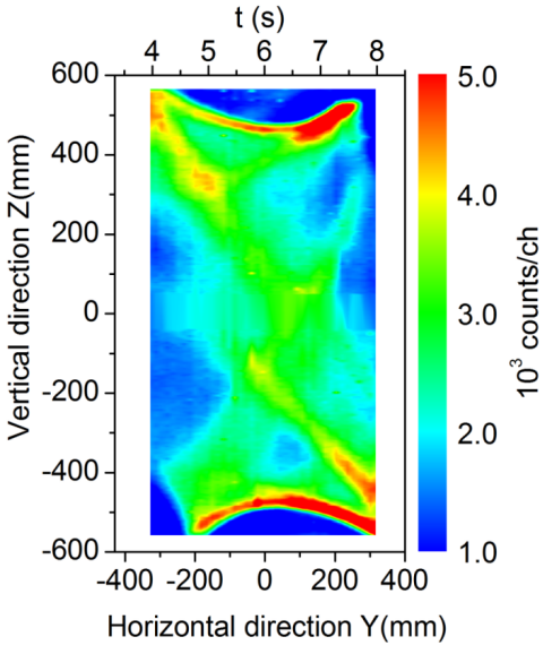

Fig. 2.17 2-D intensity distribution of CIV (384.02 Å) analyzed with intensity normalization method based on two short-pulse NBI discharges (#121176 and #121178).

This means the shot-to-shot intensity variation can also be minimized by the intensity normalization method.

The intensity normalization is also carried out for short-pulse NBI discharges. The CIV 2-D distribution shown in Fig. 2.17 is reconstructed with intensity normalization from #121176 and #121178 discharges. Then, the present result can be directly compared with those in Fig. 2.13 (b) reconstructed without intensity normalization. The temporal CIV intensity variation shown in Fig. 2.12 (d) is well compensated for by the intensity normalization. In particular, the enhanced emission trajectories in the top and bottom edges become clear at $-200 \leq Y \leq 50$ mm. Thus, it can be well demonstrated that the intensity normalization method is quite important for obtaining high-quality 2-D images of impurity line emissions.

2.4.5 Reduction in high-energy neutral particle noise using PET filter

In LHD, a large amount of spike noise has been observed in the EUV spectrum in NBI discharges. In particular, the noise is enhanced in low-density NBI discharges owing to a long slowing down time. The spike noise is caused by high-energy neutral particles originating from high-energy hydrogen beam ions from NBIs [28,29]. High-energy neutral particles can reach the CCD sensor after passing through the entrance slit and scattering on the grating. A 0.15 μm carbon filter has been installed in front of the entrance slit of the space-resolved EUV spectrometer to eliminate the neutral particles coming out of NBI discharges and the effect of NBI beams on the EUV spectrum has been examined by analyzing the pulse height of spike noises. As a result, the spike noise has been reduced by one order of magnitude [28]. However, the particle noise still remains in the spectrum because the carbon filter is considerably thin for particle elimination because of difficulty in thicker carbon filter production. To upgrade the spectrometer system performance, therefore, a 0.5 μm PET filter is adopted instead of the 0.15 μm carbon filter.

The percentage transmittance of the 0.5-μm-thick PET filter is shown in Fig. 2.18 (a) as a function of wavelength. As the filter material consists of carbon and oxygen in addition to hydrogen, K-edge absorption of carbon and oxygen occurs at 43.8 and 22.5 Å, respectively. Although the transmittance basically decreases with wavelength, it largely recovers above 43.8 Å owing to the carbon K-edge absorption. Therefore, the filter is practically applicable to the present EUV spectroscopy in the wavelength range of $30 \leq \lambda \leq 100$ Å. The particle penetration depth of the PET filter is calculated against protons as a function of energy, as shown in Fig. 2.18 (b) [30,31]. In the figure, the positions of p-NBI and n-NBI are denoted by dashed lines at 40 and 180 keV, respectively, in addition to the thickness of the PET filter denoted by a solid line. The particle penetration depth of 40 keV protons in the PET filter is also 0.5 μm.

Therefore, the present 0.5 μm PET filter can entirely block the high-energy neutral particles from p-NBIs. On the other hand, the present filter thickness still seems to be insufficient for the high-energy neutral particles from n-NBIs, the penetration depth of which is 1.6 μm. However, the energy of neutral particles coming out from plasmas is considerably reduced compared with the initial beam energy of 180 keV, because the high-energy protons, confined in plasmas, mainly dissipate the energy to bulk electrons through the collision. In addition, neutral hydrogen already changes the angle through inelastic scattering when it passes through the filter. If the change in the angle is large, neutral particles cannot enter the CCD after reflection on the grating.

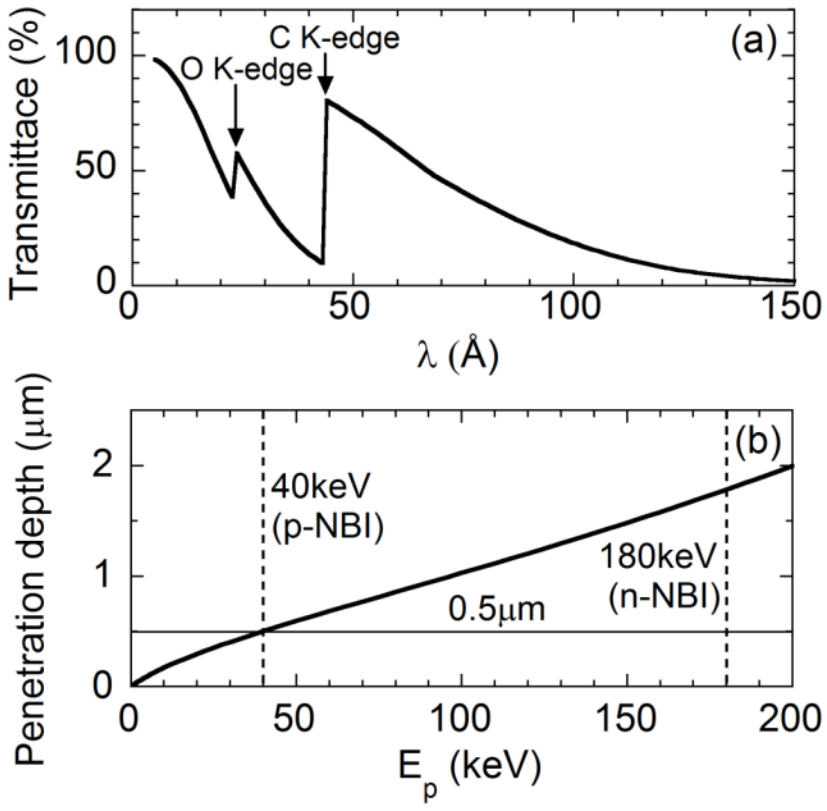

Fig. 2.18 (a) Transmittance of 0.5-μm-thick PET filter as a function of wavelength and (b) penetration depth as a function of incident proton energy. Beam energies of perpendicularly injected p-NBI (positive-ion-source-based NBI) and tangentially injected n-NBI (negative-ion-source-based NBI) are denoted by vertical dashed lines at 40 and 180 keV, respectively.

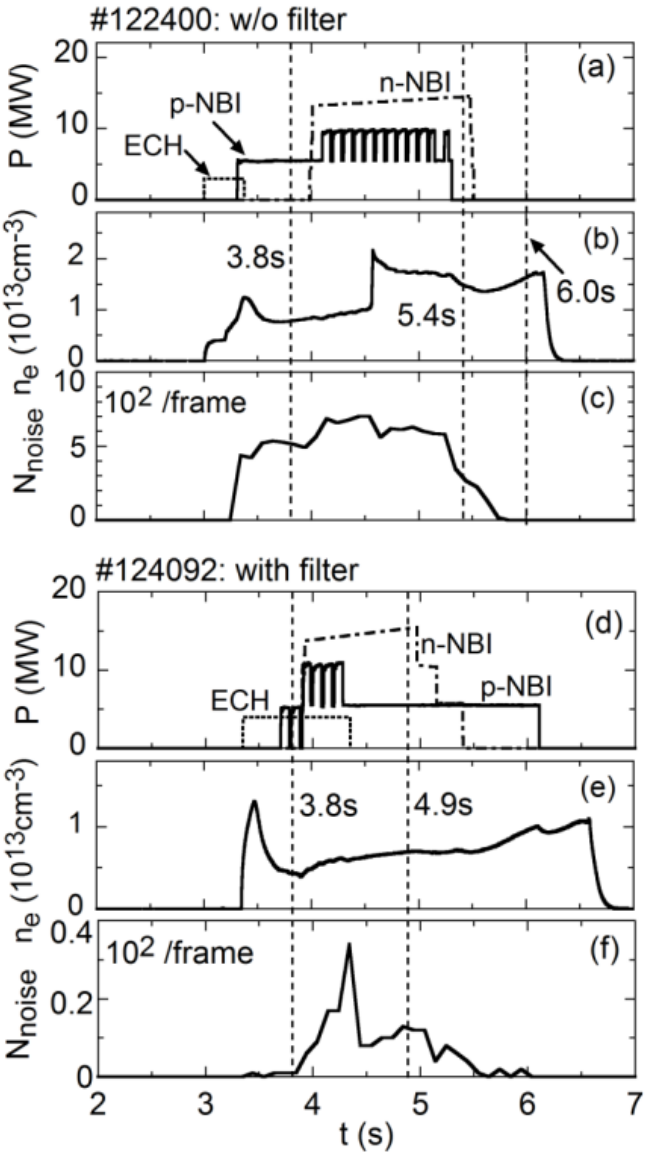

Fig. 2.19 Time behaviors of (a) port-through power of n- and p-NBIs, (b) line-averaged electron density and (c) number of spike noises per CCD frame in the case without filter and (d) port-through power of n- and p-NBIs, (e) line-averaged electron density and (f) the number of spike noises per CCD frame in the case with filter. Vertical dashed lines indicate the time at which spectral images are compared, as shown in Fig. 2.20.

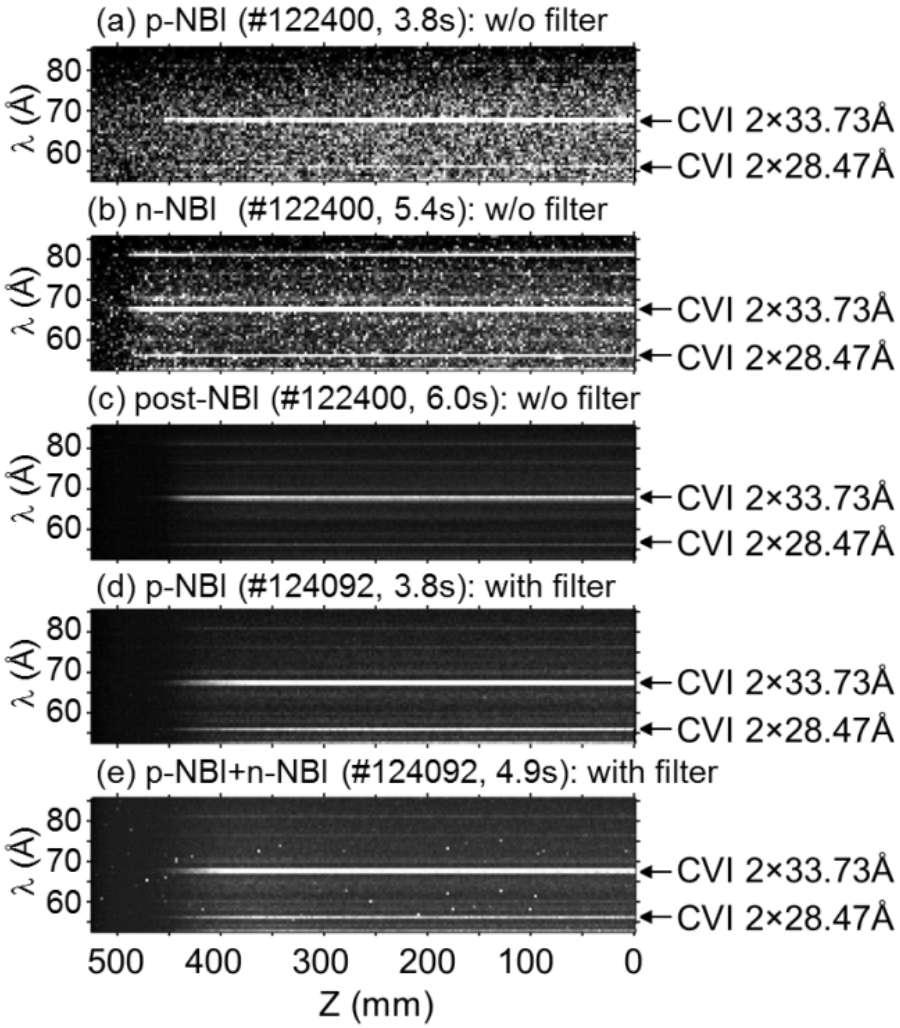

Fig. 2.20 Spectral images of 2nd order of CVI at 28.47 and 33.73 Å (a) during p-NBIs and (b) n-NBIs and (c) after switching off NBIs (post-NBI) in the case without PET filter [see t = 3.8, 5.4 and 6.0 s in Figs. 2.19 (a)–(c)] and (d) during p-NBIs and (e) n- and p-NBIs in the case with PET filter [see t = 3.8 and 4.9 s in Figs. 2.19 (d) – (f)].

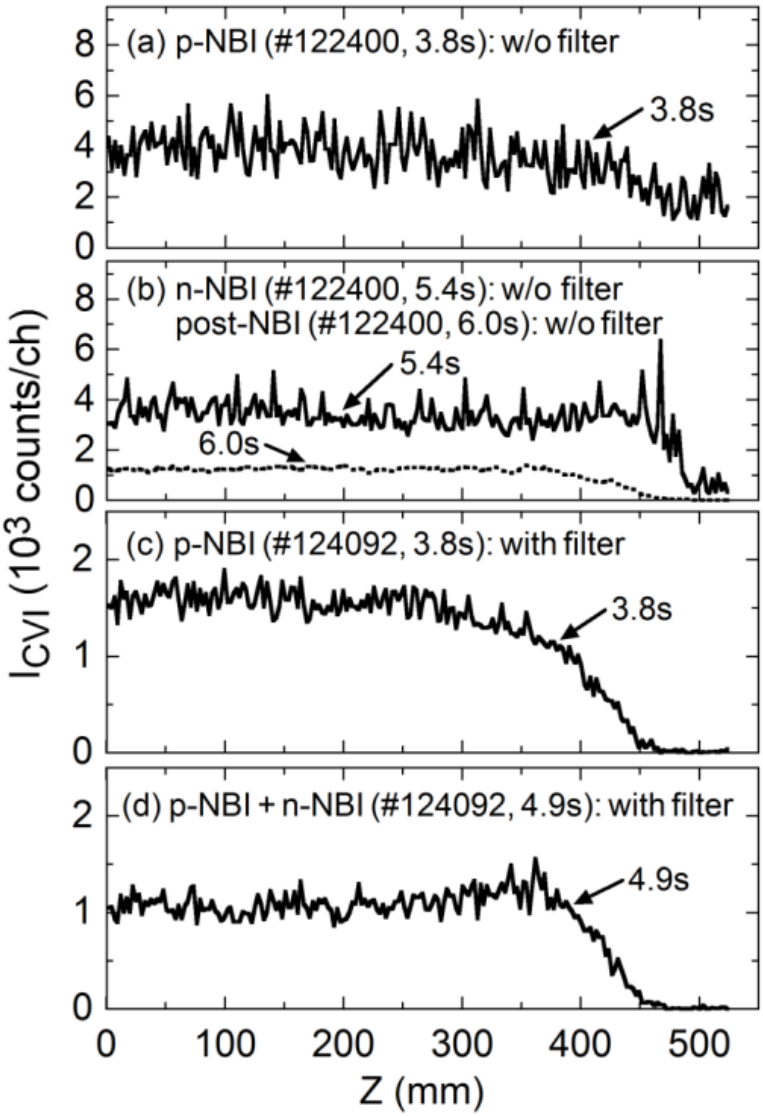

Fig. 2.21 Vertical profiles of CVI (2 × 28.47 Å) (a) during p-NBIs (t = 3.8 s) and (b) n-NBIs (t = 5.4 s: solid line) and after switching off NBIs (t = 6.0 s: dashed line) in the case without PET filter [see Figs. 2.20 (a)–2.20 (c)] and (c) during p-NBIs (t = 3.8 s) and (d) p- and n-NBIs (t = 4.9 s) in the case with PET filter [see Figs. 2.20 (d) and (e)].

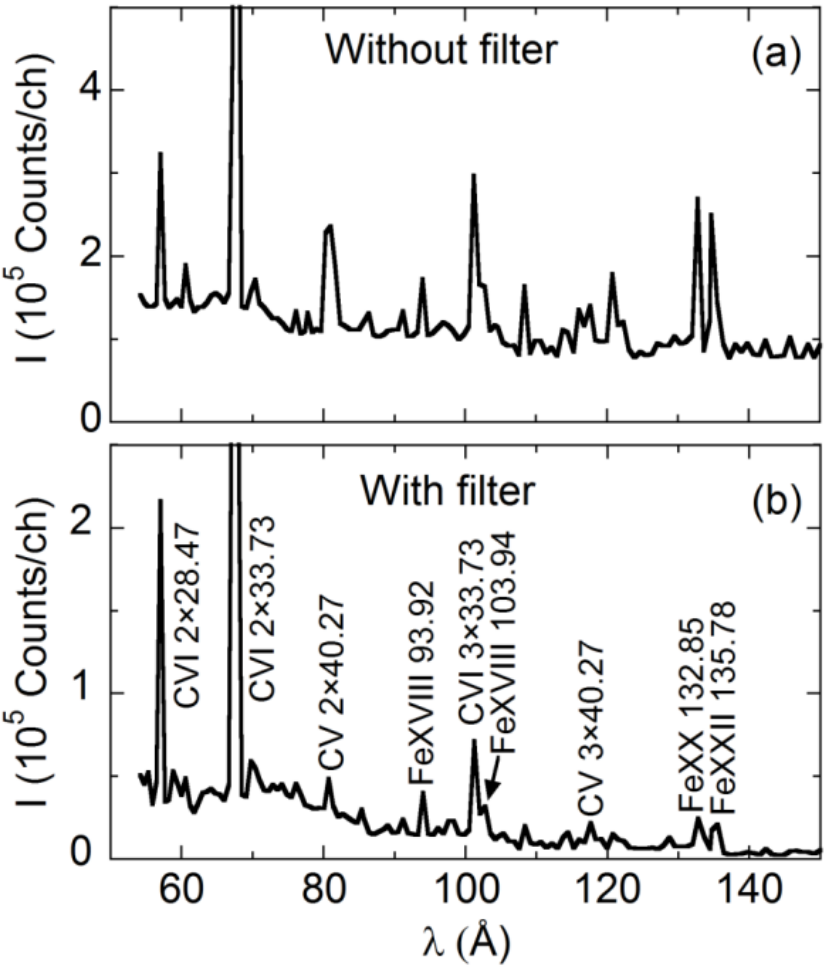

Fig. 2.22 Wavelength spectra measured using space-resolved EUV spectrometer (a) without and (b) with PET filter. The spectra are composed of several different NBI discharges.

The vertical profile is measured from low-density NBI discharges without installing the filter. The temporal evolutions of NBI injection power, electron density and the number of spike noises per CCD frame are shown in Figs. 2.19 (a)–2.19 (c), respectively. After switching off the n-NBI at t = 5.5 s, the discharge is still sustained for 0.7 s owing to a long beam slowing down time, which is a typical characteristic of the low-density NBI discharge. A vertical CIV profile is observed from the discharge in the second order (2 × 28.47 Å, 3p–1s). A CCD image in the wavelength range of $53 \leq \lambda \leq 86$ Å measured at t = 3.8, 5.4 and 6.0 s is shown in Figs. 20 (a)–(c), respectively. A large number of spike noises are observed in the CCD image at the p-NBI phase (t = 3.8 s) and n-NBI phase (t = 5.4 s), while the spike noise entirely disappears from the image after switching off the NBIs off at t = 6.0 s. The spike noise shown in Figs. 2.20 (a) and 2.20 (b) involves a variety of brightness. This suggests the neutral particle detected with the CCD has a wide energy distribution because the number of charges generated in the CCD is basically proportional to the energy of particles. The vertical profile of CVI obtained from Figs. 2.20 (a)–(c) is plotted in Figs. 2.21 (a) and 2.21 (b). The large amplitude in the profile at t = 3.8 s and 5.4 s is almost caused by the spike noise. In contrast, it is clear that the vertical profile at t = 6.0 s indicates a real CVI profile without inclusion of any spike noise.

After installing the PET filter, the vertical profile of CVI is also measured from low-density NBI discharges. The temporal evolutions of NBI injection power, electron density and the number of spike noises per CCD frame are shown in Figs. 2.19 (d)–(f), respectively. The CCD image obtained from the discharge is plotted in Figs. 2.20 (d) and 2.20 (e) for the p-NBI phase (t = 3.8 s) and p- and n-NBI phase (t = 4.9 s), respectively. By comparison with Figs. 2.20 (a) and 2.20 (d), the spike noise in Figs. 2.20 (d) and 2.20 (e) in the case of using the PET filter is considerably reduced in the CCD image. In particular, the spike noise originating from p-NBIs can be fully suppressed in the image [see Fig. 2.20 (d)]. The suppression of spike noise can also be clearly seen in the number of spike noises shown in Figs. 2.19 (c) and 2.19 (f). Here, note that the vertical unit in the noise count is markedly different between Figs. 2.19 (c) and 2.19 (f). Although a small number of spike noises, which originate from the n-NBIs, still remain in the CCD image at Fig. 2.20 (e), the effect on the CVI profile measurement is negligibly small. A remarkably important thing is that the brightness of all spike noises remaining in the CCD image in Fig. 2.20 (e) is sufficiently high, and the spike noise with low brightness entirely disappears from the CCD image, whereas the spike noise appearing in Fig. 2.20 (b) has a variety of brightness. This strongly suggests that only neutral particles with sufficiently high energies reach the CCD after penetrating the filter. For example, the spike noise count from the n-NBIs with a beam energy of 180 keV is reduced to 1/20 by the PET filter, while the spike noise from p-NBIs with a beam energy of 40 keV is perfectly suppressed. These results are fairly

reasonable when taking into account the penetration depth of neutral particles shown in Fig. 2.18 (b).

The vertical profile of CVI is plotted in Figs. 2.21 (c) and 2.21 (d) for the p-NBIs phase (t = 3.8 s) and p- and n-NBI phase (t = 4.9 s), respectively. The signal fluctuation in the vertical profiles is significantly reduced compared with that shown in Figs. 2.21 (a) and 2.21 (b) without the filter. It also indicates that the present filter works well to eliminate the spike noise, because the signal fluctuation is caused by the spike noise of various energies.

The vertical profile measured using the space-resolved EUV spectrometer in the wavelength range of $54 \leq \lambda \leq 150$ Å is converted to the wavelength spectrum, as shown in Fig. 2.22. The vertical profile is usually recorded in the binning mode to reduce the sampling time. In the present measurement, five pixels are summed and converted into a single channel. Then, the spectral resolution in the wavelength spectrum shown in Fig. 2.22 is considerably low. The high baseline seen in the spectrum without the filter in Fig. 2.22 (a) is entirely due to the spike noise. Some line emissions, e.g., CV at 2×40.27 Å, are also affected by the spike noise, which blends with the line emission in the same channel. The result also indicates that the use of the 0.5-m-thick PET filter is extremely helpful in eliminating the spike noise.

2.5 2-D impurity line emission distributions with performance improvement

High-resolution 2-D distribution of various impurity line emissions has been measured using the upgraded space-resolved EUV spectrometer system. Typical examples of the 2-D distributions are shown in Figs. 2.23 (a) and 2.23 (b), which are observed in low-density long-pulse ICRF discharges (R_{ax} = 3.60 m, B_t = 2.75 T) at $n_e = 1 \times 10^{13}$ cm^{-3} for HeII (303.78 Å, E_i = 54.42 eV) and CVI (2×33.73 Å, E_i = 490.0 eV), respectively. These images are taken at a sampling time of 100 ms and a horizontal scanning speed of V_{LHD} = 108 mm/s. Since the emission of HeII is very large in the ICRF discharge with H minority and He majority, the signal-to-noise ratio is extremely high. The helium emission is mainly localized at the bottom edge, indicating an asymmetric profile. The diagonal X-point trajectory also shows an asymmetric profile enhanced at the lower half. In the CVI emission, on the other hand, the profile is entirely symmetric. The difference between HeII and CVI profiles is caused by a difference in the radial location mainly determined by the ionization energy. The HeII emission with a small E_i is located in the outer edge of the ergodic layer, while the CVI emission with a relatively large E_i is located in the vicinity of LCFS. A specific edge

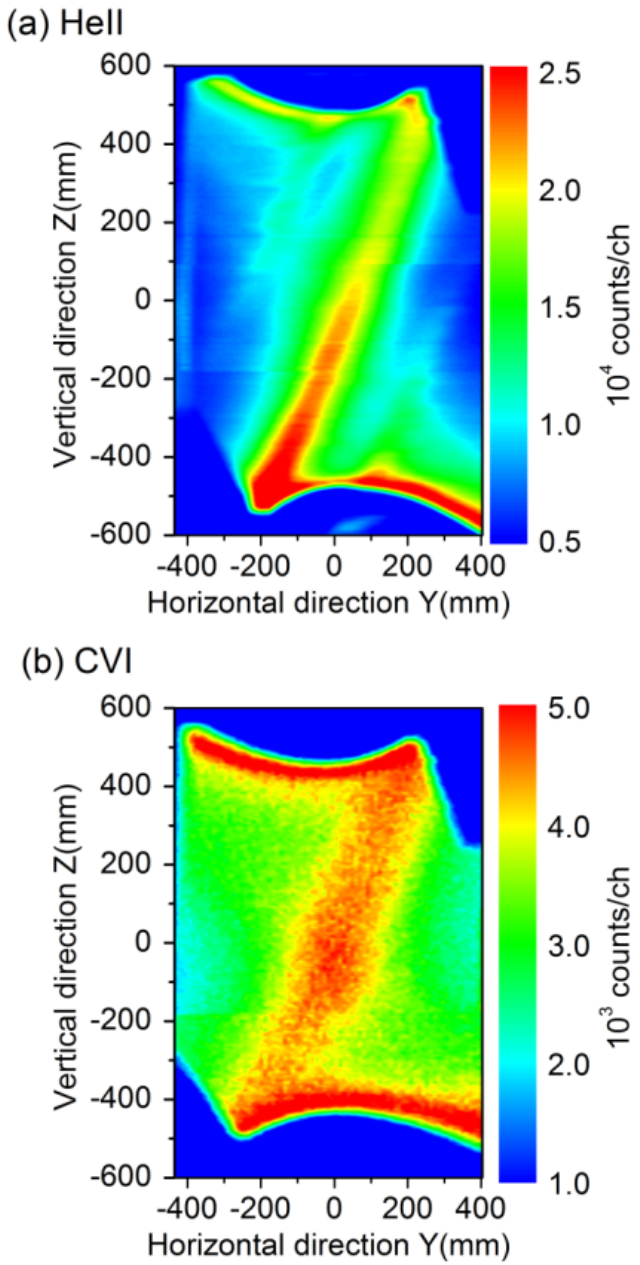

Fig. 2.23 2-D intensity distributions of (a) HeII (303.78 Å) and (b) CVI (2 × 33.73 Å) measured at horizontal scanning speed of V_{LHD} = 108 mm/s and CCD sampling time of t_{sam} = 100 ms.

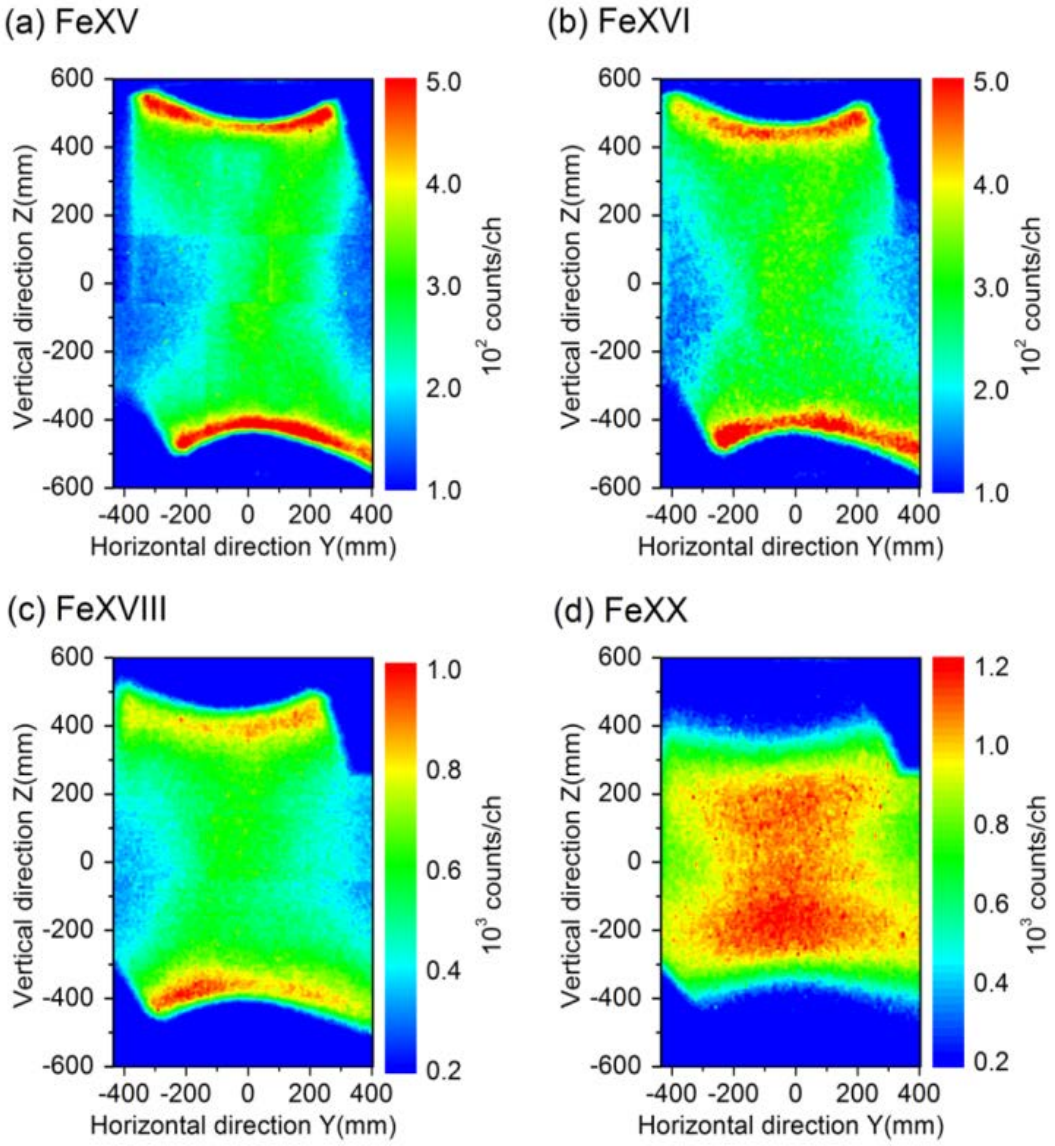

Fig. 2.24 2-D intensity distribution of (a) FeXV (284.147 Å: E_i = 456.2 eV), (b) FeXVI (335.4 Å: E_i = 489.3 eV), (c) FeXVIII (93.92 Å: E_i = 1357.8 eV) and (d) FeXX (132.85 Å: E_i = 1575.6 eV) measured at horizontal scanning speed of V_{LHD} = 108 mm/s and CCD sampling time of t_{sam} = 100 ms.

impurity transport is strongly suggested in both the 2-D distributions reflecting a 3-D magnetic field structure in the ergodic layer.

A few examples of the 2-D distributions are also shown in Figs. 2.24 (a) – 2.24 (d), which are observed in low-density long-pulse ICRF discharges (R_{ax} = 3.65 m, B_t = 2.75 T) at $n_e = 1 \times 10^{13}$ cm^{-3} for FeXV (284.147 Å, E_i = 456.2 eV), FeXVI (335.4 Å, E_i = 489.3 eV), FeXVIII (93.92 Å, E_i = 1357.8 eV) and FeXX (132.85 Å, E_i = 1582 eV), respectively. It should be noted that the magnetic axis position is different between Figs. 2.23 and 2.24. Data are taken at a sampling time of 100 ms and a horizontal scanning speed of V_{LHD} = 162 mm/s. The emissions of FeXV, FeXVI and FeXVIII are enhanced at both the top and bottom edges, basically owing to a relatively long integration of line emissions along the observation chord, while the FeXX emission is strong in the plasma core, reflecting the large E_i of 1582 eV. When the radial location of iron emissions is carefully checked among different ionization stages, it is found that the location is in agreement with the ionization energy. An important thing noted in the figure is that the diagonal X-point trajectory almost disappears from the 2-D distribution, whereas the ionization energies of FeXV and FeXVI are similar to that of CVI. This is probably caused by the difference in the magnetic axis position. In LHD, the edge magnetic field structure, particularly the divertor leg structure, markedly changes between R_{ax} = 3.66 and 3.70 m [10]. The difference in the X-point divertor trajectory between Figs. 2.23 and 2.24 seems to reflect a specific edge impurity transport as determined from the different structure of magnetic fields connecting the divertor leg.

2.6 Summary

The performance of the 2-D space-resolved EUV spectrometer system has been successfully upgraded by installing a high-frame-rate CCD and PET filter, increasing the horizontal scanning speed and adopting an intensity normalization method.

The upgraded space-resolved EUV spectrometer is absolutely calibrated on the basis of the profile measurement of visible and EUV bremsstrahlung continuum, and the calibration factor is obtained as a function of wavelength in the range of 60–440 Å. The calibration factor of the present upgraded system is comparable to that of the original system.

Since the high-frame-rate CCD can be operated with a relatively short sampling time of 50 ms for the 2-D measurement, the horizontal spatial resolution is significantly improved. With the increase in horizontal scanning speed, the 2-D distribution measurement is applicable to NBI discharges of short pulse length. As a result, a

detailed structure of the 2-D impurity emission distribution along the X-point trajectory is clearly observed in the NBI discharge.

The intensity normalization method is adopted for the data analysis of 2-D images of impurity emissions by measuring the temporal behavior of line emissions using another EUV spectrometer. The effects of temporal intensity variation during a discharge and shot-to-shot intensity variation among two or three discharges on the 2-D image reconstruction can be almost eliminated.

A 0.5-μm-thick PET filter is installed in front of the entrance slit of the space-resolved EUV spectrometer to reduce the spike noise induced by high-energy neutral particles in NBI discharges. The PET filter can perfectly block neutral particles originating from 40 keV p-NBIs. It can also slightly change the direction of neutral particles originating from 180 keV n-NBIs. As a result, the spike noise is almost eliminated from the EUV spectrum in NBI discharges.

Thus, the 2-D intensity distributions of helium, carbon and iron impurity ions are excellently observed with good quality. The iron distribution observed in the core plasma shows that the iron ion localizes at a certain radial position according to its ionization energy as a function of magnetic surface, while the helium and carbon distributions observed in the ergodic layer show an asymmetric profile. All the impurity distributions obtained with the present upgraded spectrometer system clearly indicate an improved performance of this system compared with that of the original system. The upgraded system realized through this work shows a sufficient performance for the edge impurity transport study.

References

[1] T. Satow, et al., Fusion Eng. Des. **20,** 67 (1993).
[2] A. Iiyoshi, et al., Fusion Sci. Technol. **17**, 169 (1990).
[3] T. Morisaki, et al., J. Nucl. Mater. **313**, 548 (2003).
[4] N. Ohyabu, et al., Nucl. Fusion **34**, 387 (1994).
[5] S. Morita, et al., Nucl. Fusion **53**, 093017 (2013).
[6] S. Masuzaki, et al., Nucl. Fusion **42**, 750 (2002).
[7] T. Morisaki, et al., Contrib. Plasma Phys. **40,** 266 (2000).
[8] E. H. Wang, et al., Plasma Fusion Res. **8**, 2402176 (2013).
[9] E. H. Wang, et al., Rev. Sci. Instrum. **83**, 043503 (2012).
[10] S. Morita, et al., Plasma Phys. Control. Fusion **56**, 094007 (2014).
[11] E. H. Wang, et al., Rev. Sci. Instrum. **83**, 10E509 (2012).
[12] E. H. Wang, et al., Plasma Sci. Technol. **15**, 106 (2013).
[13] Y. Takeiri, Rev. Sci. Instrum. **81**, 02B114 (2010).

[14] Y. Takeiri, et al., Fusion Sci. Technol. **58**, 482 (2010).
[15] O. Kaneko, et al., Nucl. Fusion **43,** 692 (2003).
[16] M. B. Chowdhuri, et al., Rev. Sci. Instrum. **78**, 023501 (2007) [Erratum: **84,** 109901 (2013).
[17] M. B. Chowdhuri, et al., Appl. Opt. **47**, 135 (2008).
[18] C. F. Dong, et al., Rev. Sci. Instrum. **81**,033107 (2010).
[19] C. F. Dong, et al., Rev. Sci. Instrum. **82**, 113102 (2011).
[20] H. Y. Zhou, et al., Rev. Sci. Instrum. **79**, 10F536 (2008).
[21] Y. Nakamura, et al., J. Phys. Soc. Jpn. **58**, 3157 (1989).
[22] K. Yamazaki , et al., J. Plasma Fusion Res. **79,** 739 (2003).
[23] K. Narihara, et al., Rev. Sci. Instrum.**72**, 1122 (2001).
[24] P. J. Storey, et al., Phys. Commun. **66**, 129 (1991).
[25] H. Suzuki, et al., J. Nucl. Mater. **313**–**316** 297 (2003).
[26] C. F. Dong, et al., Jpn. J. Appl. Phys. **51**, 010205 (2012).
[27] C. F. Dong, et al., Plasma Sci. Technol. **15**, 230 (2013).
[28] C. F. Dong, et al., Rev. Sci. Instrum. **83**, 10D509 (2012).
[29] X. L. Huang, et al., Rev. Sci. Instrum. **85**, 043511 (2014).
[30] S. K. Allison, et al., Phys. Rev. **127**, 792 (1962).
[31] H. Ogawa, et al., Phys. Rev. A **54**, 5027 (1996).

Chapter 3

Poloidal distribution of impurity emissions

3.1 Introduction

In the Large Helical Device (LHD), the core plasma is surrounded by the ergodic layer, in which magnetic fields with three-dimensional (3-D) structures are formed by higher-order components of the magnetic fields created by a pair of helical coils and by overlapping of edge small islands [1-4]. A two-dimensional (2-D) space-resolved extreme ultraviolet (EUV) spectrometer has been developed to measure the 2-D distribution of impurity line emissions in the ergodic layer [5,6]. The 2-D distributions of edge impurity emissions have been measured for various impurity species, e.g., CIV, HeII and FeXVI [5-7]. An entirely non-uniform 2-D distribution has been observed for such edge impurity emissions. These impurity emissions are enhanced at the top and bottom plasma boundaries and in the vicinity of the X-points. Such measured 2-D distributions may reflect a non-uniform poloidal distribution of the edge impurity emissions. Therefore, evaluating the poloidal distribution of edge impurity emissions is important for deeper understanding of the impurity behavior at the plasma edge, in particular, in the ergodic layer. As the LHD plasma shape poloidally rotates five times during one toroidal turn, the poloidal distribution of the edge impurity emissions can be estimated from their 2-D distributions. In practice, the poloidal distribution of impurity emissivities is obtained by analyzing each vertical profile measured at different toroidal positions. In this study, the poloidal impurity distribution is presented for CIV, CVI, FeXV and FeXVIII with different ionization energies. The result is compared with simulation result of the EMC3-EIRENE code [8-10].

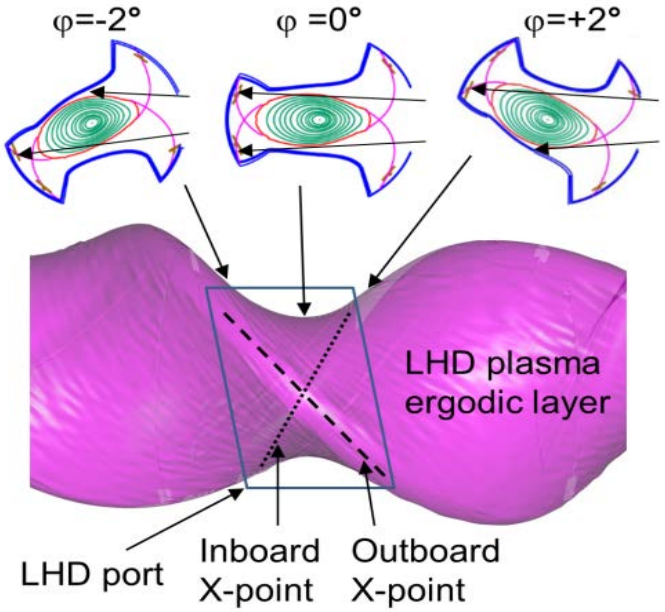

Fig. 3.1 Horizontal view of LHD ergodic layer and poloidal plasma cross-sections at three different toroidal angles $\varphi = -2°$, 0° and +2°.

3.2 EUV spectrometer and 2-D impurity emission distribution measurement

A 2-D space-resolved EUV spectrometer has been developed to measure the 2-D distribution of impurity emissions in the wavelength range of 60 to 400 Å by horizontally scanning the optical axis of the spectrometer [5]. Figure 3.1 shows the horizontal view of the LHD plasma with the ergodic layer. The position of the LHD port is shown by a diamond solid line. The observation area for the 2-D distribution measurement is limited to 120 cm and 90 cm in the vertical and horizontal directions, respectively. The inboard and outboard X-point trajectories are represented by the dotted and dashed lines, respectively. The spatial resolutions of the space-resolved EUV spectrometer (at a horizontal scanning speed $V_{EUV} = 0$) in the LHD vacuum vessel (at the major radius R = 3.60 m) are 65.3 mm and 30.2 mm in horizontal and vertical directions, respectively. The horizontal spatial resolution degrades a little when the horizontal scanning speed increases, e.g., 80 mm at $V_{EUV} = 2.5$ mm/s [5].

The main impurity species in the LHD discharges is carbon which originates from the divertor plates made of graphite. The carbon density relative to the electron density (n_{carbon}/n_e) roughly ranges in $1\% \leq n_{carbon}/n_e \leq 3\%$. The iron impurity originates

from the first wall made of stainless steel, and its density relative to the electron density, n_{Fe}/n_e, is usually very small, i.e., $n_{Fe}/n_e < 0.01\%$. As the magnetic field connection length in the ergodic layer of the LHD is longer compared with the case of tokamaks, friction force is dominant rather than the ion temperature gradient (ITG) force. Thus, the iron ion sputtered on the first wall tends to move toward the divertor plates. Therefore, in the LHD, the edge impurity transport does not depend on the impurity source location.

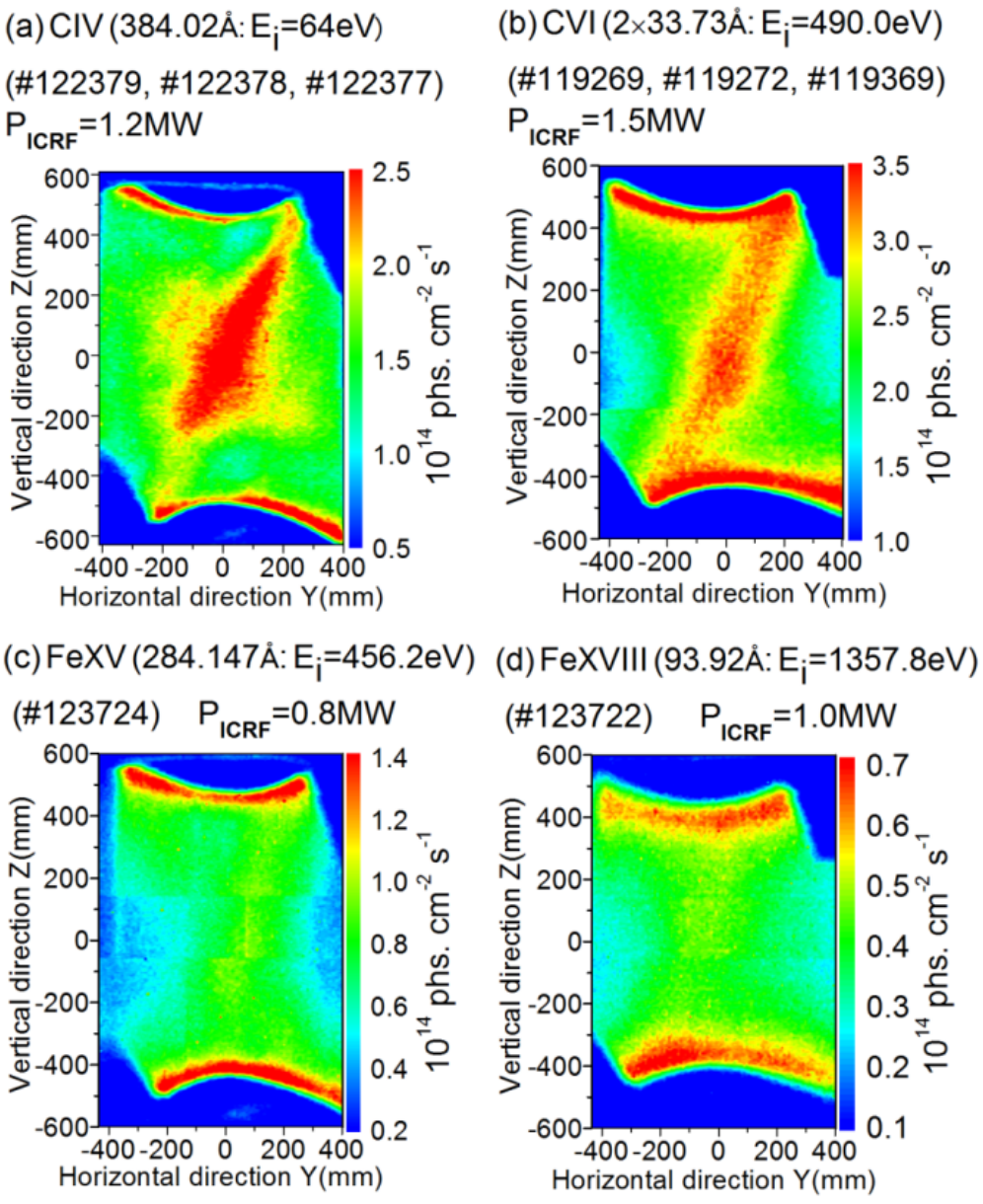

Fig. 3.2 2-D distributions of (a) CIV, (b) CVI, (c) FeXV and (d) FeXVIII at R_{ax} = 3.60 m. The shot numbers and ICRF power are indicated in each distribution.

Figure 3.2 shows the 2-D distributions of the CIV (384.174 Å, 64.0 eV), CVI (2 × 33.73 Å, 490.0 eV), FeXV (284.164 Å, 456.2 eV) and FeXVIII (93.92 Å, 1357.8 eV) impurity emissions at the specified wavelengths and ionization energies. All of the 2-D distributions are measured during the flat-top phase of the ion cyclotron resonance frequency (ICRF) discharges at the magnetic-axis position of R_{ax} = 3.60 m for similar plasma parameters, i.e., line-averaged electron density $n_e \approx 1\times10^{13}$ cm^{-3}. No remarkable variation in any of the parameters is observed during the horizontal scanning. The intensities of the impurity line emissions are absolutely calibrated using radial profiles of the bremsstrahlung continuum in the EUV and visible ranges [11,12]. In the measured 2-D distributions, the spectral intensities near the top and bottom plasma boundaries are seen to be enhanced because of a long chord length passing through the edge plasma. The inboard X-point trajectory (see Fig. 3.1) is also enhanced for CIV and CVI, indicating a non-uniform poloidal distribution in the ergodic layer.

3.3 Analysis of poloidal distribution

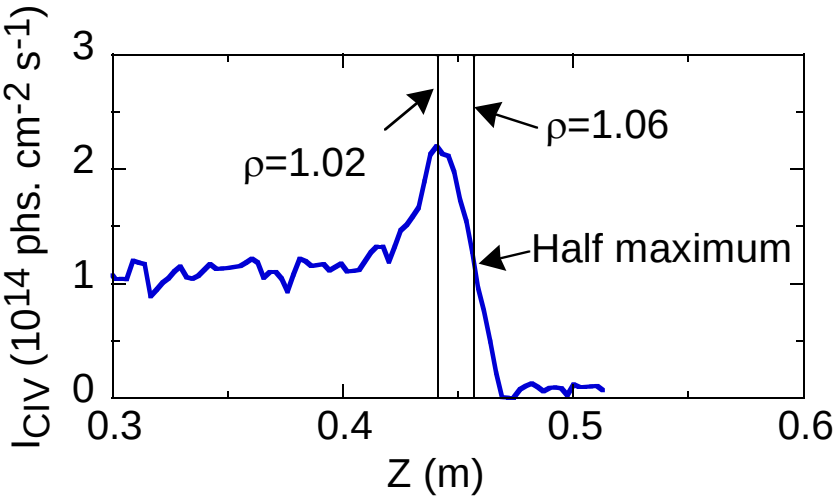

Fig. 3.3 CIV vertical profile at Y = 0 as a function of vertical position (also see Fig. 3.2).

The elliptical cross sections of the LHD plasma at three different toroidal positions, i.e., φ = −2°, 0° and +2°, are shown in Fig. 3.1. The observation chords passing through the top and bottom plasma boundaries are also shown by two solid arrows in each poloidal cross section. In the figure, it is clear that the emission intensity

at the top and bottom edges measured at different toroidal positions can show information on the poloidal distribution of impurity emissions. Thus, an evaluation of the poloidal distribution of the edge impurity emissions is attempted by analyzing the impurity emission at the top and bottom edges of the 2-D distributions. In the analysis, the data from the X-points with extremely non-uniform emissions are not used.

As the first step, the magnetic flux surface of LHD is calculated with a 3-D equilibrium code (VMEC) as a function of pressure profile. Although no magnetic surface exists in the ergodic layer, virtual magnetic surfaces, which are calculated by extrapolating the magnetic flux surface at last closed flux surface (LCFS), are assumed at $\rho > 1$. This assumption is usually used when the edge plasma in the ergodic layer is analyzed in the LHD.

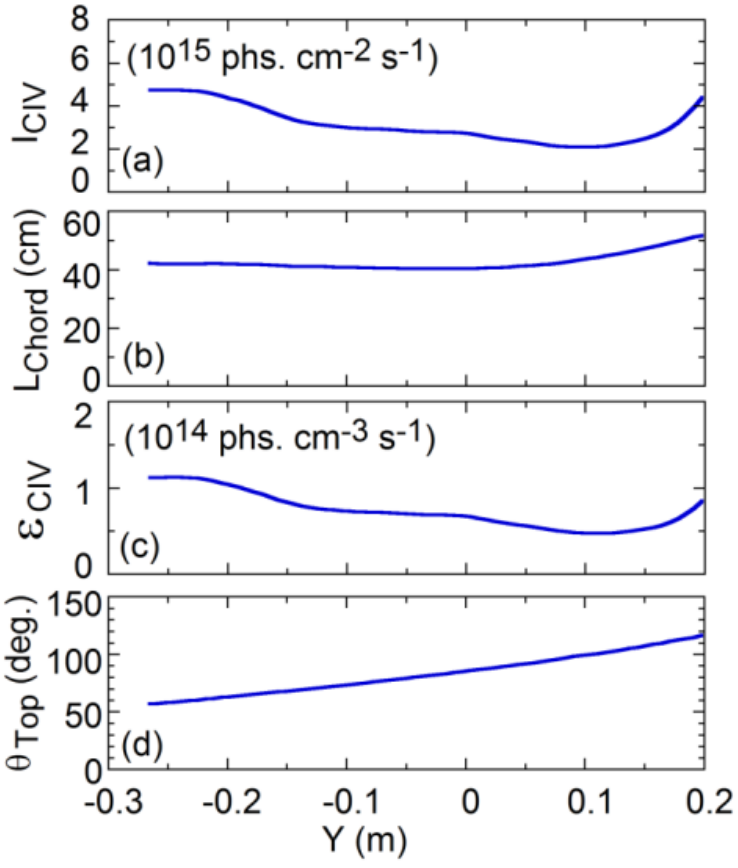

Fig. 3.4 (a) Chord-integrated intensity of CIV, (b) observation chord length, (c) CIV emissivity and (d) poloidal angle at the top plasma edge as a function of horizontal position Y.

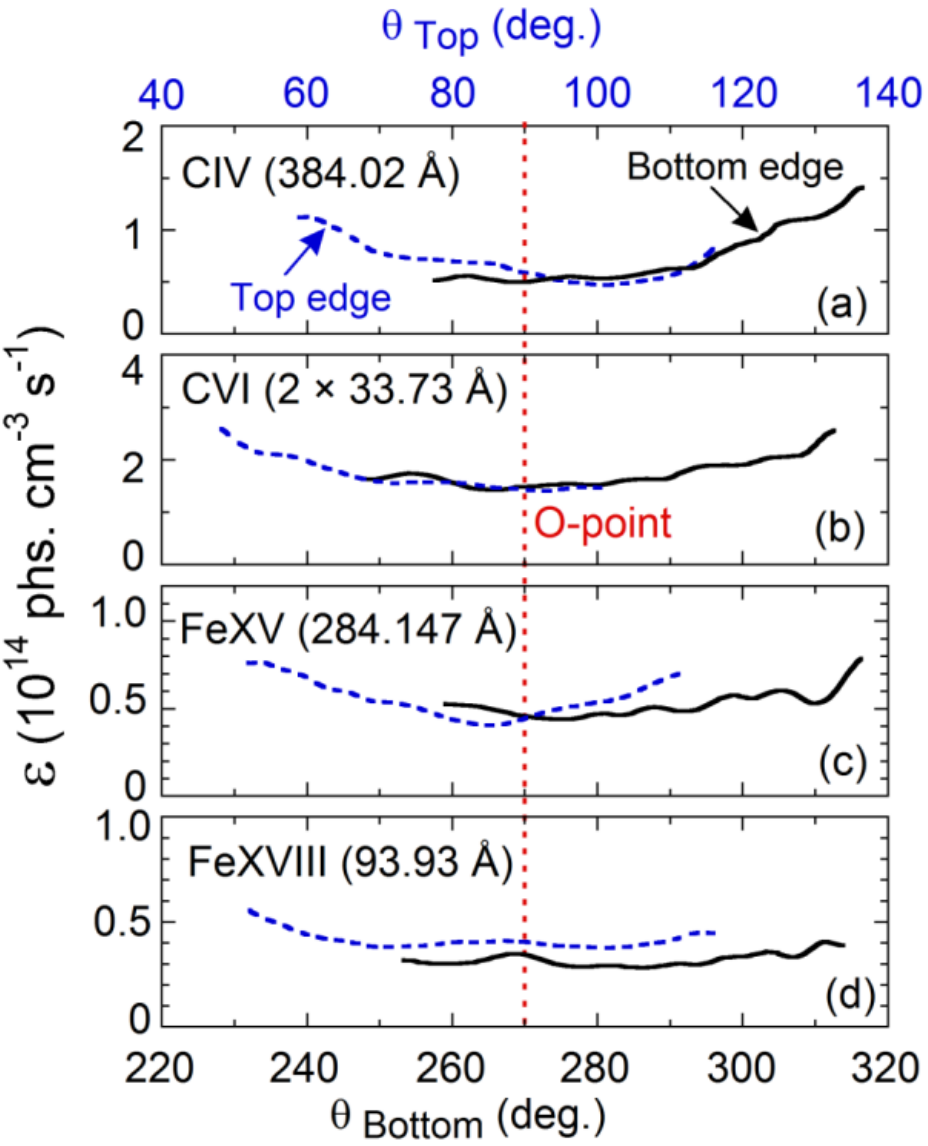

Fig. 3.5 Poloidal distributions of (a) CIV, (b) CVI, (c) FeXV and (d) FeXVIII as a function of poloidal angles θ_{Top} and θ_{Bottom}.

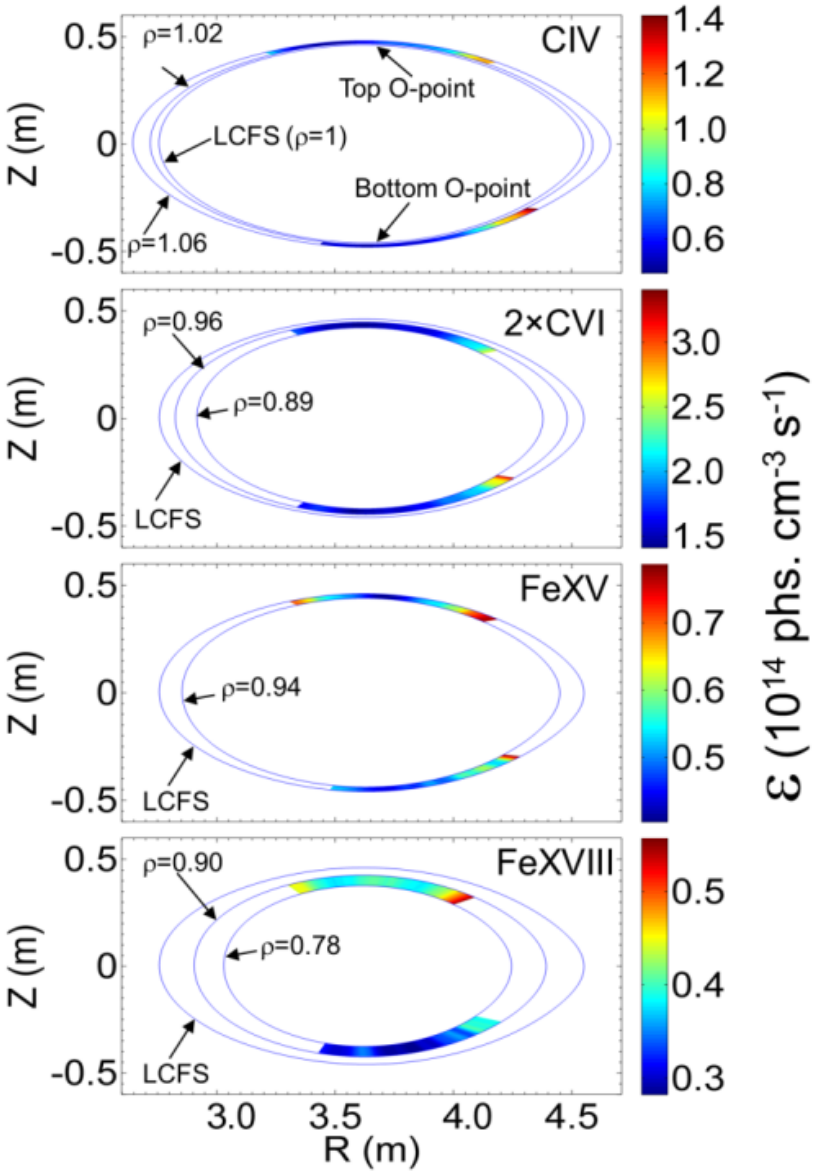

Fig. 3.6 Poloidal distributions of (a) CIV, (b) CVI, (c) FeXV and (d) FeXVIII at horizontally elongated plasma cross-sections. The measure of the emissivity is represented by different colors.

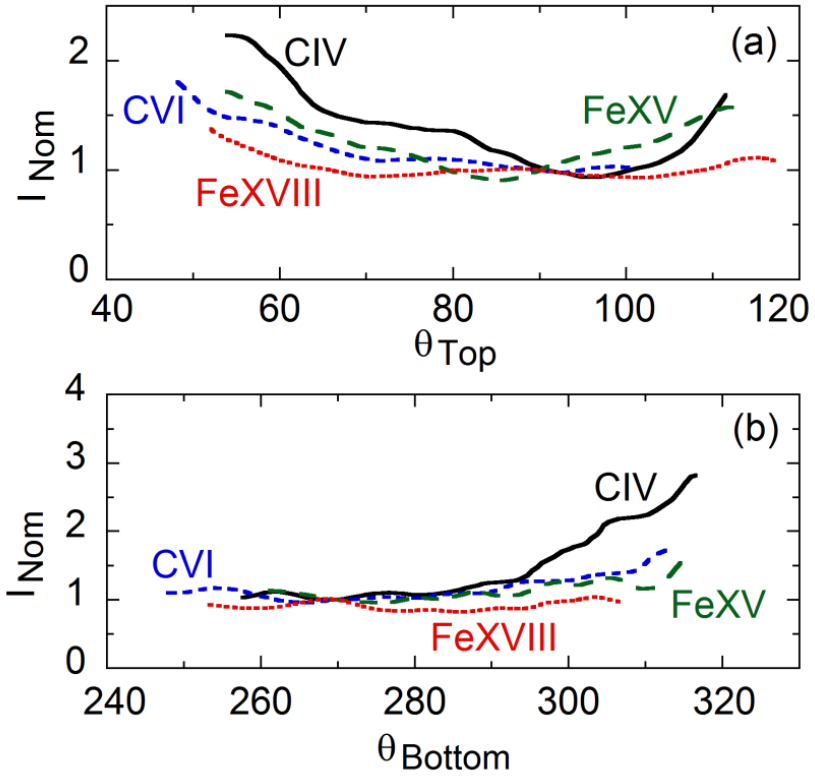

Fig. 3.7 Emissivity profiles of CIV, CVI, FeXV and FeXVIII at (a) top and (b) bottom regions normalized to the emissivity at θ_{Top} = 90° and θ_{Bottom} = 270°, respectively.

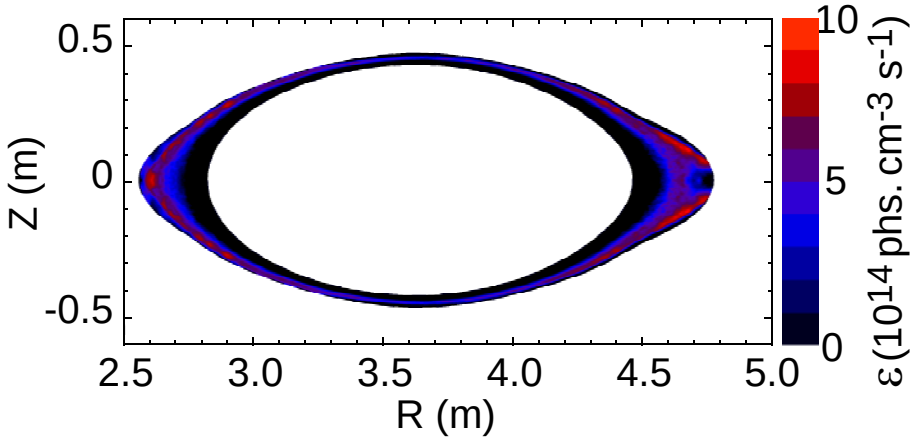

Fig. 3.8 Simulation of emissivity distribution of CIV (312.4 Å) using EMC3-EIRINE code under similar conditions as the experiment.

An example of the vertical profile of impurity emissions at the top edge is shown in Fig. 3.3 for CIV measured at Y = 0, which means $\varphi = 0°$ (see Fig. 3.2). A sharp peak is observed near the plasma edge boundary. Here, the inner and outer boundaries of the impurity vertical profile are defined by intensities at the peak and the half maximum, respectively. In the figure, the inner and outer boundaries of the CIV radial profiles are estimated to be $\rho = 1.02$ and $\rho = 1.06$, respectively.

After analyzing the inner and outer boundaries of impurity emissions, the chord-integrated intensity is estimated by integrating the emission between the two boundaries. Figure 3.4 (a) shows the chord-integrated intensity of CIV emissions at the top plasma edge, which is calculated as a function of the horizontal position. The observation chord length calculated at each toroidal position is shown in Fig. 3.4 (b). The local emissivity of CIV in each case is then obtained by dividing the chord-integrated intensity by the chord length. The results are plotted as shown in Fig. 3.4 (c).

The poloidal angle at the top plasma edge is calculated from the assumed magnetic flux surface in the ergodic layer for each horizontal position, as shown in Fig. 3.4 (d). Thus, the poloidal distribution of the CIV emissivity near the top edge can be reconstructed using vertical and horizontal coordinates from the 2-D CIV distribution. The poloidal distribution of the CIV emissivity near the bottom edge can also be analyzed in the same manner.

3.4 Results and discussion

The poloidal emissivity distributions evaluated from the 2-D distributions in Figs. 3.2 (a)–(d) are shown in Figs. 3.5 (a)–(d) as a function of the poloidal angles θ_{Top} and θ_{Bottom} at the top and bottom edges, respectively. Here, the poloidal angle is defined as the angle toward the counter-clockwise direction, with the reference as the point along the axis of the elliptical plasma on the outboard side. The poloidal distributions measured at the top and bottom edges are plotted as the dashed and solid lines, respectively. Due to the limited observation range of the EUV spectrometer, the distributions are obtained in the ranges $55° \leq \theta_{Top} \leq 110°$ and $255° \leq \theta_{Bottom} \leq 320°$. The poloidal distributions of these impurity species are also plotted against the horizontally elongated plasma cross sections. The results shown in Fig. 3.6 indicate that the radial location of the impurity ions changes inwardly (toward the plasma center) as the ionization energy increases. From the Figs. 3.5 and 3.6, it is clear that the poloidal distribution is non-uniform for impurity ions existing in the ergodic layer and in the vicinity of the LCFS, and that the non-uniformity becomes stronger with a reduction in the ionization energy of the impurity ions. This means that impurity ions located at the

outer region of the ergodic layer exhibit larger non-uniformity in the poloidal distribution. In addition, the emissivity becomes stronger as the impurity location gets closer to the X-point, whereas it is weak at both the top and the bottom O-points defined by the poloidal positions of the elliptical plasma boundary adjacent to the helical coils.

In order to compare in detail the non-uniformity among the four impurity species, the emissivity distributions from the top and bottom regions are normalized to the emissivity at the top (θ_{Bottom} = 90°) and bottom (θ_{Bottom} = 270°) O-points, respectively. The results for the top and bottom regions are shown in Figs. 3.7 (a) and (b), respectively. The normalized poloidal distribution becomes gradually uniform as the impurity ions radially move toward the plasma center. The poloidal profile of CIV shows an extremely non-uniform distribution. As the C^{3+} ions with low ionization energy (E_i = 64 eV) are located near the edge boundary of the ergodic layer, they are strongly affected by a specific edge impurity transport, which is dominant in the ergodic layer with a 3-D magnetic field structure. On the contrary, the poloidal profile of FeXVIII located within $0.78 \leq \rho \leq 0.90$ indicates a relatively flat distribution. This means the FeXVIII emissivity is a function of the magnetic surface.

The carbon distribution in the ergodic layer has been also analyzed using the 3-D edge plasma transport code, EMC3-EIRINE [8-10,13]. The emissivity distribution of CIV (312.4 Å) simulated with the code is plotted in Fig. 3.8. The plotted results indicate that the CIV emission located in the ergodic layer is stronger when the radial location moves outside. The simulated result entirely supports our present result, despite the estimation of the poloidal distribution is obtained from the 2-D distribution. Therefore, the present analysis can provide a reliable method to evaluate the impurity poloidal distribution.

3.5 Summary

The poloidal emissivity distributions of CIV, CVI, FeXV and FeXVIII have been reconstructed from their 2-D distributions measured with the space-resolved EUV spectrometer in the LHD. A non-uniform poloidal distribution has been clearly observed for CIV, whereas the FeXVIII distribution is basically a function of the magnetic surface. The present CIV results are well supported by a 3-D simulation.

References

[1] N. Ohyabu, et al., Nucl. Fusion **34**, 387 (1994).
[2] T. Morisaki, et al., J. Nucl. Mater. **31**, 3548 (2003).
[3] S. Morita, et al., Nucl. Fusion **53**, 093017 (2013).
[4] M. B. Chowdhuri, et al., Phys. Plasmas **16**, 062502 (2009).

[5] E. H. Wang, et al., Rev. Sci. Instrum. **83**, 043503 (2012).
[6] H. M. Zhang, et al., Jpn. J. Appl. Phys. **54**, 086101 (2015)
[7] S. Morita, et al., Plasma Phys. Control. Fusion **56**, 094007 (2014).
[8] Y. Feng, et al., Contrib. Plasma Phys. **44**, 57 (2004).
[9] D. Reiter, et al., Fusion Sci. Technol. **47**, 172 (2005).
[10] S. Y. Dai, et. al., Nucl. Fusion **56**, 066005 (2016).
[11] C. F. Dong, et al., Rev. Sci. Instrum. **83**, 10D509 (2012).
[12] X. L. Huang, et. al., Rev. Sci. Instrum. **85**, 043511 (2014).
[13] M. Kobayashi, et al., Nucl. Fusion **53**, 033011 (2013).

Chapter 4

Partial carbon radiation at each ionization stage of C^{2+} to C^{5+} ions

4.1 Introduction

Steady operation of the detached plasma has been achieved without additional impurity gas puffing in LHD by forming m/n = 1/1 magnetic island at $\iota/2\pi = 1$ in the ergodic layer with RMP coils [1–3]. Carbon released from graphite divertor plates is a dominant intrinsic impurity in high-density LHD discharges [4]. Then, it seems that the carbon radiation during the plasma detachment is also important for the effective edge plasma cooling triggering the detachment. In LHD, C^{2+} and C^{3+} ions with low ionization energies (E_i = 48, 65 eV) are located near the outer boundary in the ergodic layer, whereas C^{4+} and C^{5+} ions with relatively high ionization energies (E_i = 392, 490 eV) are located near the last closed flux surface (LCFS) [4]. In the RMP-assisted plasma detachment, therefore, it is very interesting to compare the radiation power from C^{2+} and C^{3+} ions located outside $\iota/2\pi = 1$ with that from C^{4+} and C^{5+} ions located inside $\iota/2\pi = 1$.

The partial radiation power at each ionization stage in carbon ions of C^{2+} to C^{5+}, $P_{rad}(C^{q+})$, is analyzed from line intensities of CIII–CVI resonance transitions which can be measured with extreme ultraviolet (EUV: 10–500 Å) and vacuum ultraviolet (VUV: 300–2400 Å) spectrometers. Intensity ratios of the $P_{rad}(C^{q+})$ to the resonance line can be useful to estimate the P_{rad} (C^{q+}). For the purpose the electron temperature at the radial location where the carbon ion exists has to be evaluated because the intensity ratio is sensitive to the electron temperature. In addition, the spectral intensity has to be

absolutely calibrated, in particular, for the VUV spectrometer. Thus, the P_{rad} (C^{q+}) analyzed with the intensity ratio are compared between attached and detached plasmas.

4.2 Experimental setup

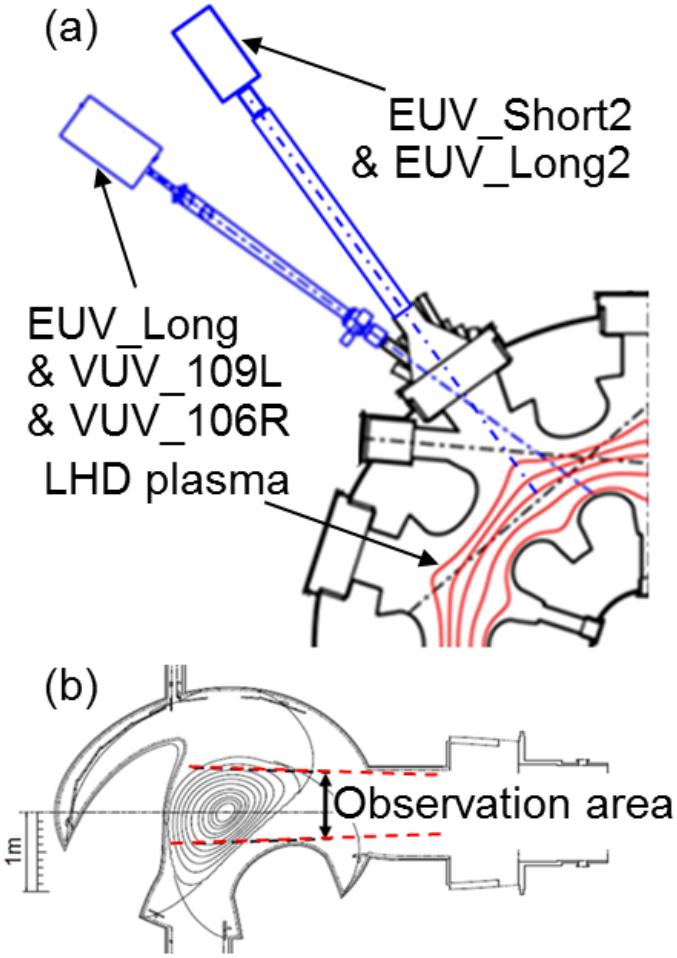

Fig. 4.1 (a) Schematic view of space-resolved EUV and VUV spectrometers (EUV_Short2 and EUV_Long2) and high-time-resolution EUV and VUV spectrometers (EUV_Long, VUV_109L and VUV_106R) and (b) observation area of EUV_Long, VUV_109L and VUV_106R.

In LHD, the m/n = 1/1 magnetic island formed by the RMP coil system was originally used for the local island divertor experiment to realize an efficient particle exhaust. The O-point of the m/n = 1/1 magnetic island is then positioned in the

outboard side of horizontally elongated plasma cross section at #6-O or #7-O toroidal section. In the present study it is called 6-O or 7-O island configuration. Since the detached plasma is realized at the magnetic axis position of R_{ax} = 3.90 m, the m/n = 1/1 island is located in the ergodic layer due to the low edge rotational transform.

The EUV and VUV spectrometers are installed on #10-O diagnostic port of LHD, as shown in Fig. 4.1 (a). In the present study, two EUV spectrometers named EUV_Short (10–100Å) and EUV_Long (50–650Å) and two 20 cm normal incidence VUV spectrometers named VUV_109L (300–1000Å) and VUV_106R (970–1900Å) are used for simultaneous high-time resolution measurement (5ms) of carbon resonance lines, i.e., CIII (977.02Å, $2s2p–2s^2$), CIV (1548.2Å, 2p–2s), CV (40.27Å, $1s2p–1s^2$) and CVI (33.73Å, 2p–1s) [5,6]. Two space-resolved EUV spectrometers named EUV_Short2 and EUV_Long2 are used for simultaneous vertical profile measurement of CIII (386.2 Å), CIV (384.17 Å), CV (40.27 Å) and CVI (33.73 Å) in the range of $-0.6 \leq Z \leq 0.6$ m with a time resolution of 100 ms [7–9]. The EUV_Long, VUV_109L and VUV_106R have a similar observation range, as shown in Fig. 4.1 (b).

4.3 Calibration of VUV spectrometers

In order to obtain the absolute intensity of CIII and CIV resonance lines, the spectral intensity measured by VUV_109L and VUV_106R has to be calibrated into the absolute intensity. The wavelength ranges of EUV_Long and VUV_109L are overlapped between 300 and 650 Å. Since the spectral intensity of EUV_Long has been already calibrated on the basis of the bremsstrahlung profile measurement in previous studies [5,10], the spectral intensity of VUV_109L can be easily calibrated by directly comparing the same spectrum from both spectrometers in the same wavelength range of 400 – 650Å. The result is plotted in Fig. 4.2 with open circles.

In order to calibrate the intensity of VUV spectra in longer wavelength range, e.g., 650–1600 Å, the intensity ratio method is applied. As shown in Fig. 4.3, two intensity ratios of CIII (977.02 Å/386.2 Å, 2p–2s/3p–2s) and CIV (1548.2 Å/312.4 Å, 2p–2s/3p–2s) are calculated with ADAS atomic code as a function of electron temperature [11]. The contribution of n_e to the ratio can be neglected because the ratio is practically insensitive to n_e. Here, the absolute intensity of CIII (386.2 Å) and CIV (312.4 Å) is obtained with EUV_Long spectrometer.

The electron temperature at radial location where the C^{2+}–C^{5+} ions exist is determined by analyzing the vertical profile of CIII–CVI emissions, as shown in Fig. 4.4. The vertical profile of CIII (386.2 Å), CIV (384.02 Å), CV (40.27 Å) and CVI (33.73 Å) is simultaneously observed with EUV_Long2 and EUV_Short2. The result is plotted in Fig. 4.4 (a). A sharp peak appears in the vertical profile at $0.4 < Z < 0.5$ m

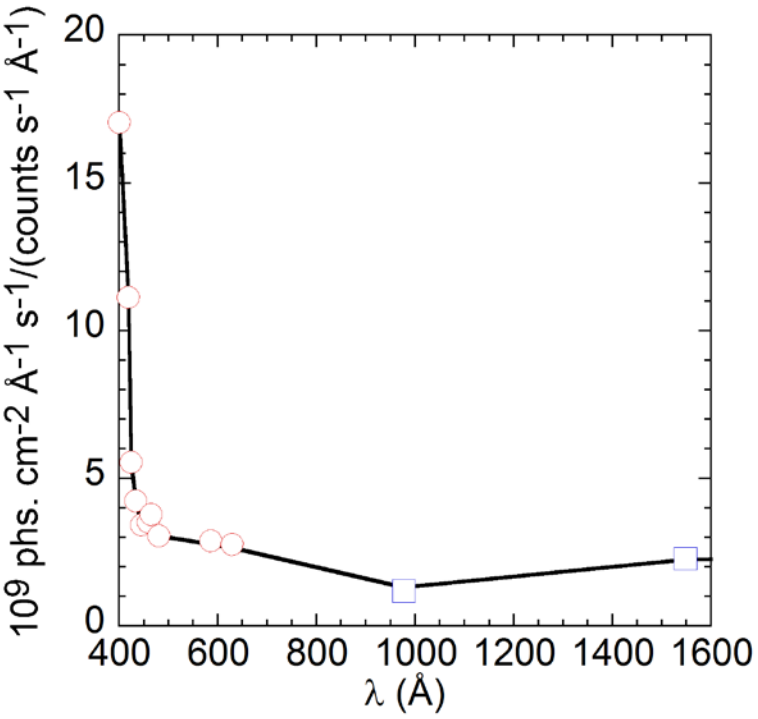

Fig. 4.2 Absolute intensity calibration factor of VUV_109L and VUV_106R in the wavelength range of 400–1600 Å.

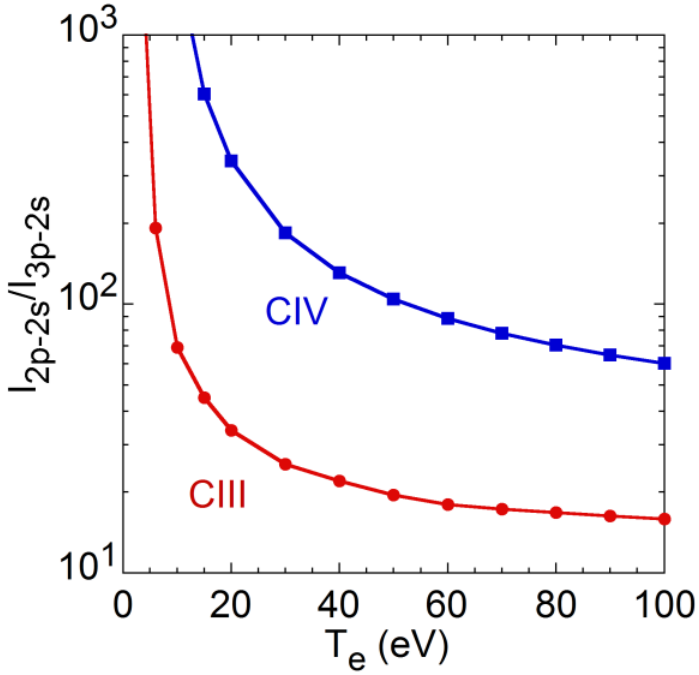

Fig. 4.3 Intensity ratios of CIII (977.02 Å/386.2 Å) and CIV (1548.2 Å/312.4 Å).

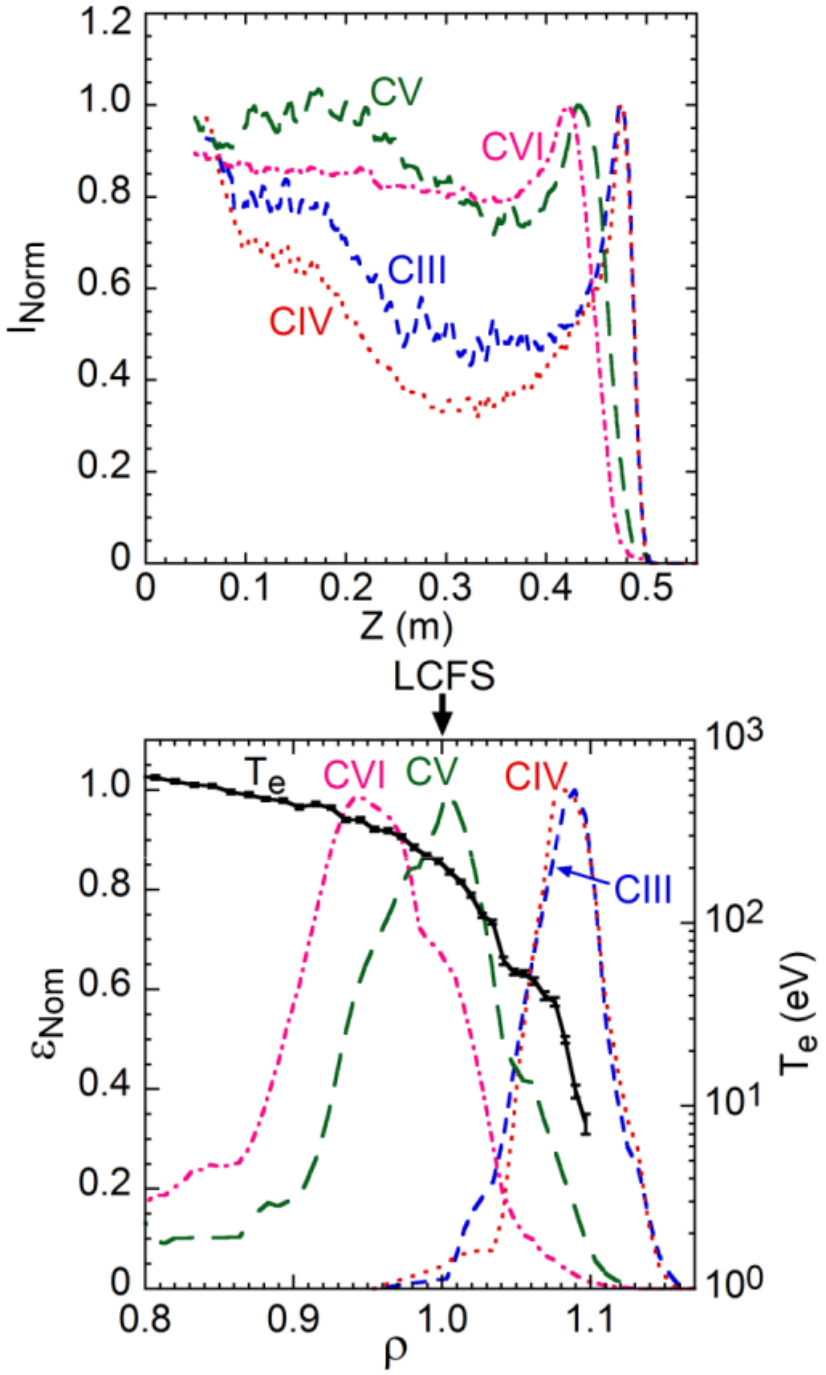

Fig. 4.4 (a) Normalized chord-integrated vertical profiles of CIII (386.2 Å), CIV (384.02 Å), CV (40.27 Å) and CVI (33.73 Å) and (b) Normalized local emissivity profiles of CIII to CVI and T_e profile as a function of minor radius.

because the chord length passing through the edge plasma is long at the top edge in horizontally elongated plasma cross section. The intensity in CIII–CVI profiles is normalized at each edge peak. Local emissivity profiles of CIII–CVI are obtained by reconstructing the chord-integrated profiles measured along the vertical direction based on the Abel inversion method. The magnetic surface necessary for the Abel inversion is calculated with the Variational Moments Equilibrium Code (VMEC), including the effect of finite plasma pressure. Although no magnetic surface exists in the ergodic layer, virtual magnetic surfaces are assumed at $\rho > 1$ by extrapolating the magnetic flux surface at $\rho = 1$. This assumption is generally used in LHD when the analysis is carried out for the ergodic layer [8]. The result is plotted in Fig. 4.4 (b). The emissivity profile is also normalized at each peak value. In the same figure a T_e profile measured by Thomson scattering system is also plotted. Then, the electron temperature at radial locations of C^{2+}–C^{5+} ions is determined from the peak position in the CIII–CIV emissivity profile, i.e., 15 eV for C^{2+}, 20 eV for C^{3+}, 210 eV for C^{4+} and 360 eV for C^{5+}.

The intensity ratio in Fig. 4.3 is determined with electron temperatures mentioned above. Thus, the spectral intensity from VUV_109L and VUV_106R spectrometers can be absolutely calibrated at wavelengths of 977.02 Å and 1548.2 Å based on the absolute intensity of CIII (386.2 Å) and CIV (312.4 Å) and the intensity ratio. The result obtained from the intensity ratio method is shown in Fig. 4.2 with open squares. Finally, the analyzed calibration factor is fitted with a smooth curve in the wavelength range of 400 – 1600 Å, as shown in Fig. 4.2 with solid line.

4.4 Estimation of partial radiation P_{rad} (C^{q+})

Radiation power of the resonance transition generally occupies a considerably large part in the radiation power from impurity ions in a certain ionization stage. Since the absolute intensity of resonance line of CIII (977.02 Å), CIV (1548.2 Å), CV (40.27 Å) and CVI (33.73 Å) is measured with the EUV and VUV spectrometers, the ratio of P_{rad} (C^{q+}) to resonance line intensity in C^{q+} ions can be calculated with ADAS atomic code. The ratio of P_{rad} (C^{q+}) to resonance line intensity is shown in Figs. 4.5 (a) – (d) as a function of electron temperature with parameter of electron density. Since the ratio is practically insensitive to n_e as seen in the figure, the contribution of n_e can be neglected in the present analysis. As the value of T_e for each ionization stage of carbon ions is already determined from the profile analysis done in Fig. 4.4 (b), the P_{rad} (C^{q+}) can be evaluated from the intensity ratio in Fig. 4.5.

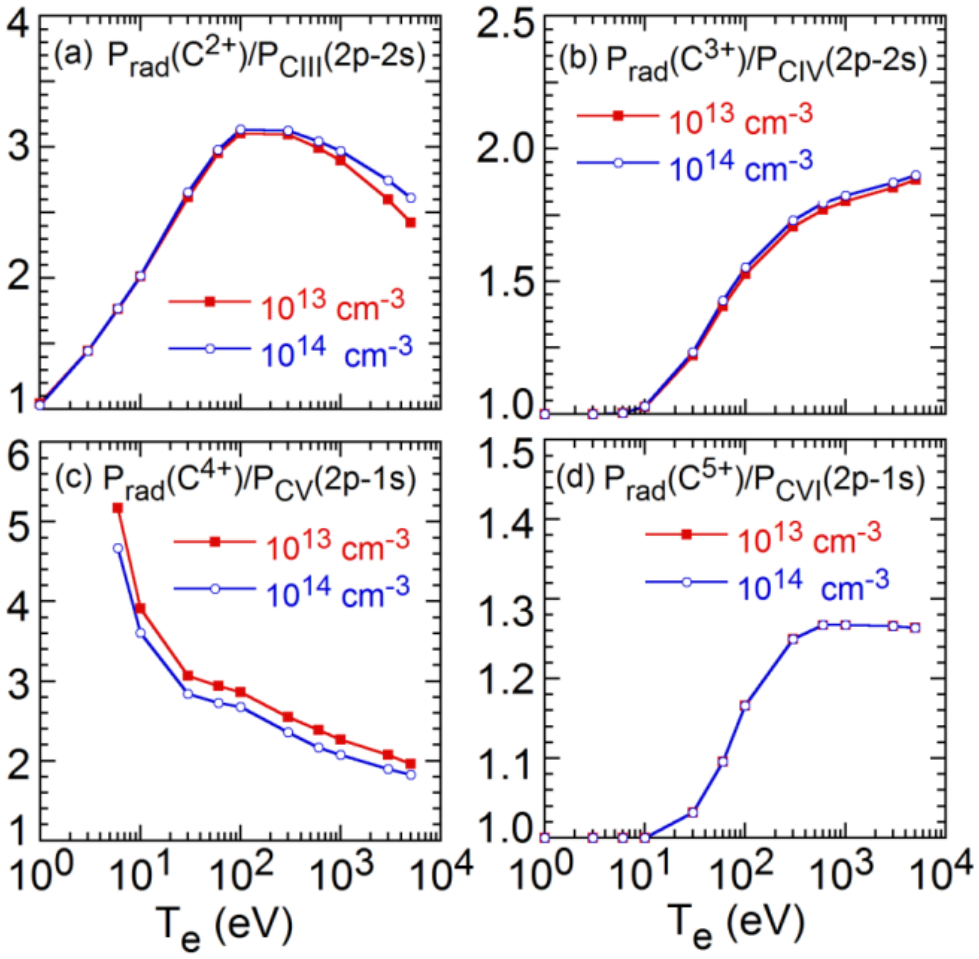

Fig. 4.5 Ratios of partial carbon radiation power at each ionization stage to radiation power of resonance line: (a) P_{rad} (C^{2+})/P_{CIII} (2p–2s), (b) P_{rad} (C^{3+})/P_{CIV} (2p–2s), (c) P_{rad} (C^{4+})/P_{CV} (2p–1s) and (d) P_{rad} (C^{5+})/P_{CVI} (2p–1s).

4.5 P_{rad} (C^{q+}) in attached and detached plasmas

The partial carbon radiation of P_{rad} (C^{2+}) to P_{rad} (C^{5+}) is analyzed for attached and detached plasmas. Figure 4.6 shows a comparison of discharge waveform between attached [Figs. 4.6 (a)–(f)] and detached [Figs. 4.6 (g)–(l)] plasmas. These two discharges are operated at magnetic axis position of R_{ax} = 3.90 m and heated by negative-ion-source based NBIs. The total radiation loss, P_{rad}, shows similar values for both plasmas, i.e., 20–25% to the port-through NBI power, P_{NBI}. In the attached plasma the line-averaged electron density is maintained constantly (~ 5×10^{13} cm^{-3}) during t = 4–

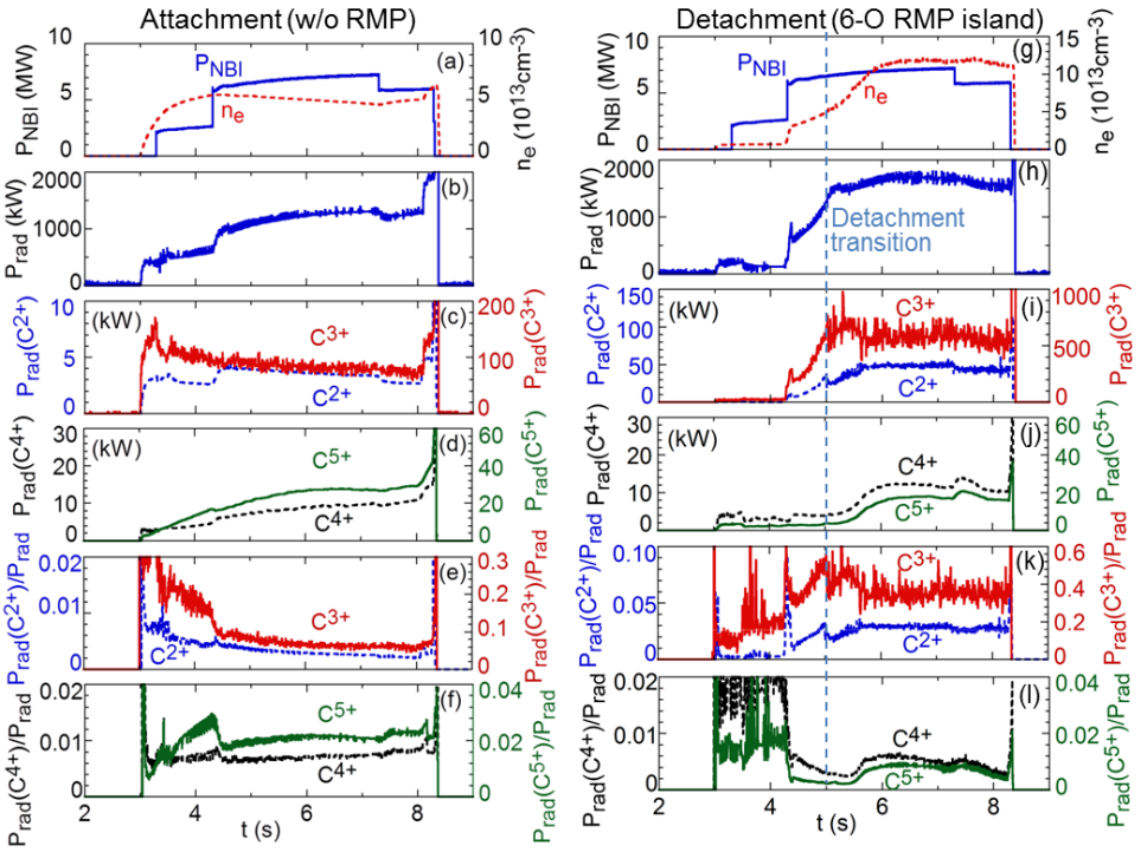

Fig. 4.6 Time behaviors of (a) NBI port-through power and line-averaged electron density, (b) total radiation loss (P_{rad}), partial carbon radiation power of (c) P_{rad} (C^{2+}) and P_{rad} (C^{3+}) and (d) P_{rad} (C^{4+}) and P_{rad} (C^{5+}) and ratios of P_{rad} (C^{q+}) to P_{rad} of (e) P_{rad} (C^{2+})/P_{rad} and P_{rad} (C^{3+})/P_{rad} and (f) P_{rad} (C^{4+})/P_{rad} and P_{rad} (C^{5+})/P_{rad} in the attached plasma without RMP. Graphs of (g) - (l) indicate time behaviors from detached plasma with 6-O RMP island in the same meaning as graphs (a) - (f).

8 s with P_{rad} = 1400 kW. The contribution of P_{rad} (C^{2+}) and P_{rad} (C^{4+}) to P_{rad} is less than 1%, while P_{rad} (C^{3+})/P_{rad} and P_{rad} (C^{5+})/P_{rad} are 8% and 2%, respectively.

In the discharge with detached plasma, the m/n = 1/1 island is formed in the ergodic layer and the O-point of the island is located at the outboard side of #6 toroidal section. With increase in the electron density, the plasma detachment occurs at t = 5.0 s, as shown in Figs. 4.6 (g)–(l). The electron density starts to increase after the appearance of the detachment at t = 5.0 s, but it is saturated at t = 6.0 s. The plasma detachment is steadily maintained at high density of $n_e = 12\times10^{13}$ cm^{-3} during t = 6–8 s until the end of NBI pulse. The radiation loss also reaches the maximum value of P_{rad} =

1700 kW. Compared with the attached plasma, it is found that the P_{rad} (C^{2+})/P_{rad} and P_{rad} (C^{3+})/P_{rad} significantly increase to 3% and 40% during the detachment phase, respectively, whereas the increment of P_{rad} is only 300 kW. In contrast, the P_{rad} (C^{4+})/P_{rad} and P_{rad} (C^{5+})/P_{rad} do not change so much compared to the attached plasma.

The drastic increase in P_{rad} (C^{2+}) and P_{rad} (C^{3+}) during the detachment phase is very clear from the present analysis. The P_{rad} (C^{3+}) expresses a dominant portion in the total carbon radiation in the detached plasma. A flattening of T_e profile appears during the detachment phase in edge T_e of 10 ~ 20 eV at the radial location of m/n = 1/1 magnetic island [1]. Radial locations of C^{2+} and C^{3+} ions are also broadened reflecting the T_e flattening as shown in Fig. 4.4 (b). The expansion of the radial location significantly enhances the P_{rad} (C^{2+}) and P_{rad} (C^{3+}) in the detached plasma. Therefore, it is concluded that a change in the edge transport of C^{2+} and C^{3+} ions locating near m/n = 1/1 island brought by the RMP field play an important role for the present detachment achievement. In addition, the carbon transport near LCFS is not affected by the supplied RMP field because the P_{rad} (C^{4+}) and P_{rad} (C^{5+}) do not change at all in both discharges with attachment and detachment.

Before the transition to the detached plasma the divertor heat flux increases with density, but the edge radiation loss increases much larger than the divertor heat flux. This divertor heat flux level has been usually observed in relatively high density discharges with attached plasmas. Therefore, the present detachment is certainly triggered by the enhanced edge radiation loss.

4.6 Summary

The partial carbon radiation of C^{2+}–C^{5+} ions has been estimated for attached and detached plasmas by analyzing the intensity of CIII–CVI resonance lines. It is found that the P_{rad} (C^{3+}) is much stronger than P_{rad} (C^{2+}), P_{rad} (C^{4+}) and P_{rad} (C^{5+}) in both the attached and detached plasmas. The P_{rad} (C^{3+}) is much increased in the detached plasma with 6-O island, i.e., 40% to P_{rad}, while P_{rad} (C^{3+}) indicates only 8% to P_{rad} in the attached plasma. The P_{rad} (C^{3+}) is therefore thought to be the dominant origin for triggering the RMP-assisted detached plasma in LHD.

References

[1] M. Kobayashi, et al., Phys. Plasmas **17**, 056111 (2010).
[2] M. Kobayashi, et al., Nucl. Fusion **53**, 093032 (2013).
[3] S. N. Pandya, et al., Nucl. Fusion **56**, 046002 (2016).
[4] M. B. Chowdhuri, et al., Phys. Plasmas **16**, 062502 (2009).

[5] M. B. Chowdhuri, et al., Rev. Sci. Instrum. **78**, 023501 (2007) and Erratum: **84,** 109901 (2013).
[6] T. Oishi, et al., Plasma Fusion Res. **10**, 3402031 (2015).
[7] C. F. Dong, et al., Rev. Sci. Instrum. **81**, 033107 (2010).
[8] H. M. Zhang, et al., Jpn. J. Appl. Phys. **54**, 086101 (2015).
[9] X. L. Huang, et al., Rev. Sci. Instrum. **85**, 043511 (2014).
[10] C. F. Dong, et al., Rev. Sci. Instrum. **82**, 113102 (2011).
[11] H. P. Summers, et al., Plasma Phys. Control Fusion **48**, 263–293 (2006).

Chapter 5

Radial distributions of edge impurity emissions in detached plasma

5.1 Introduction

In Large Helical Device (LHD), the plasma detachment has been steadily operated without any external impurity gas feed by supplying the m/n = 1/1 resonant magnetic perturbation (RMP) field at plasma axis position of R_{ax} = 3.90 m [1-4]. In the R_{ax} = 3.90 m the radial profile of rotational transform, $\iota/2\pi$, becomes relatively flat and the radial position of $\iota/2\pi$ is located in stochastic magnetic field layer existing outside last closed flux surface (LCFS) where the magnetic field structure is entirely 3-dimensional [5-7]. The RMP-assisted plasma detachment is triggered when the density increases above a threshold value, e.g., 5×10^{13} cm^{-3}. After triggering the detachment an electron temperature flattening suddenly appears in the plasma edge [1]. The temperature flattening covers a wide range of plasma radii, e.g., from the $\iota/2\pi$ = 1 position in the stochastic layer to ρ = 0.9 inside LCFS. It is believed that the magnetic island with m/n = 1/1 mode is rapidly grown up. Therefore, it is important to verify the magnetic island formation during the RMP-assisted detachment. For the purpose a space-resolved extreme ultraviolet (EUV) spectrometer is utilized to experimentally examine the magnetic island formation by measuring the vertical profile of carbon line emissions of CIII to CVI during the plasma detachment. The effect of island on the radial location of carbon emissions is investigated at the top and bottom plasma edges close to the m/n = 1/1 island O-point and X-point, respectively.

5.2 Details of space-resolved EUV spectrometer

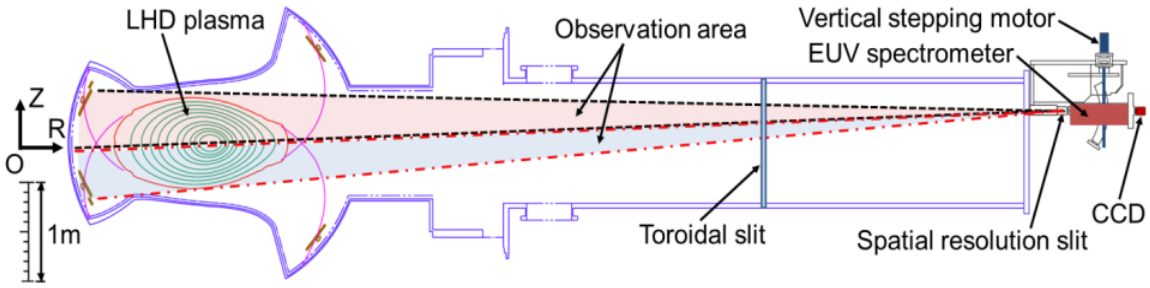

Fig. 5.1 Side view of space-resolved EUV spectrometer.

Space-resolved EUV spectroscopy has been developed in LHD for measuring the radial distribution of impurity line emissions [8–10]. As shown in Fig. 5.1, the space-resolved EUV spectrometer is installed on #10-O LHD port locating at toroidal position of $\phi = 324°$ and its optical axis is arranged perpendicular to the magnetic axis. The spectrometer consists of a 200-μm-width entrance slit, a 1-mm-width spatial resolution slit placed in front of the entrance slit, a concave varied-lines-pacing (VLS) grating and a back-illuminated charge-coupled device (CCD) detector.[3] Impurity emissions passing through the spatial resolution slit and entrance slit are refracted on the gold-coated 1200 grooves/mm grating with a sufficiently large dispersion. Then, the spectra in the wavelength range of $30 \leq \lambda \leq 500$ Å are recorded by the CCD installed behind the grating. The CCD size is 26.6×6.6 mm^2 with total pixel numbers of 1024×255 and pixel size of 26×26 μm^2. The pixel binning mode is usually used for the spatial distribution measurement to increase the readout speed. In the binning mode, a sub-image with 51×204 channels is read out at time interval of 100 ms by summing up 5 adjacent pixels and replacing into a single channel. The spectral intensity is absolutely calibrated on the basis of profile measurement of bremsstrahlung continua in EUV and visible ranges [11,12].

As shown in Fig. 5.1, the vertical profile of impurity emissions is projected on the CCD using the narrow spatial-resolution slit placed horizontally in the spectrometer. A vertical range of $\Delta Z = 530$ mm can be observed during a discharge, which corresponds to half of the plasma diameter at the short axis side of LHD elliptical plasma. In order to measure the full vertical profile with the space-resolved EUV spectrometer, the observation chord can be vertically scanned with a stepping motor installed on the spectrometer [4,5]. The vertical observation range can be therefore selected according to the experimental purpose. In the present study, the vertical profile of impurity emissions is separately measured at upper ($0 \leq Z \leq 530$ mm) and lower ($-530 \leq Z \leq 0$ mm) halves using two identical discharges. The full vertical profile ($-530 \leq Z \leq 530$ mm) is thus obtained by superposing the two vertical profiles measured at

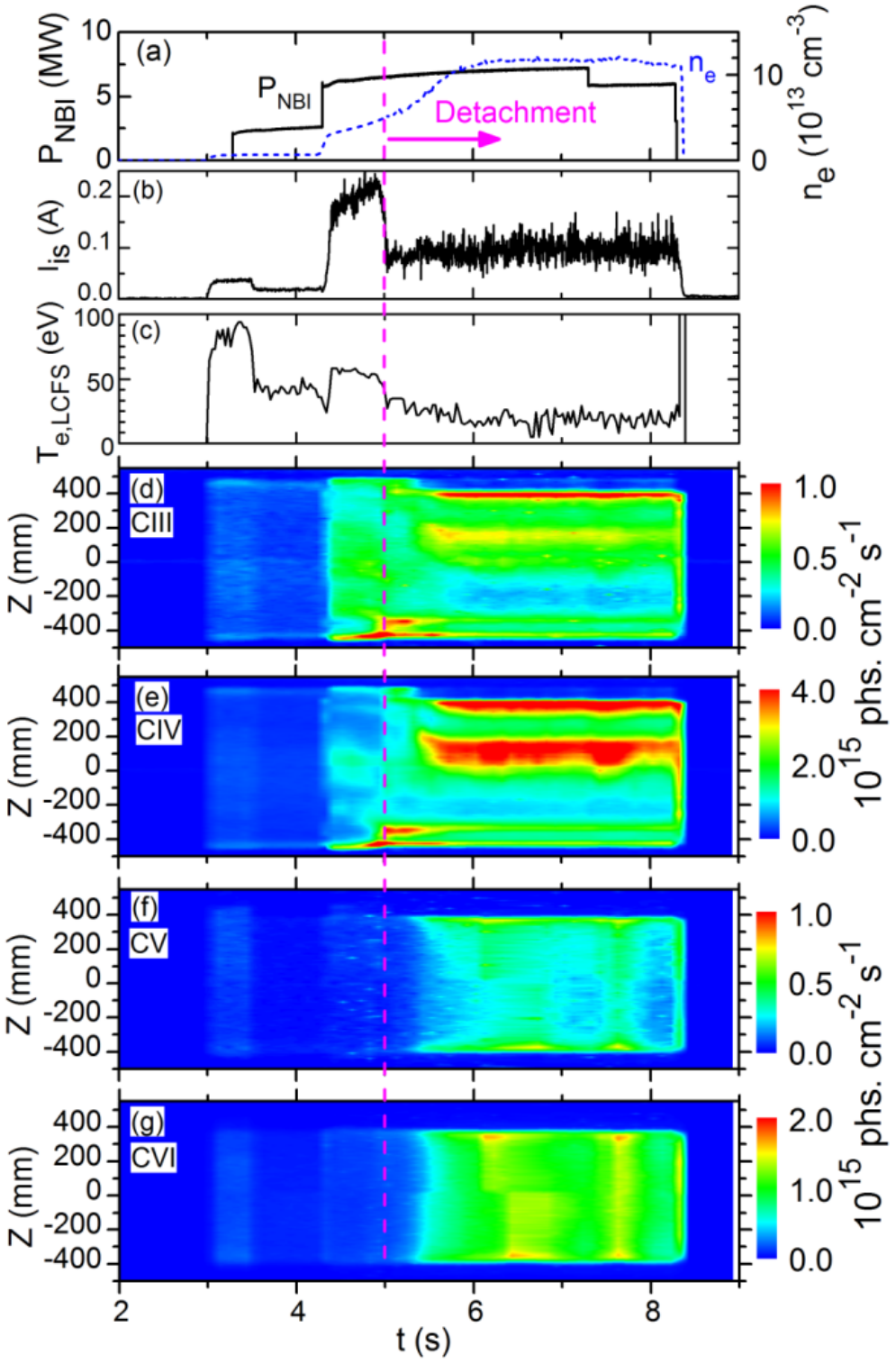

Fig. 5.2 Time behaviors of (a) NBI port-through power and line-averaged electron density, (b) ion saturation current, (c) electron temperature at LCFS and vertical profiles of (d) CIII (386.203 Å), (e) CIV (384.02 Å), (f) CV (40.27 Å) and (g) CVI (33.73 Å) in RMP-assisted detachment discharge.

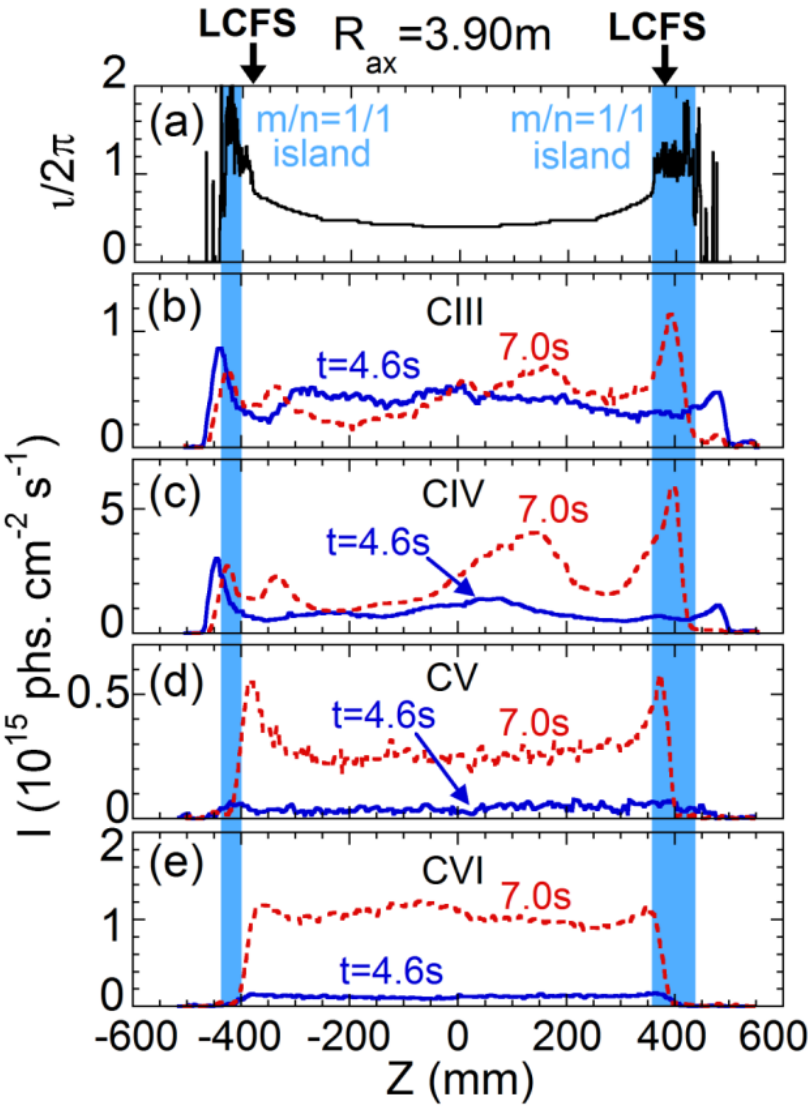

Fig. 5.3 Vertical profiles of (a) rotational transform (ι/2π), (b) CIII (386.203 Å), (c) CIV (384.174 Å), (d) CV (40.27 Å) and (e) CVI (33.73 Å) during attached (t = 4.6 s) and detached (t = 7.0 s) phases in Fig. 5.2. The radial location of ι/2π = 1 is indicated with hutched areas.

different vertical positions. The vertical position of each observation chord is accurately calibrated with the help of a toroidal slit with vertically 1.2m long comb-like apertures installed between the LHD plasma and the space-resolved EUV spectrometer [8].

5.3 Experimental results and discussion

5.3.1 Time evolution of carbon radial distribution

The plasma detachment is obtained in neutral-beam heated discharges at high densities above threshold density when the RMP field with m/n = 1/1 mode is supplied to the stochastic layer with $\iota/2\pi = 1$ position. The discharge waveform with typical detachment is shown in Figs. 5.2 (a)–(c). The RMP coil current is constantly maintained at I_{coil} = 3340 A during the discharge. In LHD two different island phases with m/n = 1/1 mode are selectable as '6-O island' and '7-O island' in which the island O-point is located at the outboard midplane of #6 ($\phi = 180°$) and #7 ($\phi = 216°$) toroidal sections, respectively [1]. Figure 5.2 shows the 6-O island case. The detachment transition occurs at t = 5.0 s when the electron density reaches $n_e \sim 5 \times 10^{13}$ cm^{-3}. The ion saturated current (I_{is}) shown in Fig. 5.2 (b) indicates a sudden decrease in the divertor particle flux. The electron temperature at the LCFS position ($T_{e,LCFS}$) also gradually decreases after the detachment transition [see Fig. 5.2 (c)].

Time development of vertical profiles of CIII (386.203 Å), CIV (384.174 Å), CV (40.27 Å) and CVI (33.73 Å) is also shown in Figs. 5.2 (d), (e), (f) and (g), respectively. Although the carbon emission intensities increase with electron density at the initial phase of the detachment, behaviors of CIII and CIV are clearly different from those of CV and CVI. The radial location of CIII and CIV emissions begins to shift inside just before the detachment transition at both top and bottom edges. On the contrary, the radial location of CV and CVI is entirely unchanged. These results strongly suggest an influence of m/n = 1/1 magnetic island formation in the plasma edge, which is discussed later in details.

5.3.2 Analysis and discussion on CIII–CVI vertical profiles

In order to examine the effect of magnetic island on carbon emission profiles, vertical profiles of CIII–CVI are compared with rotational transform in vacuum condition, as plotted in Fig. 5.3. The observation chords are shown in Fig. 5.4 with a Poincare plot of the edge magnetic field at #10-O toroidal section for the 6-O island case, which is calculated in the vacuum condition. It is clear that the island O-point is

near the top plasma edge, while island X-pint is near the bottom plasma edge. Before the detachment at t = 4.6 s, the CIII in Fig. 5.3 (b) and CIV in Fig. 5.3 (c) have a clear edge peak at both the top and bottom edges due to a long integration of the emission. During the detachment, on the other hand, the second edge peak is newly appeared in the CIII and CIV profiles at the island O-point location of $360 \leq Z \leq 430$ mm denoted with hatched area. In particular, it is clear in the CIII profile at the top edge, i.e., the weakened first peak at Z = 480 mm and the newly appeared second peak at Z = 400 mm. In addition, the CIII and CIV emissions are also increased at $0 \leq Z \leq 200$ mm reflecting the emission enhancement in the vicinity of outboard X-point divertor separatrix. In contrast, the radial position of CVI located at radially inside of the island is entirely unchanged during the detachment, while the intensity increases. Here, it should be noticed that the CVI intensity during the plasma detachment is still much smaller than that during the plasma attachment without RMP field. It indicates that the RMP field enhances the edge impurity screening.

Time behaviors of radial positions in the CIV (384.174 Å) edge peak at the top and bottom edges, i.e., Z_{Top} and Z_{Bottom}, are plotted in Figs. 5.5 (a) and (b), respectively. The closed circles and triangles indicate discharges with and without RMP, respectively. It is clearly seen that the radial position of CIV begins to move radially inside at t = 4.65 s before the detachment transition at both the top and bottom edges in the discharge with RMP, while the CIV radial position is entirely unchanged in the discharge without RMP. The values of Z_{Top} and Z_{Bottom} are also plotted as functions of electron density in Figs. 5.5 (c) and (d) for discharges with and without RMP. It is found that the CIV radial position in the discharge with RMP starts to move when the density reaches 3.8×10^{13} cm^{-3} and the detachment transition occurs at $n_e = 5.0 \times 10^{13}$ cm^{-3} after the CIV radial position is sufficiently changed. In the discharge without RMP, on the other hand, the CIV position is unchanged against density and the detachment does not occur even if the density is higher than 5.0×10^{13} cm^{-3}. In addition, the radial shift in the top edge peak (ΔZ_{Top}) is much larger than that in the bottom edge peaks (ΔZ_{Bottom}) during the detachment, i.e., $\Delta Z_{Top} \sim 80$ mm and $\Delta Z_{Bottom} \sim 20$ mm. As shown in Fig. 5.4, the island O- and X-points are located near the top and bottom plasma edges, respectively. Therefore, the difference between ΔZ_{Top} and ΔZ_{Bottom} observed here indicates a clear evidence of m/n = 1/1 magnetic island suddenly grown up during the plasma detachment. The result concludes that formation of a big magnetic island expanded into magnetic surface region of ρ=0.9 is possible by supplying the RMP field, even if the magnetic resonance exists in the stochastic magnetic field layer.

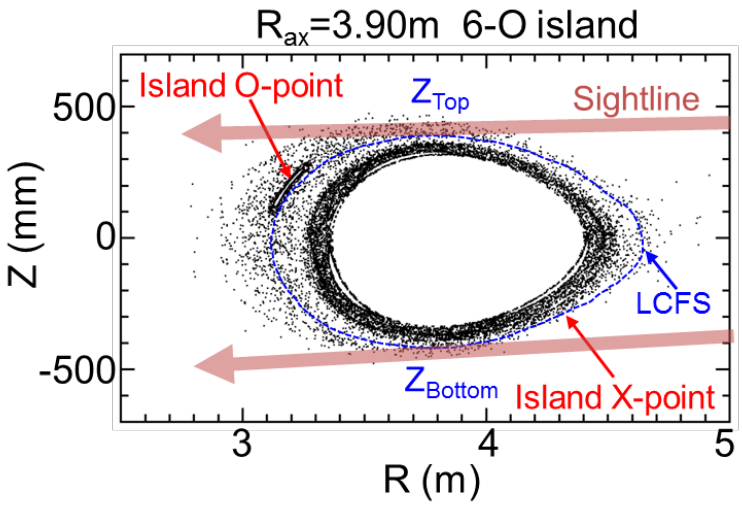

Fig. 5.4 Observation chords and Poincare plot of edge magnetic field structure at #10-O toroidal section with m/n = 1/1 island calculated in vacuum condition.

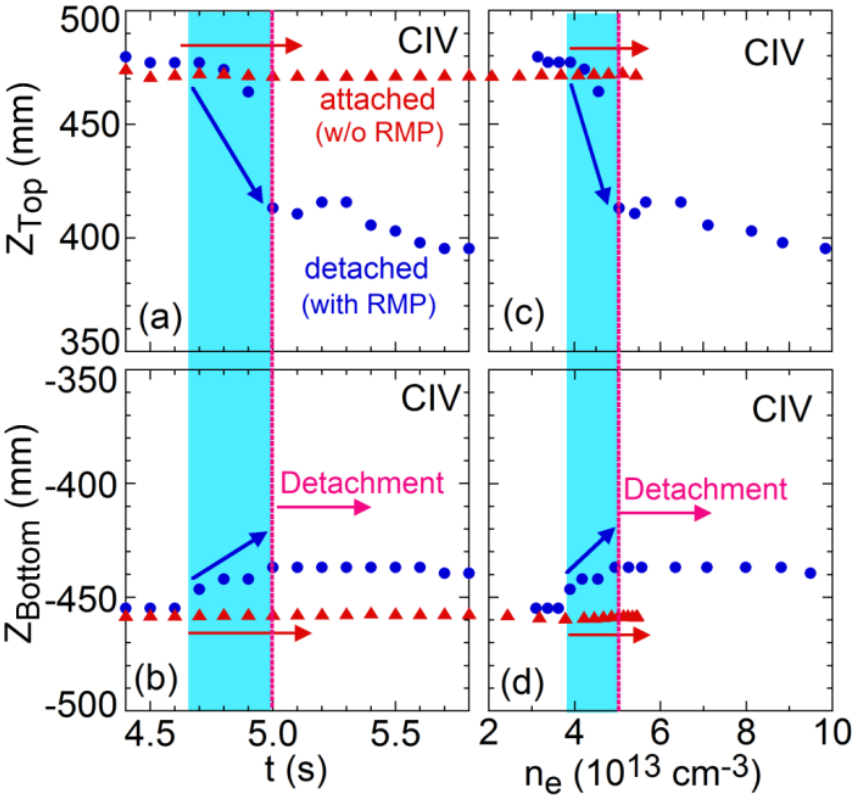

Fig. 5.5 Time behaviors of CIV (384.174 Å) vertical positions at (a) top and (b) bottom edges and density dependences of CIV vertical positions at (c) top and (d) bottom edges in discharges without (closed triangles) and with (closed circles) RMP.

5.4 Summary

The radial distribution of impurity carbon emissions has been measured during plasma detachment in LHD with the space-resolved EUV spectroscopy. The effect of RMP field on the edge impurity emission can be clearly observed from the radial distribution measurement. It is found that the radial position of CIII and CIV radially shifts inside before the RMP-assisted detachment transition, but it is unchanged in general discharges without RMP. The difference in the radial shift between the top and bottom CIV edge peaks experimentally confirms the appearance of m/n = 1/1 island during the plasma detachment.

References

[1] M. Kobayashi, et al., Phys. Plasmas **17**, 056111(2010).
[2] M. Kobayashi, et al., Nucl. Fusion **53**, 093032 (2013).
[3] S. N. Pandya, et al., Nucl. Fusion **56**, 046002 (2016).
[4] H. M. Zhang, et al., Plasma Fusion Res. **11**, 2402019 (2016).
[5] S. Morita, et al., Plasma Phys. Control. Fusion **56**, 094007 (2014).
[6] M. B. Chowdhuri, et al., Phys. Plasmas **16**, 062502 (2009).
[7] N. Ohyabu, et al., Nucl. Fusion **34**, 387 (1994).
[8] C. F. Dong, et al., Rev. Sci. Instrum. **81**,033107 (2010).
[9] E. H. Wang, et al., Rev. Sci. Instrum. **83**, 043503 (2012).
[10] H. M. Zhang, et al., Jpn. J. Appl. Phys. **54**, 086101 (2015).
[11] C. F. Dong, et al., Rev. Sci. Instrum. **82**, 113102 (2011).
[12] X. L. Huang, et al., Rev. Sci. Instrum. **85**, 043511 (2014).

Chapter 6

Vertical profiles and 3-D structures of carbon emissions in detached plasma

6.1 Introduction

Heat load mitigation of divertor plates is one of the critical issues in the future fusion device such as ITER [1,2]. The peak power load on ITER divertor plates is estimated to be more than 20 MW/m^2, which is almost two times higher than the present engineering limit (~10 MW/m^2) [3]. The plasma detachment using working gas or gaseous impurities, which has been attempted in many tokamak devices, is a possible solution for the heat load mitigation [4–10]. The H-mode plasma with complete detachment has been realized without deterioration of the energy confinement in ASDEX Upgrade with feedback-controlled gas puffing system using deuterium and neon. The total radiation reaches 90% of the input power during the plasma detachment [5,6]. In "hybrid" H-mode plasmas of DIII-D, the peak heat flux at the outer divertor plate is reduced by a factor of 2.5 using argon puff carried out near the outer divertor target [7]. In the detached H-mode plasma of JT-60U, the radiation power from neon ions at the inner divertor reaches 55% to the total radiation [8]. In JET and Alcator C-Mod, on the other hand, the completely detached H-mode plasma is successfully obtained using only deuterium gas puffing [9, 10].

ITER operation scenario is considered with the H-mode [1,2]. In the present experiments of tokamaks with H-mode, then, a steady sustainment of the plasma detachment becomes an important subject because a large heat flux based on the edge localized mode (ELM) may penetrate the edge high radiation region and reaches the divertor plates [9]. In addition, the operation window of the plasma detachment with H-mode is very narrow [4–10].

In helical devices another technique for realizing the detached plasma has been attempted in Wendelstein 7-AS (W7-AS) and in Large Helical Device (LHD) using the resonant magnetic perturbation (RMP) coils without any external impurity gas feed

[12–14]. The heat load on divertor plates decreases by a factor of 3–10 during the detachment phase basically without degradation of energy confinement. This method seems to be attractive because the detached plasma with RMP may also mitigate a big ELM burst in tokamaks [12]. Dedicated experiments have been performed in W7-AS and LHD to investigate the operation window for a steady-state sustainment of high-performance plasmas. In W7-AS, it is found that the island size and field line pitch in the island at the plasma edge region influence the stability of detached plasmas. In LHD it is also found that the radial location of m/n = 1/1 island supplied by RMP in the plasma edge is a critical factor for successful achievement of the detached plasma. The detached plasma in LHD can be achieved when the m/n = 1/1 island is created only in the edge stochastic magnetic field layer. At present, however, the reason why the radial location of m/n = 1/1 island is critical for achieving the plasma detachment in LHD is unclear. In addition, the concentration of impurity iron originating in the first wall protection tiles made of stainless steel is very low in general LHD discharges, in particular, at high-density discharges [15]. Carbon released from graphite divertor plates is thought to be a possible impurity source which can contribute to the high edge radiation during plasma detachment [12], although the energy loss channel in the RMP-assisted detached plasma without external impurity gas is still an open question. Therefore, the study of carbon behaviors during the plasma detachment in LHD is very important to find a cause triggering the detachment transition.

A 2-D space-resolved EUV spectrometer in LHD has been upgraded to measure the vertical profile and 2-D distribution of impurity line emissions in short-pulse neutral-beam-injection (NBI) discharges mainly by increasing the spectrometer scanning speed, installing a thin filter to eliminate the NBI high-energy neutral particles and adopting a new analysis method [16–18]. As a result, it becomes possible to measure the 2-D distribution in detached plasmas. The influence of the m/n = 1/1 magnetic island formed by RMP coils on the edge carbon behavior can then be studied with the upgraded spectrometer system. The NBI discharge shows entirely different behaviors between the two magnetic axis positions of R_{ax} = 3.75 m and 3.90 m when the RMP is supplied. The detachment is easily triggered by the RMP at R_{ax} = 3.90 m in which the m/n = 1/1 island locates just outside the last closed flux surface (LCFS), while the discharge has basically no response to the RMP supply at R_{ax} = 3.75 m in which the island locates just inside the LCFS [19]. On the other hand, the CIII and CIV are located outside the LCFS and the CV and CVI are located in the vicinity of LCFS. Therefore, the observation of radial profiles and 2-D distributions of carbon ions is very important to study the influence of the island in relation to the formation of plasma detachment because the radial position of m/n = 1/1 island is located just inside and outside the LCFS at R_{ax} = 3.75 m and 3.90 m configurations, respectively. The measured vertical profile and 2-D distribution of carbon emissions are also analyzed with three-dimensional (3-D) edge plasma transport code, EMC3-EIRENE.

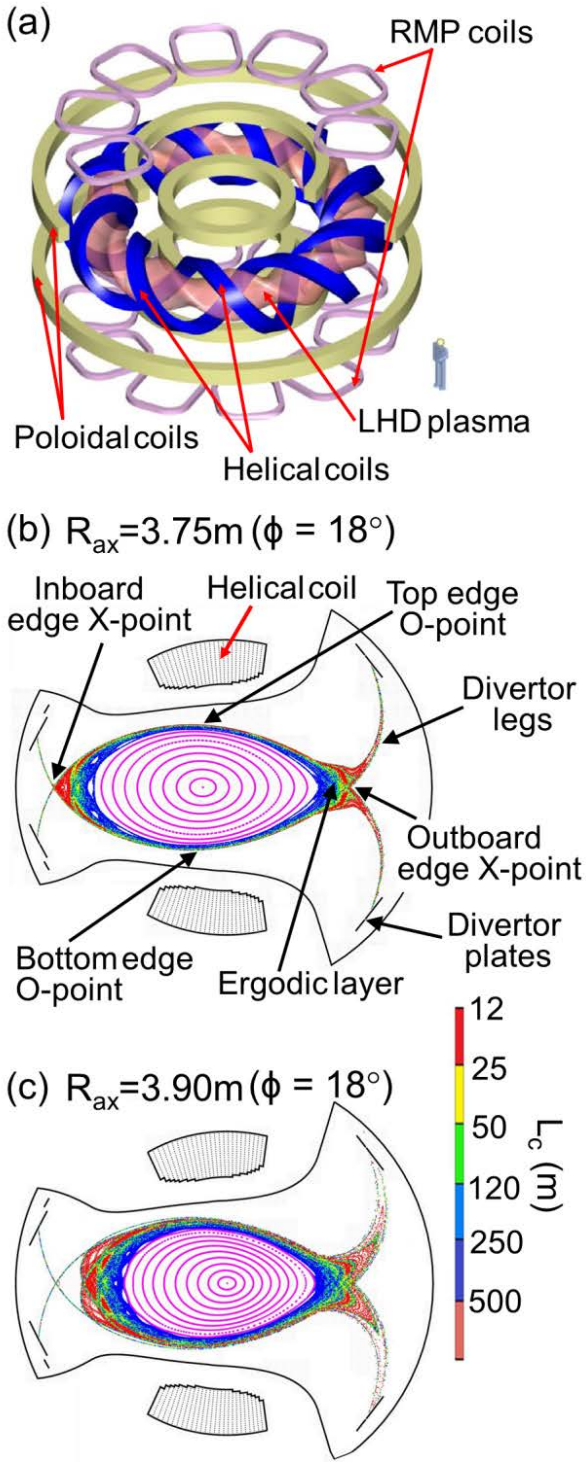

Fig. 6.1 (a) Bird's eye view of helical coils, RMP coils and toroidal plasma shape in LHD and connection lengths (L_c) in the ergodic layer with magnetic axis of (b) R_{ax} = 3.75 m and (c) R_{ax} = 3.90 m.

In the present paper, the edge magnetic field structure and RMP coil system in LHD are described in Sect. 6.2. The EUV and VUV spectroscopy are briefly explained in Sect. 6.3. Then, the vertical profile and 2-D distribution of impurity carbon emissions from NBI discharges at R_{ax} = 3.75 m and 3.90 m are presented with data analysis by the simulation in Sect. 6.4 and Sect. 6.5, respectively. Finally, the study is summarized in Sect. 6.6.

6.2 Edge island formation by RMP coils in LHD

The magnetic field for plasma confinement in LHD is basically produced by two superconducting helical coils with poloidal and toroidal pitch numbers of l = 2 and n = 10, respectively, as shown in Fig. 6.1 (a), while three pairs of superconducting poloidal coils are used for the control of the plasma position, the shaping of the plasma cross section and the cancelling of the stray magnetic field. The magnetic axis position is varied at major radius between R_{ax} = 3.50 m and 4.00 m in general experiments. The averaged plasma minor radius defined by the last closed flux surface (LCFS) takes the maximum value of 64 cm at R_{ax} = 3.60 m. The core plasma in LHD is always accompanied by a stochastic magnetic layer called the "ergodic layer" formed outside the LCFS, which is originated in the presence of higher order Fourier components in the magnetic field created by the helical coils [21]. Since the magnetic islands with different mode numbers overlap each other in the ergodic layer, the magnetic field structure becomes entirely three-dimensional. The magnetic field structure in the ergodic layer at a horizontally elongated plasma cross section (ϕ = 18°) is shown in Figs. 6.1 (b) and (c) for R_{ax} = 3.75 m and 3.90 m configurations, respectively. It indicates that the magnetic field connection length, L_c, in the ergodic layer distributes at the extremely wide range of $10 \leq L_c \leq 2000$ m. In addition, two edge X-points appears at the inboard and outboard sides in the figure. In the present paper, those are called "inboard edge X-point" and "outboard edge X-point." In contrast with this, two positions closed to the helical coil are called "top edge O-point" and "bottom edge O-point." It is clear from the figures that the thickness of the ergodic layer, λ_{erg}, varies with the poloidal angle. The maximum and minimum thicknesses of the ergodic layer at the ϕ = 18° toroidal position are given at the edge X- and O-points, respectively. The magnetic field line called "divertor leg" originating in the vicinity of the edge X-points is directly connected to the divertor plates made of graphite.

The magnetic field structure in the ergodic layer is very different between the two magnetic axis positions of R_{ax} = 3.75 m and 3.90 m. The LCFS position becomes smaller when the magnetic axis position is shifted outward, whereas the outside boundary of the ergodic layer basically does not change at all. As a result, the λ_{erg} in the R_{ax} = 3.90 m configuration is much larger than that in the R_{ax} = 3.75 m configuration.

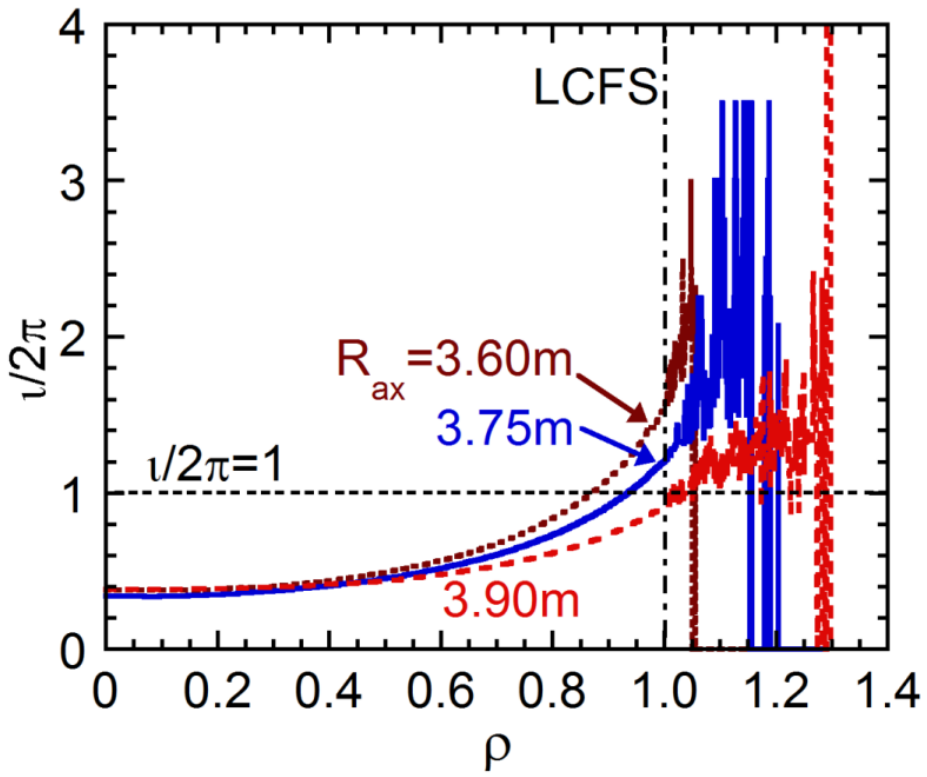

Fig. 6.2 ι/2π profile as a function of minor radius (ρ) for R_{ax} = 3.60 m, 3.75 m and 3.90 m. LCFS position is indicated with a dashed-dotted line.

The λ_{erg} has the biggest value in the inboard edge X-point of the horizontally elongated plasma cross section (ϕ = 18°) at R_{ax} = 3.90 m configuration, i.e., $\lambda_{erg} \sim 60$ cm, while the magnetic field lines at the outboard edge X-point are dominantly connected to the divertor plates, as seen in Fig. 6.1 (c). Many magnetic field lines with shorter L_c ($12 \leq L_c \leq 25$ m) that appearing in the vicinity of the outboard X-point are connected to the divertor plates through the divertor legs in the R_{ax} = 3.90 m configuration [22].

An additional ten pairs of normal conducting coils are installed at the top and the bottom on the LHD as shown in Fig. 6.1 (a) to create a large magnetic island with m/n=1/1 mode in the plasma edge, which are now called resonant magnetic perturbation (RMP) coils. The RMP coil system was originally used for the local island divertor experiment to demonstrate an efficient particle exhaust [15]. As the island size can be easily controlled by the coil current, the maximum RMP coil current of I_{coil} = 3340 A is used in the present study to trigger the plasma detachment. The edge magnetic field structure with m/n=1/1 island is then kept constant during the discharge by presetting the coil current.

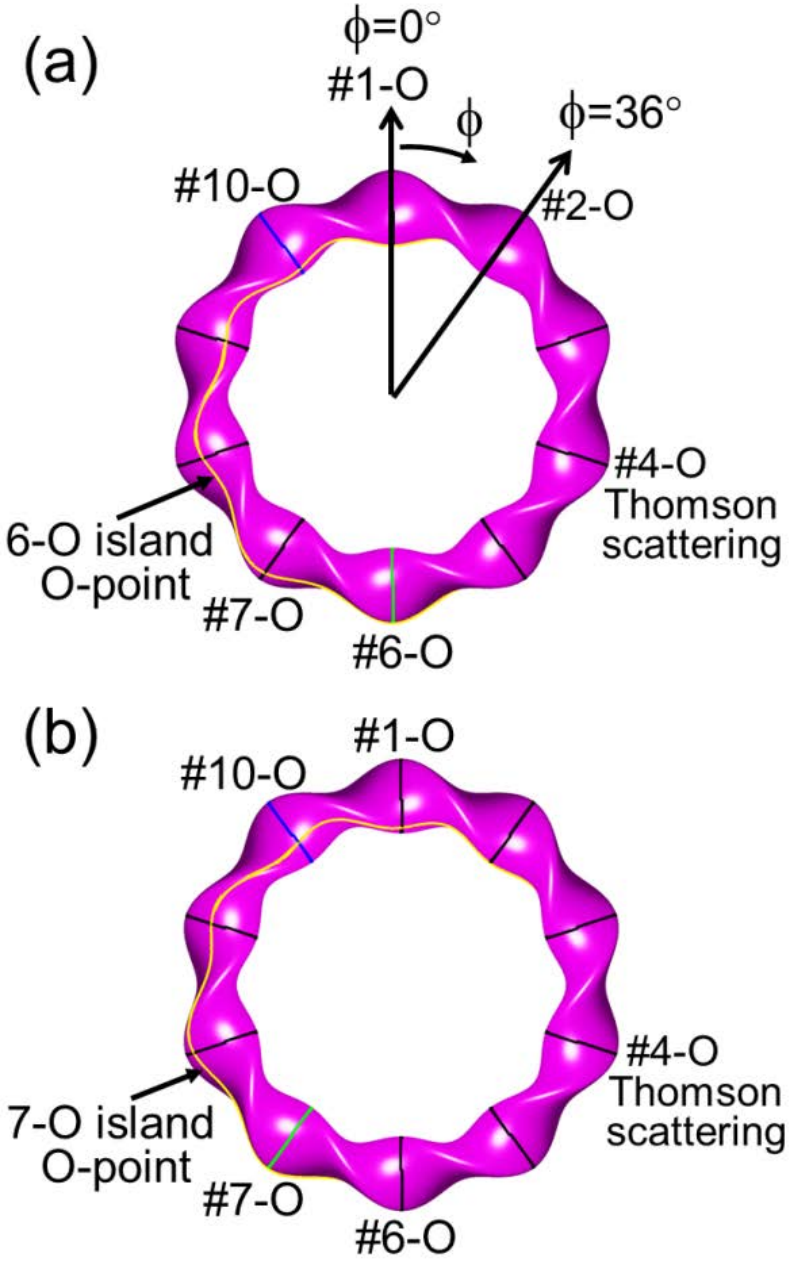

Fig. 6.3 Schematic view of the O-point trajectory of m/n = 1/1 magnetic island on a flux surface at $\iota/2\pi = 1$ for (a) 6-O and (b) 7-O islands in R_{ax} = 3.75 m configuration.

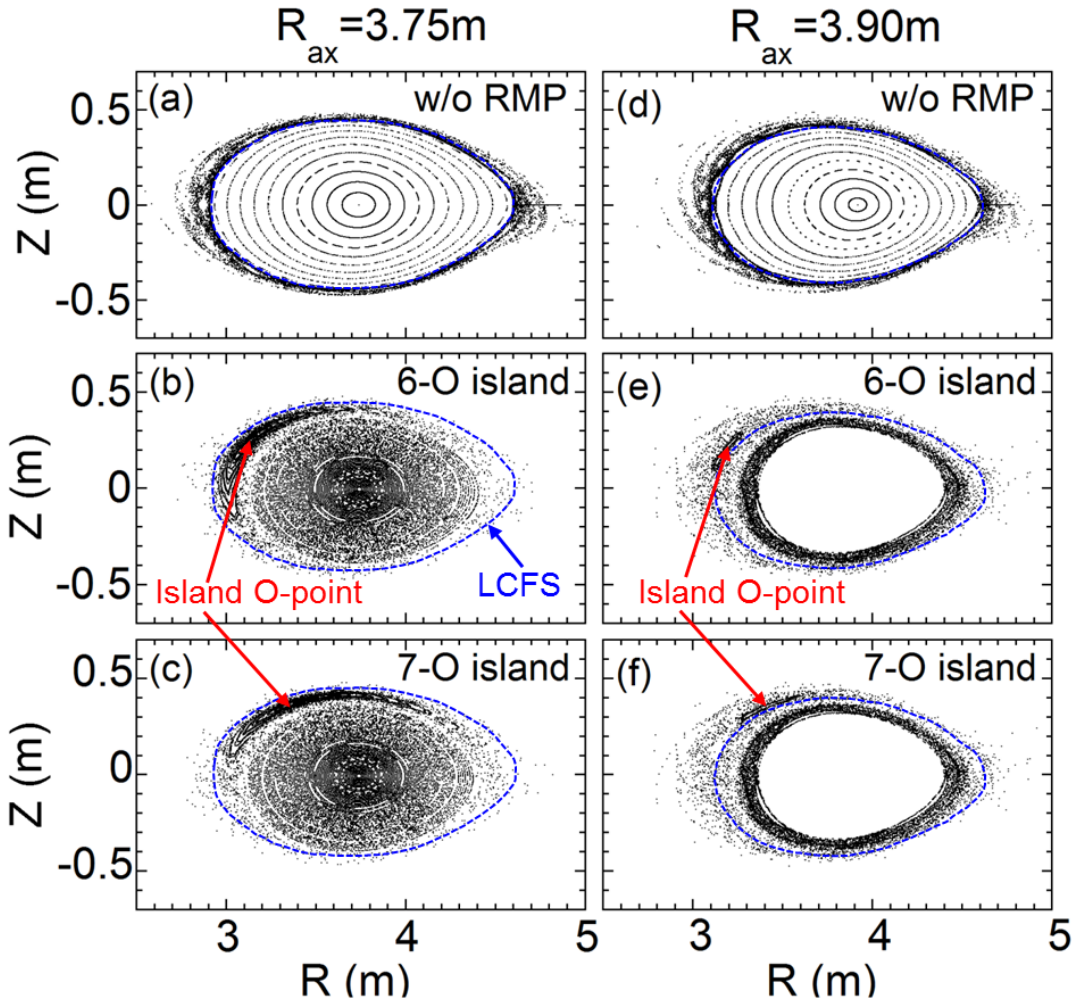

Fig. 6.4 Magnetic field structures in vacuum condition at #10-O toroidal location; (a) without RMP, (b) 6-O island and (c) 7-O island at R_{ax} = 3.75 m and (d) without RMP, (e) 6-O island and (f) 7-O island at R_{ax} = 3.90 m. The LCFS is indicated with dashed line in each figure.

Radial profiles of the rotational transform ($\iota/2\pi$) in LHD are shown in Fig. 6.2 as a function of minor radius (ρ) for magnetic axis positions of R_{ax} = 3.60 m, 3.75 m and 3.90 m. The $\iota/2\pi$ profile becomes gradually flat when the magnetic axis shifts outward. According to the change, the radial position of $\iota/2\pi$ = 1 also moves outside, i.e., ρ = 0.93 inside LCFS (ρ = 1) at R_{ax} =3.75 m and ρ = 1.03 just inside the ergodic layer at R_{ax} = 3.90 m. In the case of R_{ax} = 3.90 m, then, any clear magnetic island formation has not been observed in general discharges because the RMP field has in principle no clear magnetic resonance of m/n = 1/1 mode in the stochastic magnetic field layer, while a considerably large island always has been formed with the RMP field in the R_{ax} = 3.60 m and 3.75 m configurations. This is described below in detail.

Figure 6.3 shows the top view of LHD plasma. The poloidal position of m/n = 1/1 island can be changed slightly by phasing the RMP coil currents. The poloidal position of the island O-point is also indicated in the figures. The trajectory of the island O-point formed in the midplane at #6-O (ϕ = 180°) and #7-O (ϕ = 216°) outboard diagnostic ports is plotted in Figs. 6.3 (a) and (b), respectively. Here, we define the two configurations as "6-O island" and "7-O island." In practice, the trajectory of the island O-point in Fig. 6.3 is traced on a flux surface with $\iota/2\pi$ = 1 at R_{ax} = 3.75 m configuration. The island O-point is then located for both the 6-O and 7-O island configurations in the inboard side of horizontally elongated plasma cross section at the #10-O (ϕ = 326°) diagnostic port where the spectrometers are installed, while the poloidal angle of the island O-point is slightly different between the two.

The poloidal structure of the magnetic island created by the RMP coils is generally calculated in the vacuum condition for the core plasma inside the LCFS. If the island exists in the ergodic layer, the structure can be obtained by tracing the 3-dimensional trajectory of each magnetic field line. The Poincaré plot of magnetic field lines without RMP coils in the ergodic layer is shown in Figs. 6.4 (a) and (d) with magnetic surfaces for R_{ax} = 3.75 m and 3.90 m, respectively. Several intrinsically existing small magnetic islands appear in the ergodic layer, while well-arranged magnetic surfaces are seen in the plasma core region. The island structure with RMP field at R_{ax} = 3.75 m is plotted in Figs. 6.4 (b) and (c) for 6-O and 7-O island cases, respectively. Since the island exists inside the LCFS denoted with dashed line, the magnetic field structure in the ergodic layer is not traced in the figures because it is nearly the same as Fig. 6.4 (a). The island with m/n = 1/1 mode is localized at the inboard side of #10-O toroidal position, although the poloidal position of the island is a little different between 6-O and 7-O configuration. In the case of R_{ax} = 3.90 m, on the other hand, the island structure becomes much different from the R_{ax} = 3.75 m case because the $\iota/2\pi$ = 1 position is located in the ergodic layer. The magnetic field lines at R_{ax} = 3.90 m configuration with RMP coils is plotted in Figs. 6.4 (e) and (f) for 6-O and 7-O islands, respectively. In order to make clear the island position the number of mesh

in the calculation is increased compared to Figs. 6.4 (a) and (d). It is then noted that the magnetic field structure in the plasma core is not plotted in Figs. 6.4 (e) and (f) because the plasma core is entirely black. A small island can be seen in the ergodic layer at just outside the LCFS of the figures, while the poloidal shape is entirely different from the ordinary island seen in the plasma core. In the present study, a poloidal position opposite to the island O-point is called the island X-point, although the island X-point is not clearly visible in the Poincaré plot.

6.3 Experimental setup

The EUV and VUV spectroscopic systems are installed on the #10-O LHD port ($\phi = 324°$). In the present study, two EUV spectrometers named EUV_Short (10–100Å) and EUV_Long (50–650 Å) and two 20 cm normal incidence VUV spectrometers named VUV_109L (300–1000Å) and VUV_106R (970–1900 Å) are used for simultaneous measurement of carbon spectra with high-time resolution of 5ms [23–25]. Two other space-resolved EUV spectrometers named EUV_Short2 (10–100Å) and EUV_Long2 (50–650Å) observe the vertical profile and 2-D distribution of carbon line emissions, respectively [16–18, 26]. The intensities of EUV and VUV spectra are absolutely calibrated on the basis of profile measurements of the bremsstrahlung continuum in the visible and EUV ranges [18, 27].

The EUV_Long2 spectrometer is developed to observe both the vertical profile and the 2-D distribution of impurity line emissions [17, 18, 22].As shown in Fig. 6.5 (a), the spectrometer optical axis can be horizontally scanned around a pivot using a horizontal stepping motor. When the optical axis of spectrometer is fixed perpendicular to the magnetic axis, i.e., $\theta = 0°$, a vertical profile of impurity emissions can be measured in the vertical observation range of $-600 \leq Z \leq 600$ mm at the horizontally elongated plasma cross section. On the other hand, the 2-D distribution of impurity emissions can be measured by horizontally scanning the optical axis from $\theta = -2°$ to $+2°$ during a steady phase of discharges. As shown in Fig. 6.5 (b), a large trapezoidal diagnostic port with a vertical size of 1200 mm and a horizontal size of 700 mm is used for the 2-D distribution measurement. Therefore, the impurity emissions from inboard and outboard edge X-points can be separately measured, as indicated in Fig. 6.5 (b) with dotted and dashed lines, respectively. The m/n = 1/1 island twists on the flux surface of $\iota/2\pi = 1$ with the movement of toroidal location (see Fig. 6.3). The vertical position of island O- and X-points changes against the horizontal distance in the 2-D observation range. Those trajectories in the 2-D observation range are shown in Figs. 6.6 (a) and (c) for 6-O island and Figs. 6.6 (b) and (d) for 7-O island. This is because the vertical

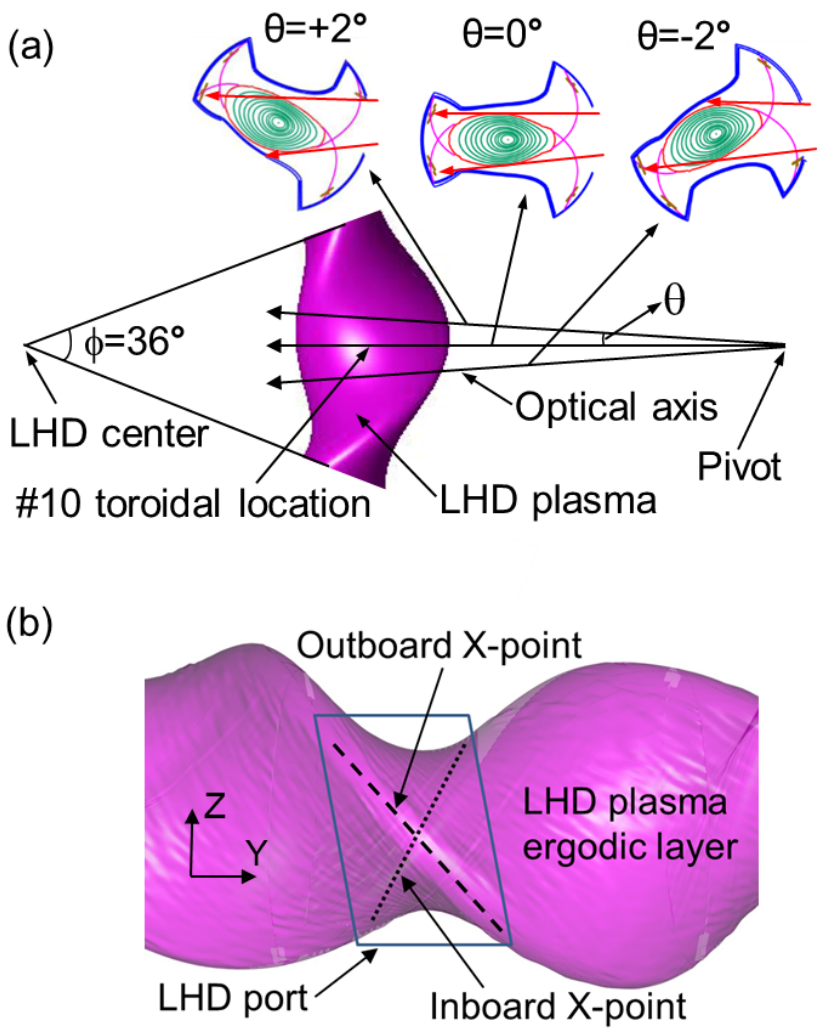

Fig. 6.5 (a) Top and (b) horizontal views of LHD plasma shape with observation area of EUV_Long2 spectrometer system at #10-O toroidal location. Three poloidal cross sections of LHD plasma are also shown for three different angles in the spectrometer optical axis of θ = +2°, 0° and −2°. The top and bottom boundaries of the vertical observation range are indicated by two arrows in each poloidal cross section. The #10-O LHD diamond port for the 2-D distribution measurement is indicated by a solid line. Inboard and outboard X-point trajectories are indicated by dotted and dashed lines, respectively.

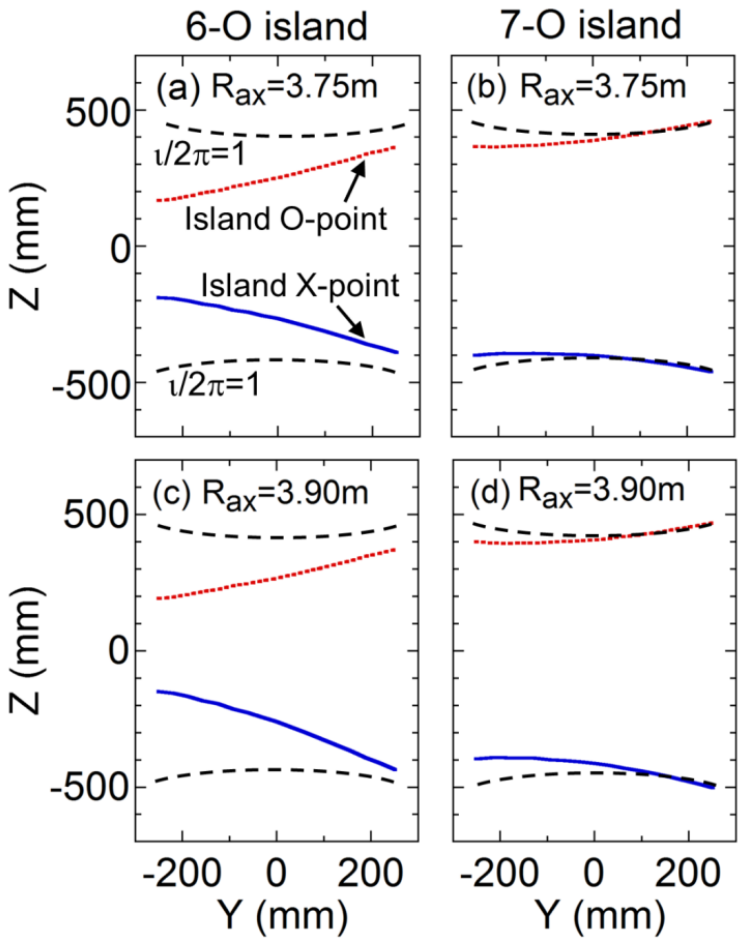

Fig. 6.6 Vertical positions of O-point (dotted line) and X-point (solid line) of the m/n = 1/1 magnetic island within the observation area of EUV_Long2 spectrometer installed on #10-O LHD port; (a) 6-O and (b) 7-O islands at R_{ax} = 3.75 m configuration and (c) 6-O and (d) 7-O islands at R_{ax} = 3.90 m configuration. Radial location of ι/2π = 1 is also indicated with dashed line in each figure.

locations of ι/2π = 1 are also indicated with dashed lines in each figure. The 6-O island largely changes the vertical position of the island O- and X-points compared to the 7-O island for both the magnetic axis positions of R_{ax} = 3.75 m and 3.90 m, e.g., Z = 165–365 mm for 6-O island and Z = 365–460 mm for 7-O island at R_{ax} = 3.75 m. Because the vertical position of the island O- and X-points is slightly different between R_{ax} = 3.75 and 3.90 m, reflecting the different edge rotational transform shown in Fig. 6.2.

6.4 Impurity carbon emissions at R_{ax} = 3.75 m configuration with island inside LCFS

Carbon and iron ions always exist in LHD discharges as the intrinsic impurity, which originate in the graphite divertor tiles and stainless steel first wall, respectively. The amount of iron impurity is, however, relatively small in most of LHD discharges due to the presence of the screening effect in the ergodic layer. Although the iron radiation still exists in the plasma core, it can be entirely ignored in the analysis of edge plasma including the ergodic layer because the line emissions from low-ionized iron are negligibly small in both the VUV and the EUV wavelength ranges. Therefore, the carbon ions can mainly contribute to the edge radiation in LHD discharges. Line emissions of CIII –CVI are then studied in discharges at R_{ax} = 3.75 and 3.90 m because the m/n=1/1 island in inward-shifted magnetic axis positions such as R_{ax} = 3.60 m is located deep inside the core plasma. As the first step in the study, therefore, the vertical profile and 2-D distribution of CIII–CVI are analyzed in discharges with R_{ax} = 3.75 m.

6.4.1 Discharge waveform and radial profiles of n_e and T_e

A discharge initiated by electron cyclotron heating (ECH) in R_{ax} = 3.75 m configuration can be steadily maintained with negative-ion-source-based NBIs (n-NBI) at the toroidal magnetic field of B_t = –2.64 T. The minus value means counter-clockwise direction in the toroidal filed. The waveform of typical discharges with and without RMP is shown in Fig. 6.7. A constant electron density (n_e) is kept during t = 4–8 s by controlling the hydrogen gas puffing rate, while the density in the discharge with RMP is slightly smaller than that without RMP, i.e., n_e = 4.0 and 4.5 × 10^{13} cm^{-3} for discharge with and without RMP, respectively. The central electron temperature (T_{e0}) shows a constant value around 1.8 keV during t = 4–8 s for both discharges. The plasma stored energy (W_p) in the discharge with RMP is significantly lower than that in the discharge without RMP reflecting the edge temperature reduction as seen in Fig. 6.8 (b). The radiation loss power (P_{rad}) in the discharge with RMP also indicates a lower value compared to that without RMP, mainly reflecting the reduced edge density as seen in Fig. 6.8 (a). The reduction of edge radiation is also observed in carbon line emissions of CIII (386.203 Å), CIV (384.174 Å), CV (40.27 Å) and CVI (33.73 Å) plotted in Figs. 6.7 (f), (g), (h) and (i), respectively.

The radial profiles of n_e and T_e measured with Thomson scattering diagnostic along major radius direction in the horizontally elongated plasma cross section at #4-O (ϕ = 144°) toroidal location are shown in Fig. 6.8 for discharges without and with RMP.

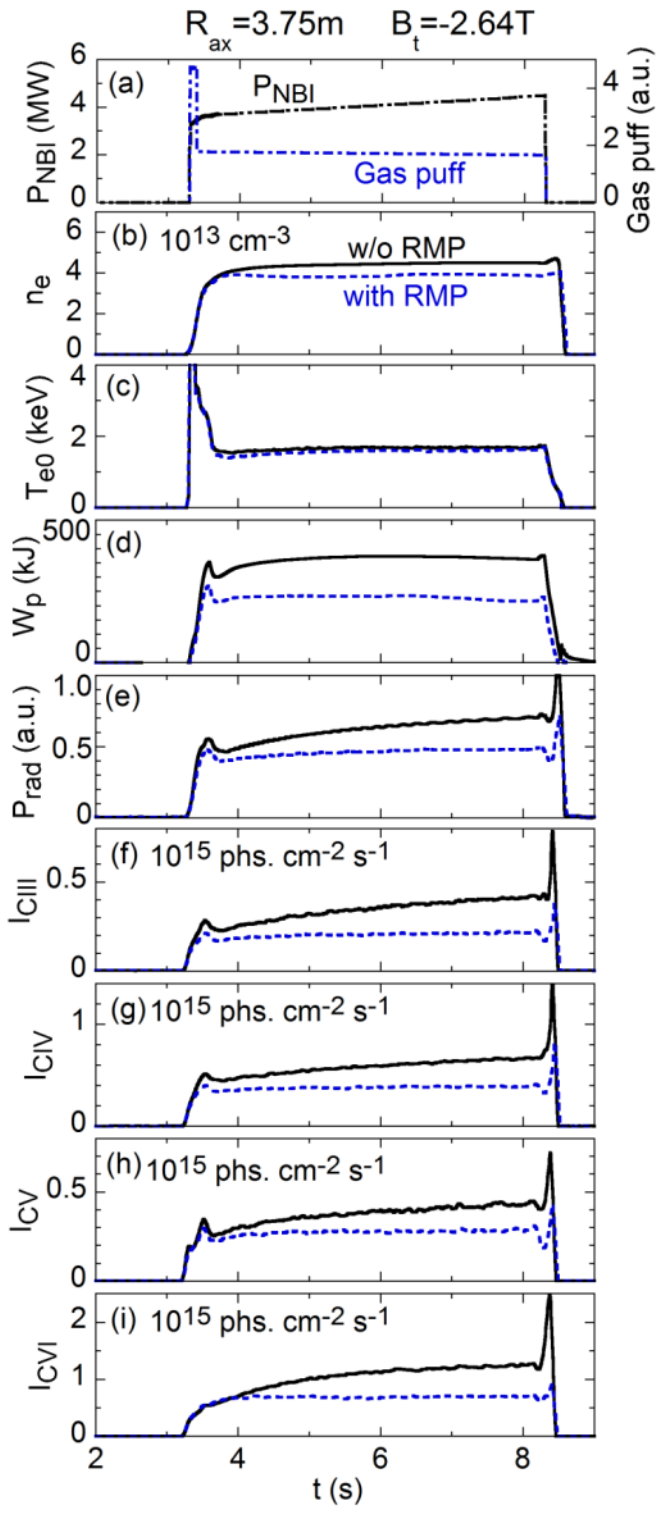

Fig. 6.7 Time behaviors of (a) NBI port-through power and hydrogen gas puffing, (b) line-averaged electron density, (c) central electron temperature, (d) stored energy, (e) radiation loss power, (f) CIII (386.203 Å), (g) CIV (384.174 Å), (h) CV (40.27 Å) and (i) CVI (33.73 Å) in discharges at R_{ax} = 3.75 m without (solid line) and with RMP (dashed line).

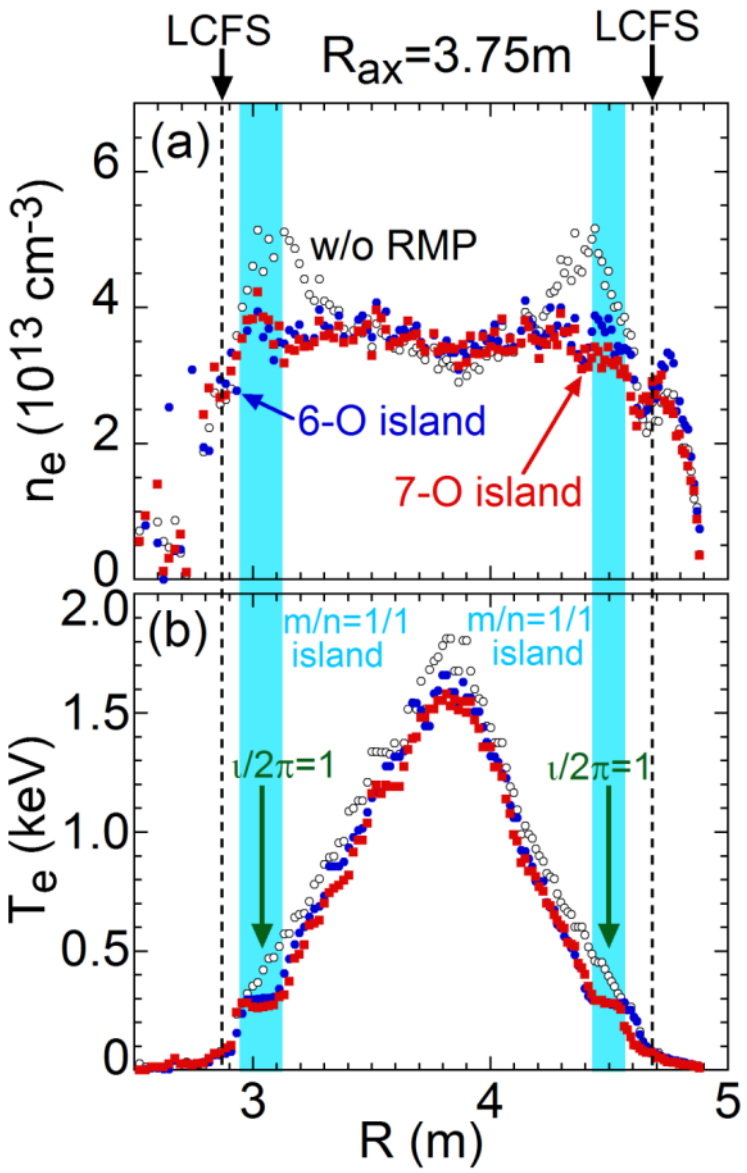

Fig. 6.8 Radial profiles of (a) n_e and (b) T_e in discharges at R_{ax} = 3.75 m without RMP (open circles), with 6-O island (solid circles) and with 7-O island (solid squares). Radial locations of LCFS and $\iota/2\pi$ = 1 are indicated with dashed lines and vertical arrows, respectively. The radial range of m/n = 1/1 island is indicated with shaded area.

The hollow density profile always observed in the discharge without RMP is changed to a flat density profile when the RMP is supplied. The m/n = 1/1 magnetic island is clearly identified at $\iota/2\pi = 1$ position indicated with vertical arrows inside the LCFS, which is also denoted with dashed lines. The radial width of m/n = 1/1 island is denoted with shaded area. Since the #4-O toroidal port is away from the #6-O and #7-O toroidal ports by $\phi = 72°$ and 108°, respectively, the edge T_e flattening can be observed at both the inboard and the outboard sides. The shape of T_e flattening is slightly different between the 6-O and 7-O islands reflecting the small different poloidal angle of the island. Since the temperature at the island ranges in $250 \leq T_e \leq 300$ eV and is much higher than the ionization energy of C^{2+} (48 eV) and C^{3+} (64eV) ions, the radiation from such ions is not fully affected by the appearance of island. The core T_e slightly decreases with the edge T_e flattening, whereas the T_e outside the island is almost unchanged.

6.4.2 EMC3-EIRENE code for data analysis

The 3-D distributions of the density of carbon ions and resultant carbon line emissions of CIII (386.203 Å), CIV (312.42 Å), CV (40.27 Å) and CVI (33.73 Å) are simulated with a 3-D edge plasma transport code EMC3-EIRENE. The EMC3 code for solving the fluid equations of particle, momentum and energy in steady state is coupled with the EIRENE code for solving the kinetic neutral transport equations coupled with the recycling neutrals from divertor plates and the first wall [28, 29].The EMC3 modelling includes parallel and cross-field transports in a 3-D geometry of the magnetic field. The transport of bulk plasma and impurity along the magnetic field line is considered to be classical, while the cross-field transport perpendicular to the magnetic field line is assumed to be anomalous [28].

In the fluid approximation, the momentum balance equation of impurity ions along the magnetic field line is given as

$$m_z \frac{\partial V_{z\parallel}}{\partial t} = -\frac{1}{n_z}\frac{\partial T_i n_z}{\partial s} + m_z \frac{V_{i\parallel} - V_{z\parallel}}{\tau_{zi}} + ZeE_{\parallel} + 0.76Z^2\frac{\partial T_e}{\partial s} + 2.6Z^2\frac{\partial T_i}{\partial s}, \qquad (6.1)$$

where z and i denote the impurity with charge state Z and the bulk plasma ion, respectively. The notation s is the coordinate along the magnetic field line. The variables $V_{i\parallel}$, $V_{z\parallel}$, τ_s, m_z and $E_{\parallel}$ denote the parallel velocities of bulk plasma and impurity, impurity-ion collision time, impurity ion mass and parallel electric field, respectively. The values of T_z and T_i denote the temperatures of the impurity and the

bulk plasma ions, respectively, and $T_z = T_i$ is assumed in the equation. The inertia term shown in the left-hand side of the equation can be neglected due to a small value. The first term on the right-hand side of the equation shows the impurity pressure gradient force. The second and third terms are the force due to friction between the impurity and bulk plasma ions and the force due to the parallel electric field, respectively. The fourth and fifth terms on the right-hand side are the forces due to the electron and ion temperature gradients, respectively. It has been proved that the second and fifth terms in the right-hand side are dominant in the equation, which means the friction force and the ion thermal force become dominant in the force balance of impurity ions along the magnetic field line for the usual plasma parameters. The flow of the bulk plasma ions, $V_{i\|}$, is usually directed towards the downstream, i.e., from the plasma edge to the divertor plates, and the friction force moves the impurity ions to the divertor region. On the other hand, the temperature gradient, $\partial T_i/\partial s$, is, directed towards the upstream, i.e., from the divertor plates to the plasma edge, and the thermal force moves impurity ions to the upstream direction. Therefore, the impurity velocity, $V_{z\|}$, is a consequence of the competition between the friction and the ion thermal forces. If the friction force is more dominant than the thermal force, the impurity ion can be screened.

The cross-field transport is also important in the ergodic layer of LHD where the connection length of magnetic field lines is very long. In the EMC3 code the cross-field transport of bulk and impurity ions is assumed to be anomalous. Here, it is noted that the bulk ion in LHD is proton. The particle diffusion coefficient, $D_\perp$, and heat conduction coefficient, $\chi_\perp$, are determined for bulk plasmas by analyzing the edge density and temperature profiles measured with Thomson scattering diagnostic. Spatially constant values of $D_\perp$ and $\chi_\perp$ are used in the code. Although the cross-field impurity diffusion of impurity ions, $D_{Z\perp}$, may be different from bulk ions [30, 31], the impurity motion in the present modeling is simply smoothed out towards the perpendicular direction with $D_{Z\perp}$. The poloidal distribution of impurity line emissions is therefore more uniform when the $D_{Z\perp}$ is large. The $D_{Z\perp}$ different from $D_\perp$ is also used in the present analysis to reproduce the measured profile of impurity line emissions.

In the simulation for $R_{ax} = 3.75$ m configuration, $D_\perp = 0.2$ m^2/s and $\chi_\perp = 0.5$ m^2/s are used for bulk plasmas by analyzing edge electron density and temperature profiles shown in Fig. 6.8. The amount of impurity carbon is mainly dependent on the sputtering yield of the graphite divertor plates, C_{sput}. In the present study, the sputtering rate of $C_{sput} = 0.5\%$ has been used for the graphite divertor plate [30, 31]. Figure 6.9 shows the simulated 2-D distribution of CIII–CVI emissivity in the ergodic layer at horizontally elongated plasma cross section. It is clear that the CIII and CIV with low ionization energies, i.e., 48 eV for C^{2+} and 64 eV for C^{3+}, are mainly located near the outer boundary of the ergodic layer or in the vicinity of divertor legs, while the CV and

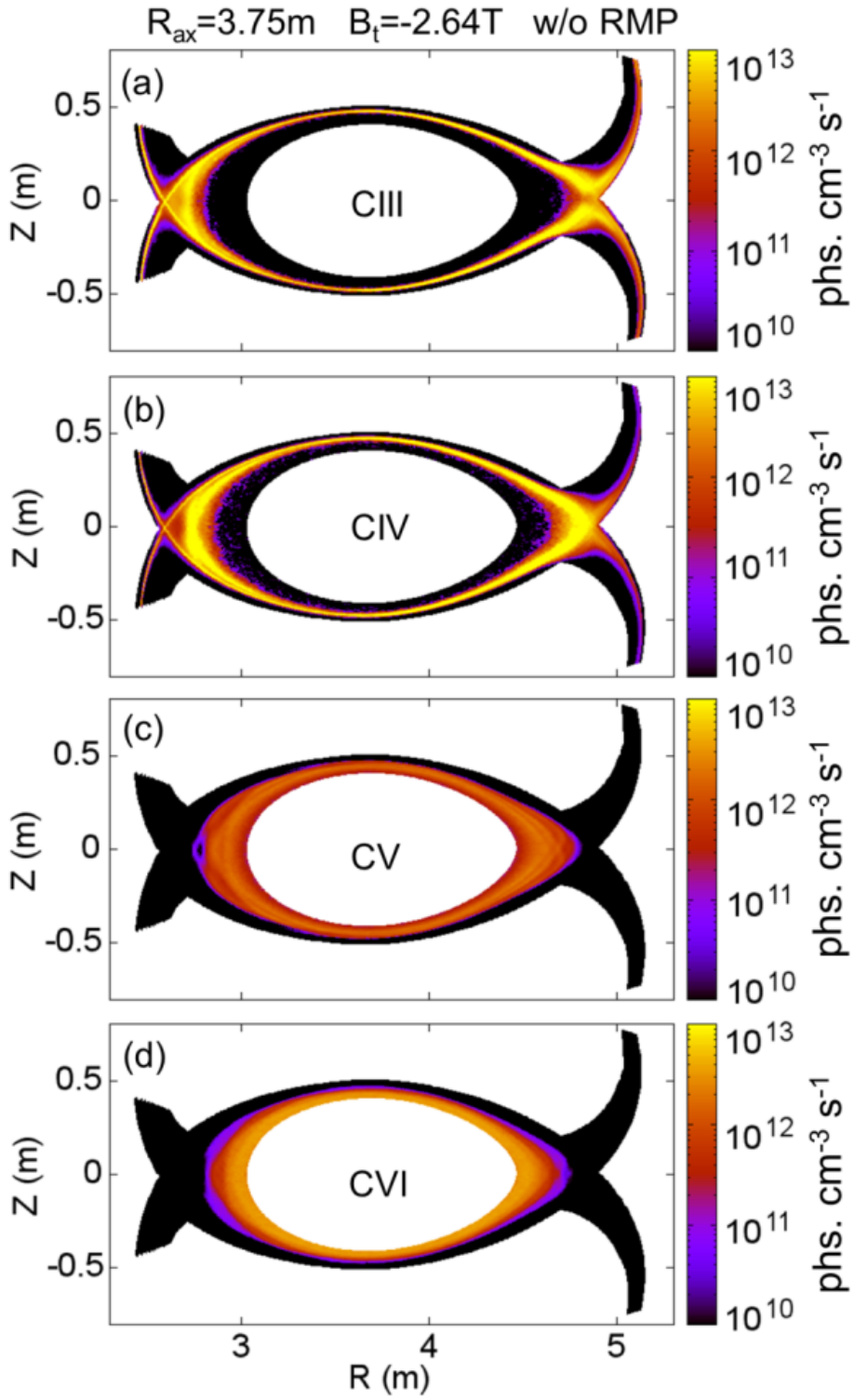

Fig. 6.9 Poloidal distributions of impurity emissivity in the ergodic layer calculated with EMC3-EIRENE for (a) CIII (386.203 Å), (b) CIV (312.42 Å), (c) CV (40.27 Å) and (d) CVI (33.73 Å) in discharges without RMP at R_{ax} = 3.75 m.

CVI are dominant inside the ergodic layer due to the high ionization energies, i.e., 392 eV for C^{4+} and 490 eV for C^{5+} [32]. Therefore, the poloidal distributions of CIII and CIV are entirely non-uniform thus enhancing the intensity in the vicinity of inner and outer X-points, whereas the CV and CVI intensities show a uniform poloidal distribution. Since the EMC3-EIRENE code is only applicable to the open magnetic field layer such as the ergodic layer in LHD or the scrape-off layer in tokamaks, the CVI emission inside the LCFS is not plotted in Fig. 6.9 (d) due to the absence of data. In addition, any up-down asymmetry is not observed in the simulation result at $\phi = 18°$ because the magnetic field structure in the ergodic layer is basically identical between the upper and lower edge regions.

6.4.3 Vertical profiles of carbon line emissions

The vertical profile of CIV to CVI is measured at the density and temperature flat-top phase of t = 6.0 s shown in Fig. 6.7 for three configurations, i.e., without RMP, 6-O island and 7-O island. The results are plotted in Figs. 6.10 (d), (e) and (f) for CIV, CV and CVI, respectively. The $\iota/2\pi$ profiles for the three configurations are also plotted in Figs. 6.10 (a), (b) and (c). The positions of LCFS and island O-point are indicated with vertical arrow at the top of figures and vertical dashed line, respectively. Since the island O-point is located in the upper position at #10-O toroidal section for both the 6-O and 7-O islands [see Figs. 6.4 (b) and (c)], the local flattening of $\iota/2\pi$ appears in the top of the vertical profile. The radial range of m/n = 1/1 island is denoted with shaded area. The radial width of the m/n = 1/1 island is roughly 8 cm at the top edge O-point as seen in Figs. 6.10 (b) and (c). When the island O-point is located at the edge X-point, the radial width becomes bigger as seen in the T_e profile of Fig. 6.8 (b).

In the general discharge without RMP, the CIV profile is poloidally non-uniform and vertically asymmetric as shown in Fig. 6.10 (d). In contrast to this, the CVI profile is roughly symmetric as shown in Fig. 6.10 (e). The edge peaks in CIV at $Z \sim \pm 500$ mm and CV at $Z \sim \pm 440$ mm are due to a long integration effect along the observation chord in the thin CIV and CV emission contours [see Figs. 6.9 (b) and (c)]. In addition, the CIV is also enhanced in the range of $-300 \leq Z \leq 300$ mm in the vicinity of inboard or outboard edge X-points, while the CV and CVI profiles seem to be flat. This can be well explained by the simulation (see Fig. 6.9). Further, the emission from upper half at $-500 \leq Z \leq 0$ mm tends to have grater intensity compared to the emission from lower half at $0 \leq Z \leq 500$ mm. In particular, this is clear in the CIV profile, suggesting an up-down asymmetry in the edge impurity radiation.

When the RMP is supplied, the CIV and CV profiles slightly change in the upper half structure. This is reasonable because the T_e and n_e profiles are unchanged in

the ergodic layer outside the LCFS (see Fig. 6.8). Therefore, the m/n = 1/1 island has little influence on the CIV and CV profiles in the R_{ax} = 3.75 m configuration. On the other hand, the CVI profile in Fig. 6.10 (f) indicates a significant change when the RMP is supplied. The CVI intensity is clearly reduced for both the 6-O and 7-O island cases. When the RMP is supplied, the impurities intrinsically existing in LHD plasmas such as carbon and iron are always decreased in the plasma core despite the unchanged influx. The reason is therefore due to the enhanced edge impurity screening [19]. It is also noticed that the CVI intensity increases at the top O-point near Z = 400 mm where the island O-point exists. This seems to be an effect of edge temperature flattening shown in Fig. 6.8 (b). Here, it is concluded that the m/n = 1/1 island at R_{ax} = 3.75 m configuration can only change the CVI distribution located near the island and the effect of m/n = 1/1 island on the CIV and CV distributions is entirely small.

The up-down asymmetry is slightly enhanced when the B_t is in the counter-clock wise direction, e.g., B_t = –2.64 T [15]. A comparison of CIV–CVI vertical profiles is shown in Fig. 6.11 for clockwise (solid lines) and counter-clockwise (dashed lines) B_t directions. It is clear that the up-down asymmetry is emphasized in the case of the counter-clockwise direction, in particular, for CV. Although the physical mechanism is unclear at present, this asymmetry may suggest an importance of the particle drift. Since the edge peak position indicates the radial location of carbon ions, we understand that both C^{3+} and C^{4+} ions are located outside the $\iota/2\pi = 1$ position and the C^{5+} ions are located very close to the $\iota/2\pi = 1$ position.

The CIV–CVI vertical profiles are also analyzed with EMC3-EIRINE, as plotted with dotted line in Fig. 6.11. The intensity profiles are normalized to the measurement at Z = 0 mm. Since the EUV_Long2 spectrometer is placed at 9300mm away from the LHD plasma and 500m above the midplane, the observation chords are vertically inclined a little. Then, the simulation with experimental geometry does not exactly show the vertical symmetry. Although the effect of the inclined observation chord on the profile is very small, it typically appears in the simulation of CIV profile at Z ~ ±400 mm because the CIV is located at the outer boundary of the ergodic layer. The simulation can well explain the CIV profile in clockwise B_t direction, while that in counter-clockwise direction is somewhat different in both edge regions of the top and bottom. In the simulation the cross-field impurity diffusion coefficient of $D_{Z\perp}$ = 1.0 m^2/s, of which the value is five times larger than the bulk ions, is used for carbon ions to explain the experiment. In the CVI simulation the emission inside the LCFS is not included in the emissivity profile. The CVI emission near the edge O-point in the ergodic layer, which created the edge peaks appeared at Z = ±400 mm, is unnecessarily enhanced. In practice, the CVI emission near the edge X-point inside the LCFS is strong, and then the CVI profile becomes roughly flat as seen in the experiment. The

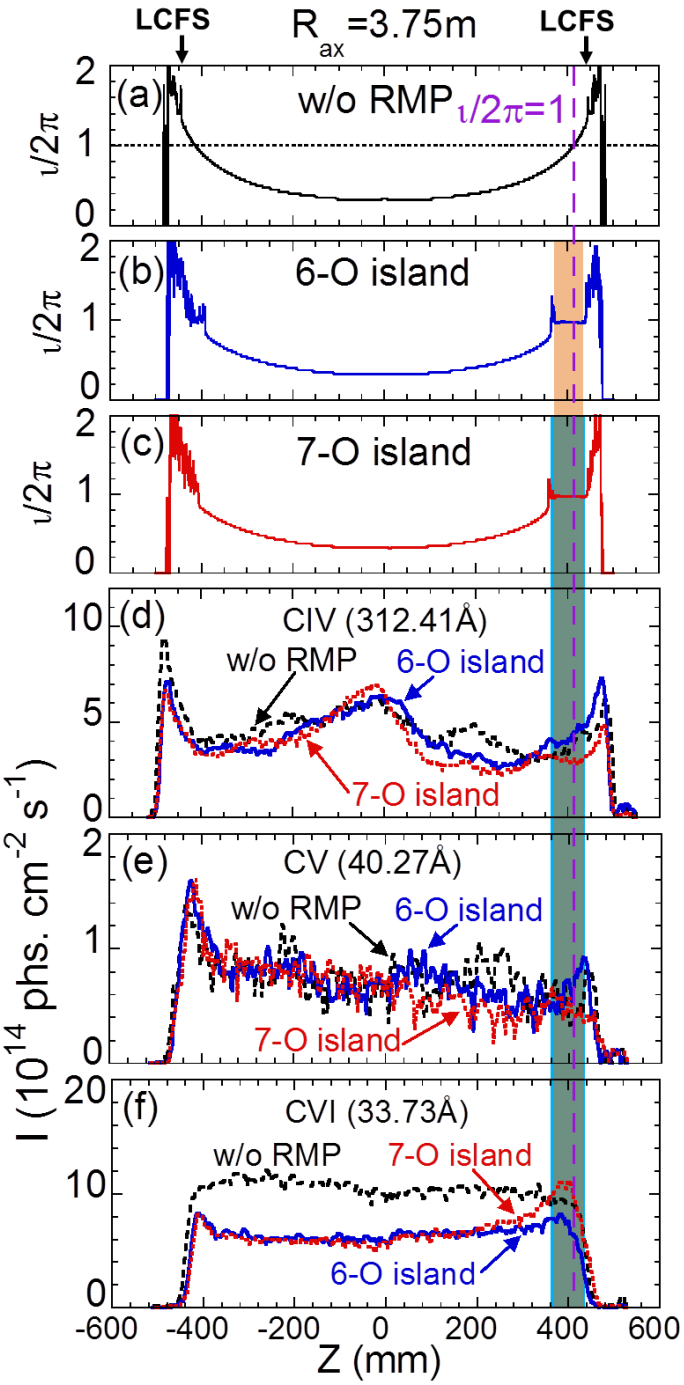

Fig. 6.10 ι/2π profiles (a) without RMP, (b) with 6-O island, (c) with 7-O island and vertical profiles of (d) CIV (312.42 Å), (e) CV (40.27 Å) and (f) CVI (33.73 Å) at #10-O toroidal location in discharges at R_{ax} = 3.75 m without RMP (dashed line), with 6-O island (solid line) and with 7-O island (dotted line). Radial locations of LCFS and ι/2π = 1 are indicated with vertical arrows and dashed line, respectively. The radial distributions of m/n =1/1 island are indicated with shaded areas with different colors for 6-O (brown) and 7-O island (sky blue).

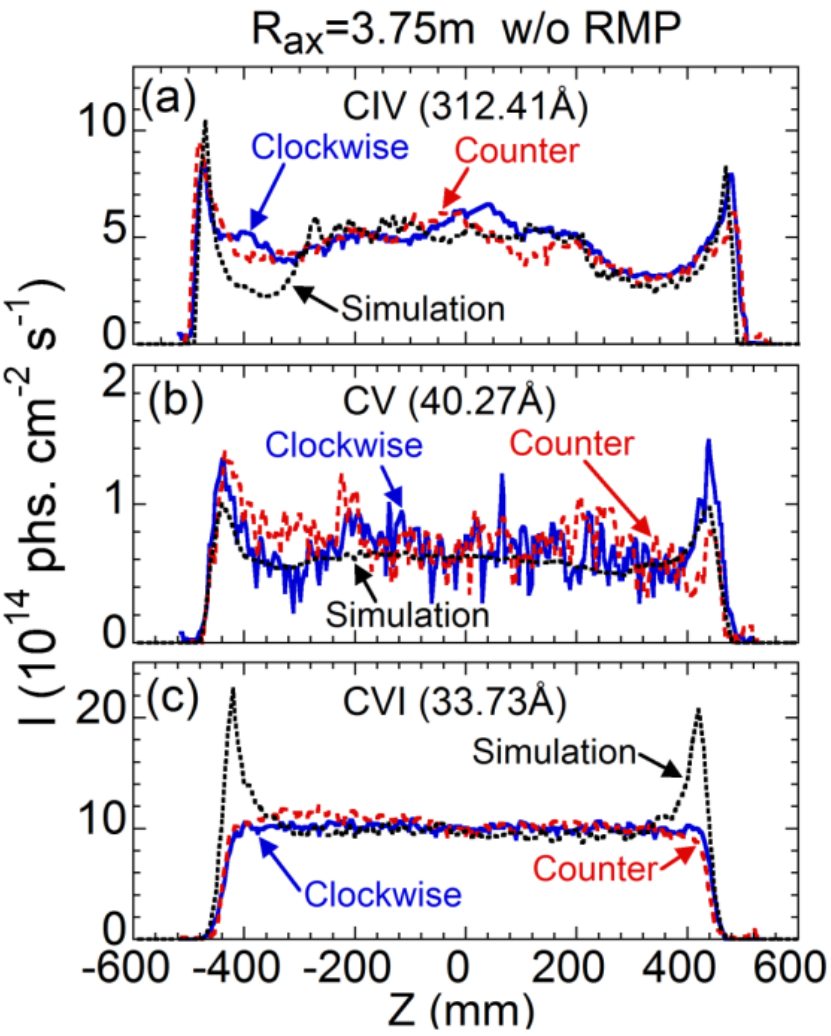

Fig. 6.11 Vertical profiles of (a) CIV (312.42 Å), (b) CV (40.27 Å) and (c) CVI (33.73 Å) measured at #10-O toroidal location in discharges at R_{ax} = 3.75 m with toroidal magnetic field in clockwise (B_t = 2.64 T: solid line) and counter-clockwise (B_t = –2.64 T: dashed line) directions and simulated with EMC3-EIRENE (dotted line).

CVI emissivity is also slightly stronger at the lower half of the plasma in the counter-clockwise B_t direction, while the profile in the clockwise direction is almost flat.

6.4.4 2-D distribution of carbon line emissions

In order to study the effect of m/n = 1/1 island on the carbon emission in greater detail, the 2-D distribution of CIV–CVI is measured in the steady phase of NBI discharges at R_{ax} = 3.75 m. The result is shown in Fig. 6.12.

In general discharges without RMP, the 2-D CIV distribution shown in Fig. 6.12 (a) indicates that the emission is dominant at the top and bottom edges and in the vicinity of inboard and outboard X-points. The trajectories of inboard and outboard X-points are indicated in Fig. 6.12 (a) with dashed-dotted and long-dashed lines, respectively. The schematic view in Fig. 6.5 (b) and the simulation in Fig 6.9 (b) are also helpful for understanding the Fig. 6.12 (a). In contrast to it, the CV and CVI distributions shown in Figs. 6.12 (d) and (g) are almost uniform except for the bottom edge. The up-down asymmetry brought by the effect of counter-clockwise toroidal magnetic field is also clearly observed in the 2-D distributions of CIV–CVI.

The 2-D distribution of carbon emissions is also simulated with EMC3-EIRENE code [30,31]. The 2-D plot of the CIV simulation shown in Fig. 6.13 (a) indicates emission enhancements not only in the top and bottom edges but also along several trajectories parallel to the inner and outer X-points. The simulated result in Fig. 6.13 (a) with $D_{Z\perp}$ = 0.2 m^2/s is considerably different from the experimental result in Fig. 6.12 (a), while the intensity is in the same level. The CV simulation in Fig. 6.13 (c) also indicates a different structure from the experiment in Fig. 6.12 (d). To explain the experimental data, then, a larger impurity diffusion coefficient is adopted in the simulation. The results with $D_{Z\perp}$ = 1.0 m^2/s are shown in Figs. 6.13 (b) and (d) for CIV and CV, respectively. The sharp trajectories related to edge X-points seen in Figs. 6.13 (a) and (c) almost disappear from Figs. 6.13 (b) and (d) and the simulated results with large $D_{Z\perp}$ are relatively in good agreement with the experimental results in Figs. 6.12 (a) and (d). However, there still remain unclear points, in particular, in the angle of X-point trajectories between the simulation and experiment. In the present simulation code, at least, effects of plasma pressure on the magnetic field structure in the ergodic layer and particle motion on the impurity transport such as ∇B drift are not included. An improvement in the simulation code is necessary for further discussions. The 2-D distribution of CVI shown in Fig. 6.13 (c) is enhanced near the top and bottom where the chord integration length in the emission is long, suggesting a clear difference from the experiment in Fig. 6.12 (g). This difference is also caused by the absence in the simulation inside the LCFS.

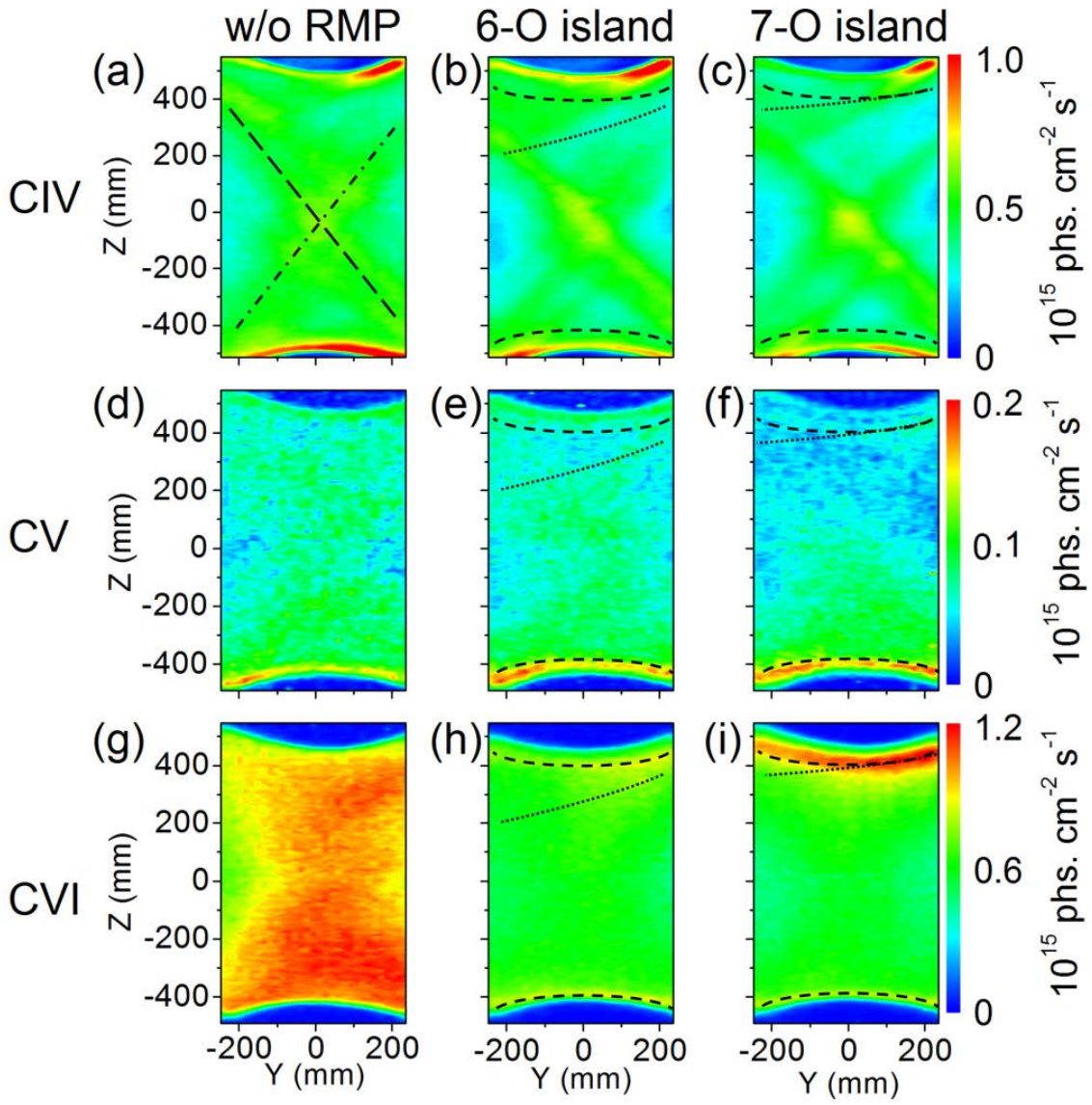

Fig. 6.12 2-D distributions at R_{ax} = 3.75 m of CIV (312.42 Å) in discharges (a) without RMP, (b) with 6-O island and (c) with 7-O island, CV (40.27 Å) in discharges (d) without RMP, (e) with 6-O island and (f) with 7-O island and CVI (33.73 Å) in discharges (g) without RMP and (h) with 6-O island. Trajectories of outboard X-point, inboard X-point and island O-point are indicated with long dashed, dotted-dashed and dashed lines, respectively. The radial location of $\iota/2\pi$ = 1 profile is indicated with dashed lines in each figure.

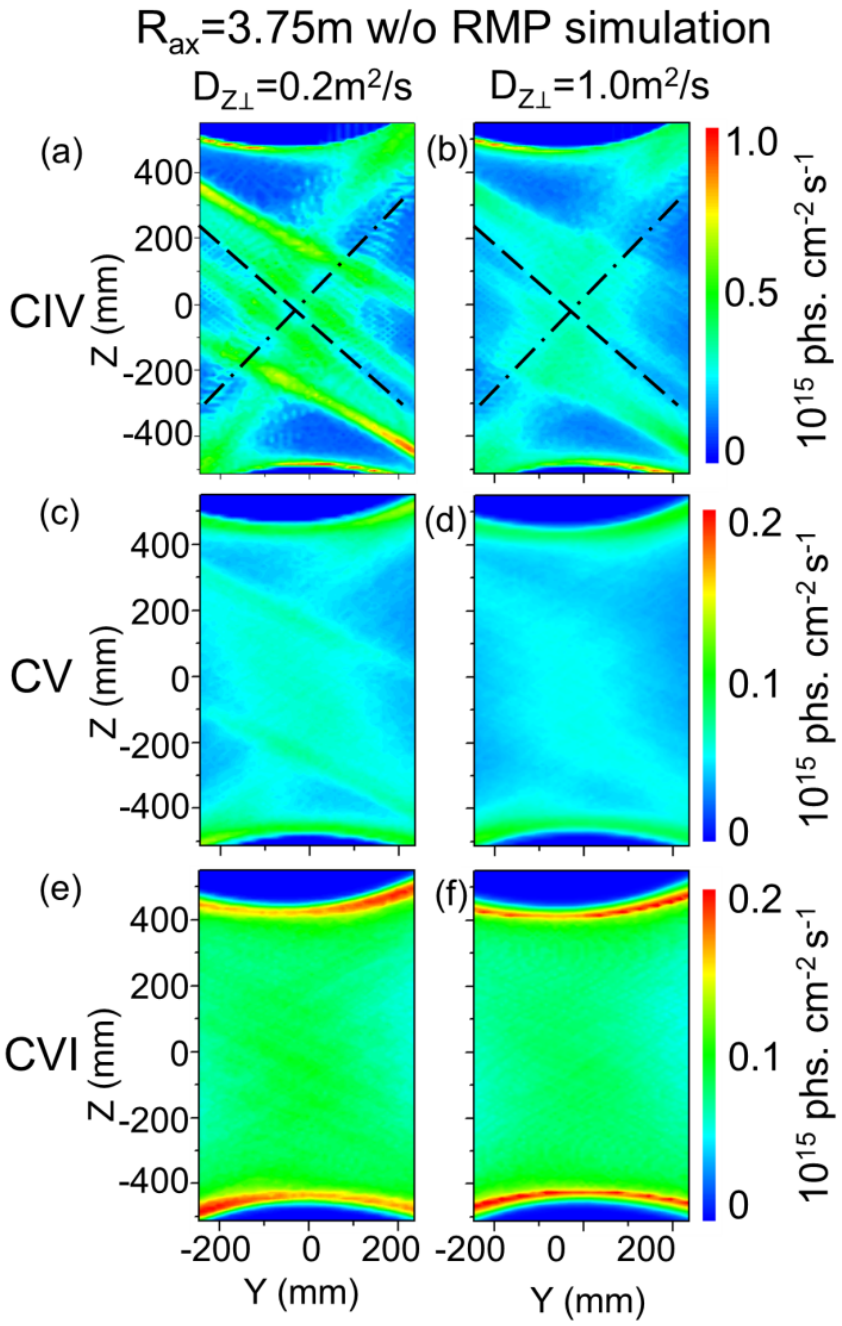

Fig. 6.13 2-D emissivity distributions simulated with EMC3-EIRENE in R_{ax} = 3.75 m configuration without RMP for (a) CIV (312.42 Å), (c) CV (40.27 Å) and (e) CVI (33.73 Å) at impurity diffusion coefficient of $D_{Z\perp}$ = 0.2 m^2/s and (b) CIV, (d) CV and (f) CVI at $D_{Z\perp}$ = 1.0 m^2/s. Trajectories of outboard and inboard X-point are indicated with long dashed and dotted-dashed lines, respectively.

Even if the RMP is supplied, the CIV and CV distributions do not obviously change, as shown in Figs. 6.12 (b), (c), (e) and (f), whereas a significant change is observed in the 2-D distribution of CVI, as shown in Figs. 6.12 (h) and (j). In the 6-O island case shown in Fig. 6.12 (h) the CVI is slightly enhanced at the top and bottom edges. In the 7-O island case of Fig. 6.12 (i), however, the CVI is clearly strong at the top edge. The trajectory of the island O-point is indicated in the figures with dotted line and the radial location of $\iota/2\pi = 1$ is indicated with dashed line for both the 6-O and 7-O island cases. Then, we can understand that the CVI intensity is basically enhanced in the vicinity of island O-point seeing Figs. 6.4 (c) and 6.12 (i).

6.5 Impurity carbon radiation at R_{ax} = 3.90 m configuration with island outside LCFS

6.5.1 Discharge waveform and radial profiles of n_e and T_e

Vertical profiles and 2-D distributions of CIII–CVI are also studied in attached and detached plasmas at R_{ax} = 3.90 m configuration. Figure 6.14 shows typical waveform of NBI discharges without (solid line) and with (dashed line) RMP at R_{ax} = 3.90 m and B_t = 2.54 T. The discharge initiated with ECH at t = 3.0 s is maintained with n-NBIs for 5 s at t = 3.3 – 8.3 s. In the discharge without RMP, the additional gas feed is not utilized to avoid the radiation collapse at high density range [12]. The line-averaged density and central electron temperature roughly keep constant, i.e., $n_e \sim 5 \times 10^{13}$ cm^{-3} and $T_{e0} \sim 1.2$ keV, during 3.5s from 4.5 to 8.0s at which the 2-D distribution is observed. The ion saturation current, I_{is}, measured with Langmuir probe array embedded in the divertor plates at #6-O is constant at I_{is} = 0.17 A during the discharge. The effective plasma radius denoted with a_{99} shown in Fig. 6.14 (f) is also constant at r_{eff} = 0.55 m during the discharge, indicating unchanged plasma volume. Here, the value of a_{99} often used in LHD is defined by a plasma radius in which 99% of the total plasma energy is confined. The effective plasma radius is calculated based on the T_e and n_e profiles from Thomson scattering diagnostic.

When the RMP is supplied, and the electron density reaches a density threshold, the discharge condition drastically changes to an entire different state. As shown in Fig. 6.14 (e), the ion saturated current suddenly decreases by 60% at t = 5.1 s denoted with vertical dotted line at which the density reaches the threshold and keeps the low value until the end of discharge. This current behavior indicates a specific feature of the plasma detachment. In the present discharge the density threshold is $n_e \sim 5 \times 10^{13}$ cm^{-3}, while it slightly depends on the NBI input power. After the transition to the detachment plasma, the electron density continuously to increase until t = 6.3 s and saturates at $n_e \sim$

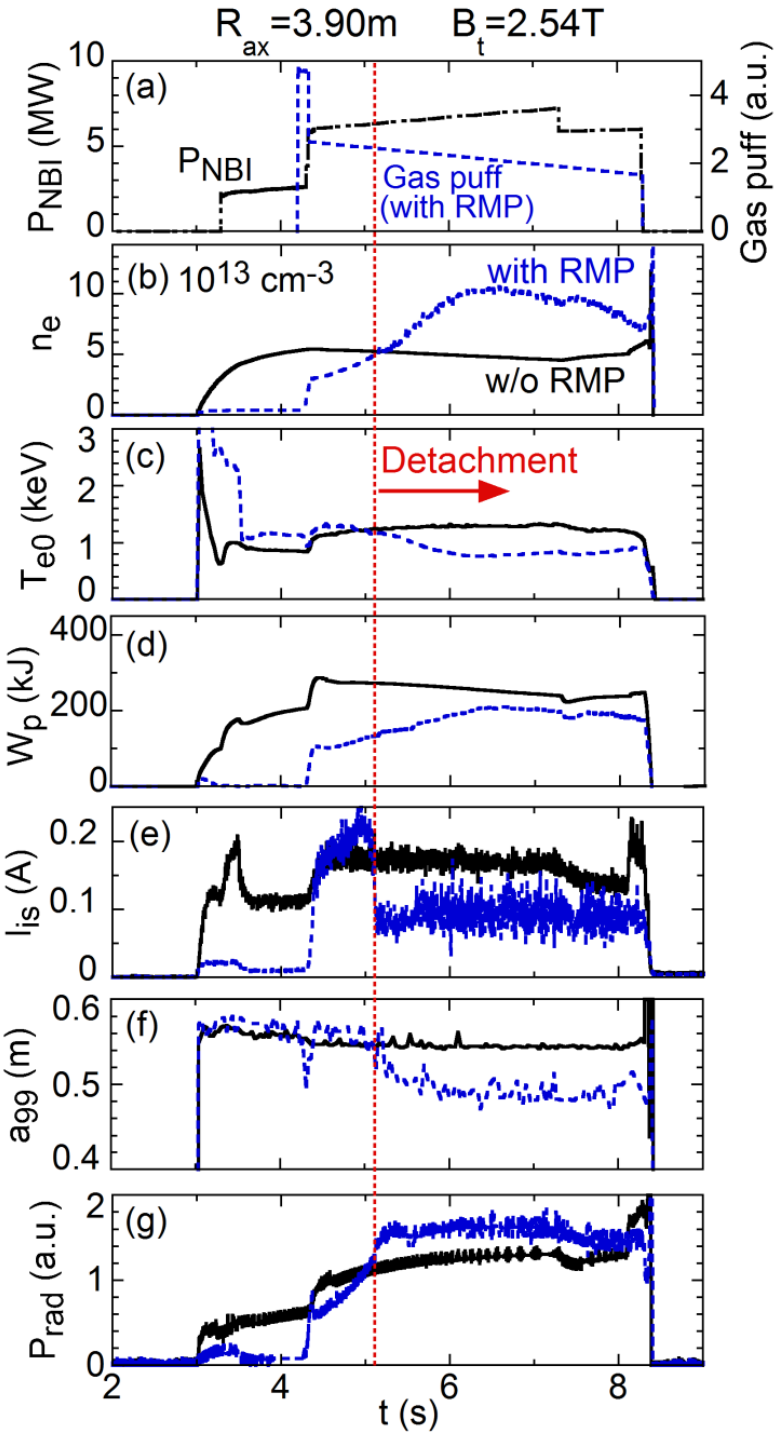

Fig. 6.14 Time behaviors of (a) NBI port-through power and gas puffing, (b) line-averaged electron density, (c) central electron temperature, (d) stored energy, (e) ion saturated current, (f) effective plasma radius and (g) radiation loss power in discharges at R_{ax} = 3.90 m without RMP (solid line) and with RMP (dashed line). The timing of detachment transition is indicated with vertical dotted line.

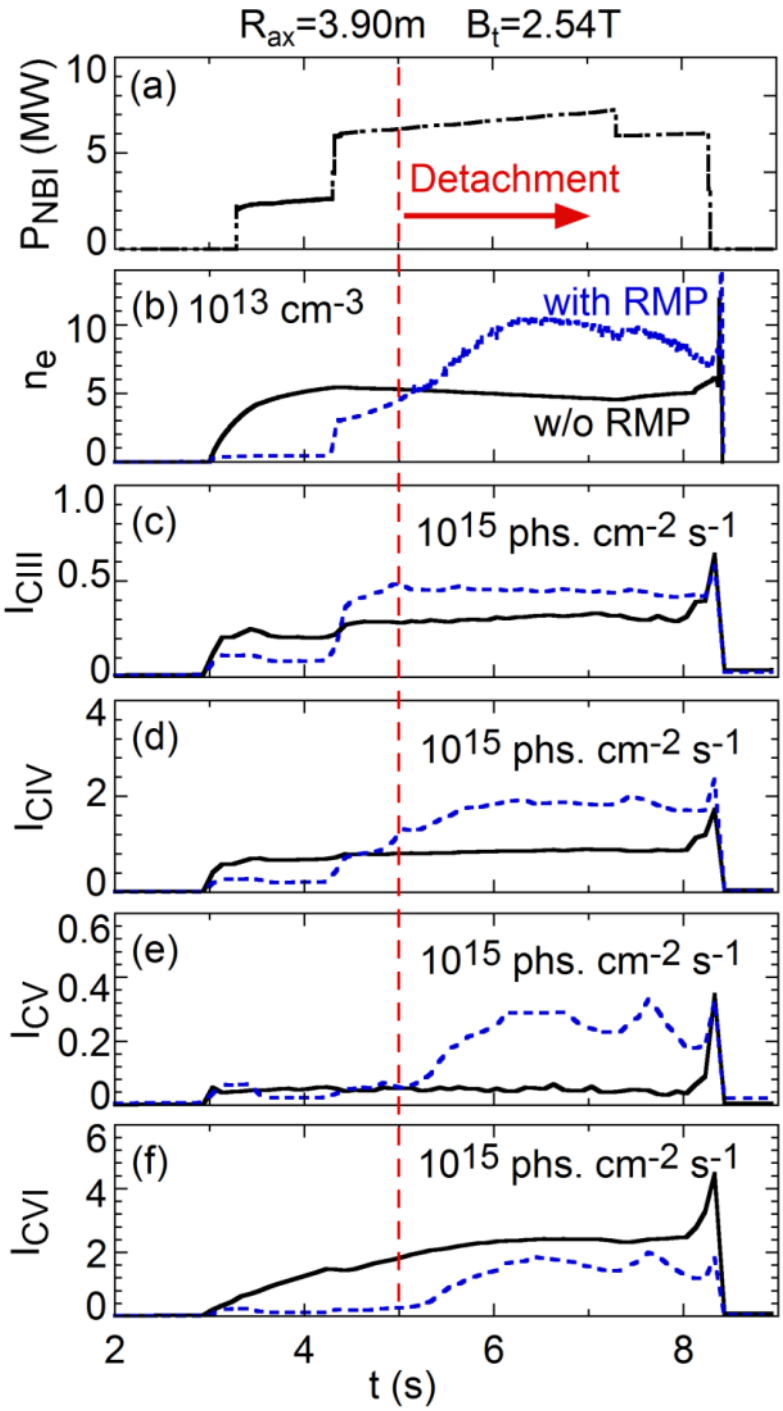

Fig. 6.15 Time behaviors of (a) NBI port-through power, (b) line-averaged electron density and intensities of (c) CIII (386.203 Å), (d) CIV (384.174 Å), (e) CV (40.27 Å) and (f) CVI (33.73 Å) in discharges at R_{ax} = 3.90 m without (solid line) and with RMP (dashed line).

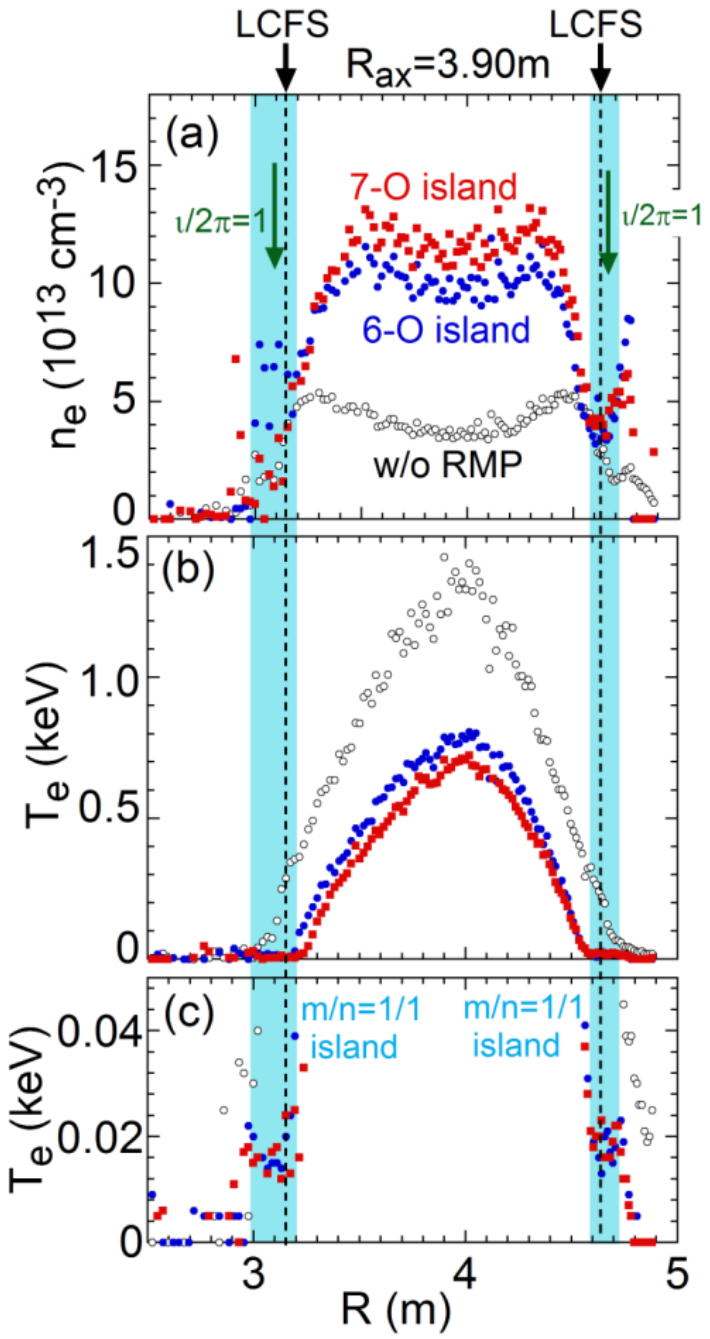

Fig. 6.16 Radial profiles of (a) n_e, (b) T_e and (c) enlarged T_e in discharges at R_{ax} = 3.90 m without RMP (open circles), with 6-O island (solid circles) and with 7-O island (solid squares). Radial locations of LCFS and $\iota/2\pi = 1$ are indicated with dashed lines and vertical arrows, respectively. Radial range of m/n =1/1 island is denoted with shaded area.

12×10^{13} cm^{-3}. The central electron temperature starts to decrease after the detachment transition due to the density increase and finally stays at $T_{e0} \sim 0.8$ keV. In contrast, the stored energy still continues to increase even after the detachment transition and takes a similar temporal behavior to the density. Another specific feature at the detachment transition appears in the effective plasma radius. The effective plasma radius of r_{eff} = 0.55 m starts to decrease after the detachment transition. It reaches r_{eff} = 0.48 m and keeps the constant plasma radius basically until the end of discharge. The radiation power is also increased and constantly kept at a considerably high level during the plasma detachment phase. It should be noted that absolute value of the total radiation power still has not been obtained due to a problem of calibration including 3-D radiation structure. The time behaviors of carbon line emissions of CIII (386.203 Å), CIV (384.174 Å), CV (40.27 Å) and CVI (33.73 Å) are shown in Fig. 6.15. The CIII–CV emissions significantly increase during the detachment phase, indicating the enhancement of edge radiation. However, the CVI emission clearly decreases during the detachment phase suggesting an enhancement of the impurity screening effect by the additional RMP field.

The radial profiles of n_e and T_e measured at t = 7.0 s in Fig. 6.14 are shown in Fig. 6.16 for three different discharges, i.e. without RMP (open circles), 6-O island with detachment (solid circles) and 7-O island with detachment (solid squares). The radial positions of $\iota/2\pi = 1$ and LCFS are denoted with vertical arrows and vertical dashed lines, respectively. The radial location of m/n = 1/1 island is denoted with shaded area. The density in the plasma core largely increases for both the 6-O and 7-O island cases after the detachment transition, of which the densities are a few times larger than the density in discharges without RMP. On the other hand, the temperature in the plasma core at the detachment phase is much lower than that in the discharge without RMP.

It is very interesting to examine the effect of the island in the density and temperature profiles. One of the specific features is observed in the edge density jump. The density increases in the vicinity of the island. This phenomenon also appears in the density profile at R_{ax} = 3.75 m configuration shown in Fig. 6.8 (a). The effect of the island also appears in the edge temperature profile. Figure 6.16 (c) shows the detailed T_e profile in the edge region. The C^{2+} and C^{3+} ions stay in the vicinity of the flat T_e region. A flattened edge temperature ranging in $10 \leq T_e \leq 20$ eV is clearly seen near the island position. Although the temperature profile at 6-O island is slightly broadened compared to the profile at 7-O island, this seems to be an effect of different deformation in the magnetic surface due to the plasma pressure.

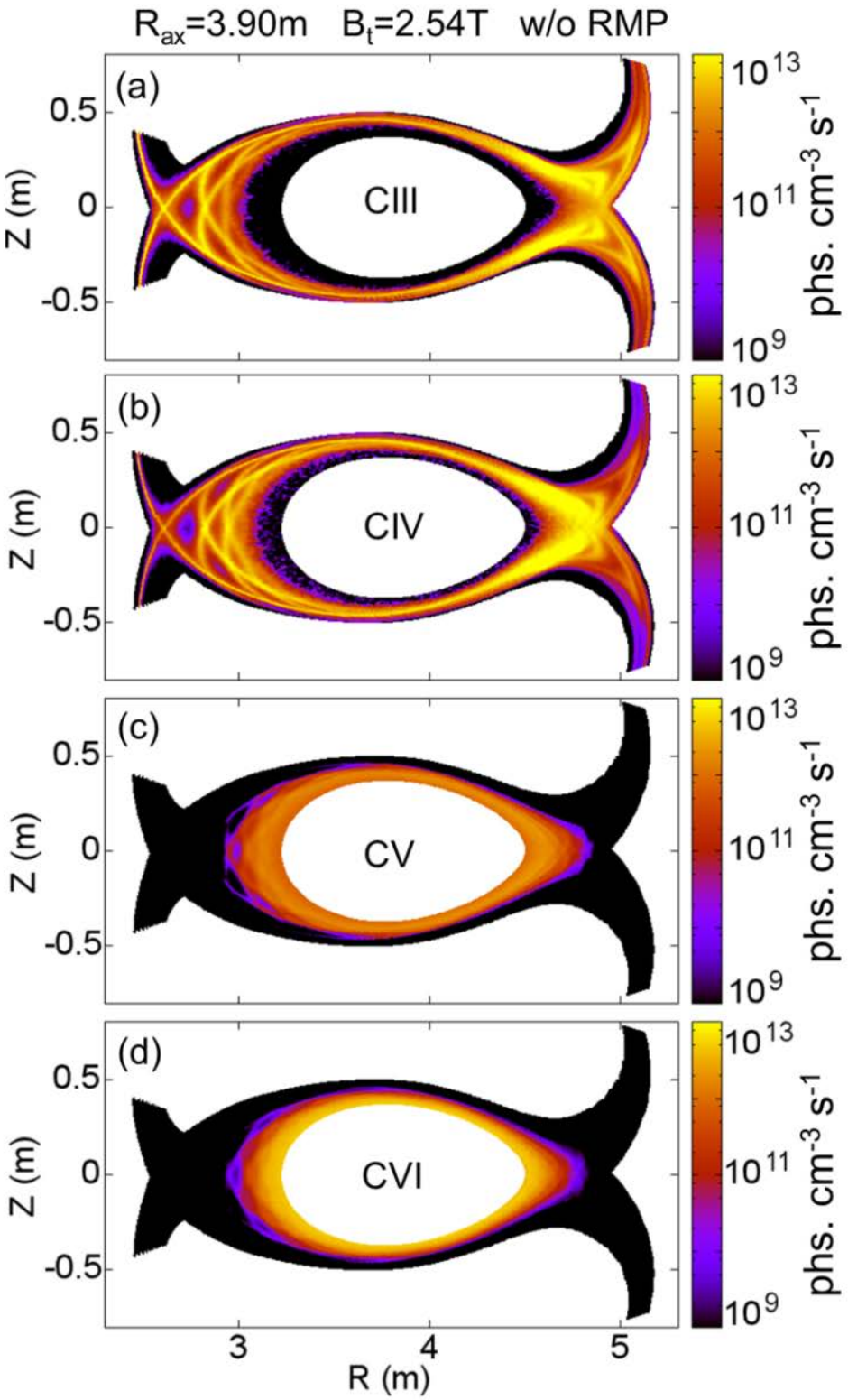

Fig. 6.17 Poloidal distributions of impurity emissivity in the ergodic layer simulated with EMC3-EIRENE for (a) CIII (386.203 Å), (b) CIV (384.174 Å), (c) CV (40.27 Å) and (d) CVI (33.73 Å) in R_{ax} = 3.90 m configuration without RMP.

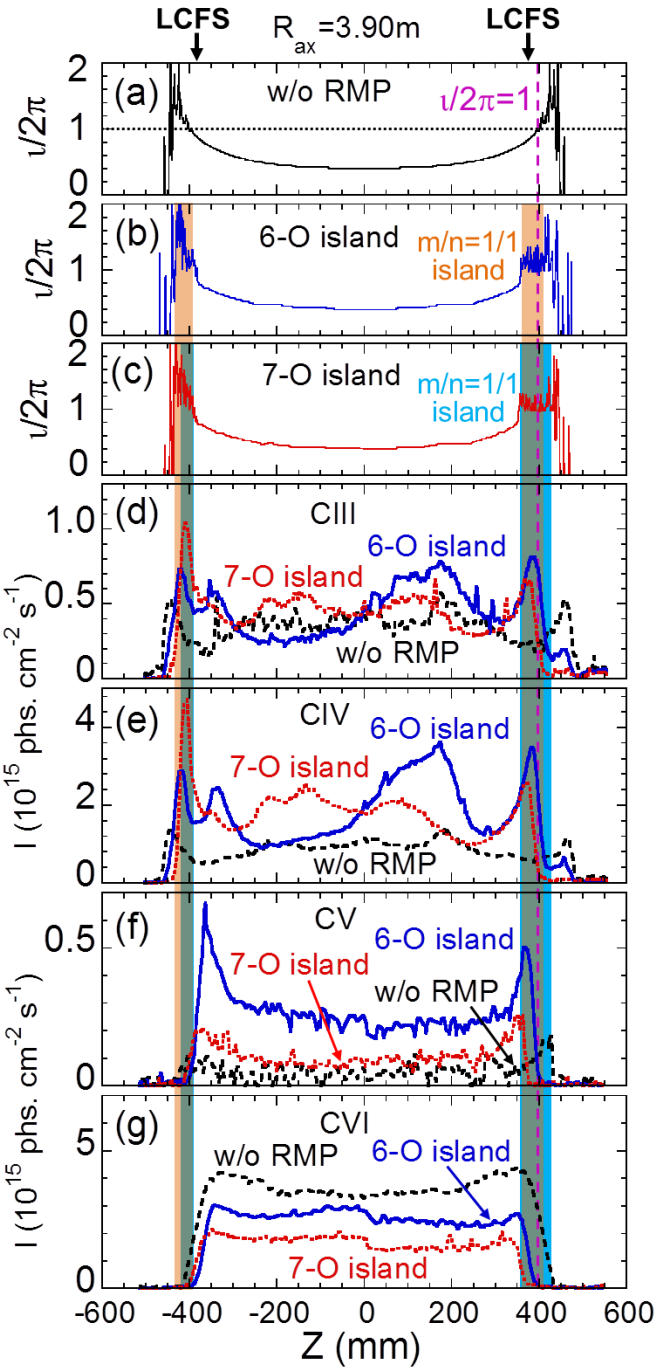

Fig.6.18 ι/2π profiles (a) without RMP, (b) with 6-O island, (c) 7-O island and vertical profiles of (d) CIII (386.203 Å), (e) CIV (384.174 Å), (f) CV (40.27 Å) and (g) CVI (33.73 Å) at #10-O toroidal location in discharges at R_{ax} = 3.90 m without RMP (dashed line), with 6-O island (solid line) and with 7-O island (dotted line). Radial locations of LCFS and ι/2π = 1 are indicated with vertical arrows and dashed line, respectively. The radial ranges of m/n = 1/1 island are indicated by shaded area with different colors for 6-O (brown) and 7-O island (sky blue).

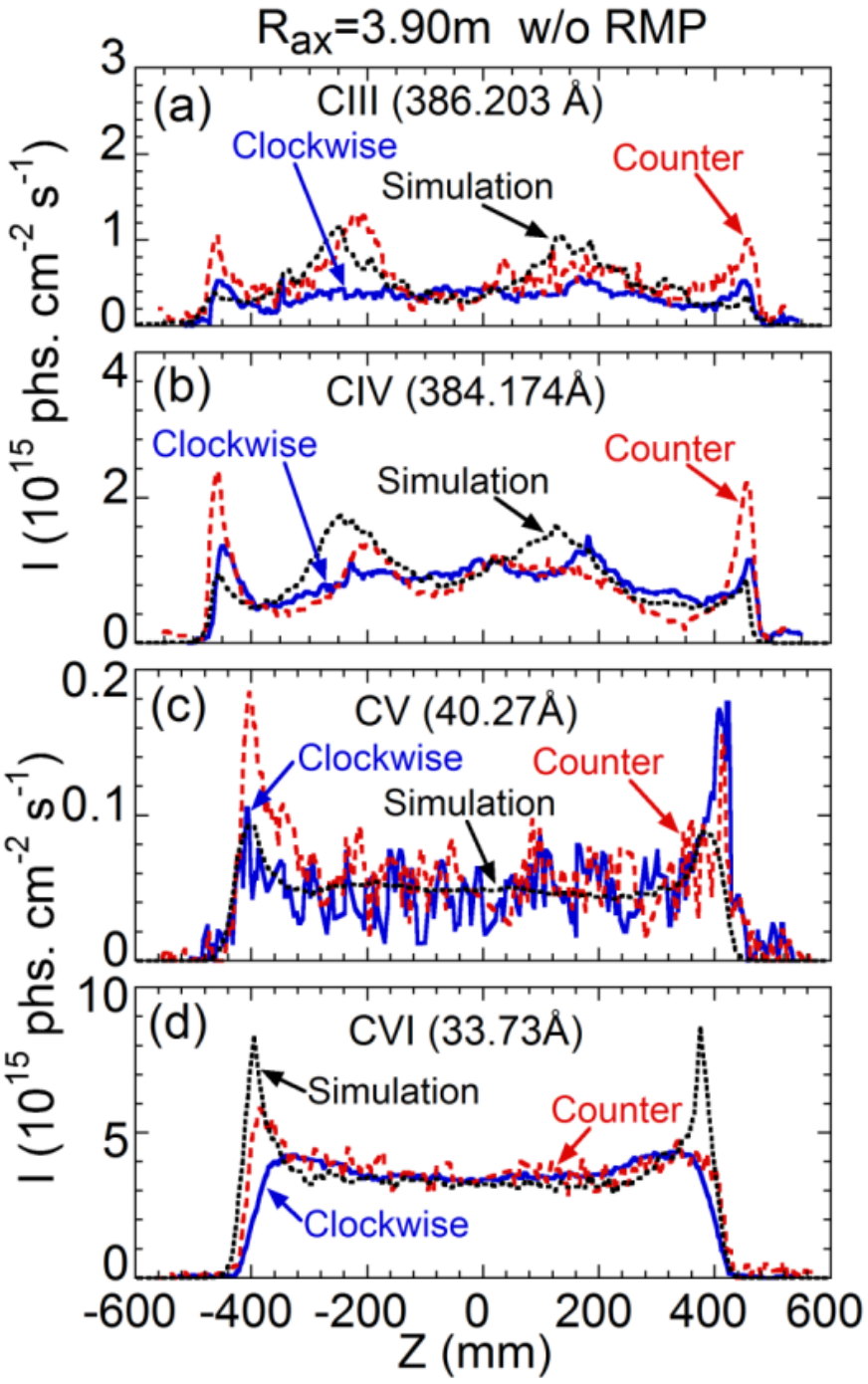

Fig. 6.19 Vertical profiles of (a) CIII (386.203 Å), (b) CIV (384.174 Å), (c) CV (40.27 Å) and (d) CVI (33.73 Å) measured at #10-O toroidal location in discharges at R_{ax} = 3.90 m with toroidal magnetic field in clockwise (B_t = 2.54 T: solid line) and counter-clockwise (B_t = –2.54 T: dashed line) directions and simulated with EMC3-EIRENE (dotted line).

6.5.2 Vertical profiles of carbon line emissions

The emissivity distribution of CIII–VI is simulated with EMC3-EIRENE for R_{ax} = 3.90 m configuration as well as the R_{ax} = 3.75 m case. The $D_\perp$ and $\chi_\perp$ are also determined by analyzing the edge electron density and temperature profiles shown in Fig. 6.16, i.e., $D_\perp$ = 0.2 m^2/s and $\chi_\perp$= 0.6 m^2/s. The impurity diffusion coefficient of $D_{Z\perp}$ = 4.0 m^2/s is used for carbon ions at all charge states in R_{ax} = 3.90 m. The reason is described below. The simulated result shown in Fig. 6.17 is closely similar to the previous result in Fig. 6.9, i.e., non-uniform CIII and CIV emissions located near the outer boundary in the ergodic layer and uniform CV and CVI emissions located in the vicinity of LCFS. The simulation of CIII and CIV emissivity shown in Figs. 6.17 (a) and (b) suggests a detailed structure in the vicinity of inboard and outboard edge X-points reflecting the complicated magnetic field structure at R_{ax} = 3.90 m in the region of inboard and outboard X-points. Comparing Figs. 6.17 (a) and (b) with Fig. 6.1 (c), it is clear that the CIII and CIV emissions are dominant in the region where the connection length ranges in $50 \leq L_c \leq 250$ m. Since the magnetic field lines in R_{ax}=3.90m configuration are dominantly connected to the divertor plates through the outboard X-point, the CIII and CIV emissions are stronger in the vicinity of the outboard X-point [see Fig. 6.1 (c)].

The vertical profiles of $\iota/2\pi$ and CIII–CVI at R_{ax} = 3.90 m are shown in Fig. 6.18 for attached plasma without RMP and detached plasmas with 6-O and 7-O islands. The CIII–CVI profiles at t = 7.0 s in Fig. 6.14 are plotted in Figs. 6.18 (d)–(g). The radial position of $\iota/2\pi$ = 1 indicated with dashed line in R_{ax} = 3.90 m configuration is located just outside the LCFS denoted with vertical arrows. A local flattening of the $\iota/2\pi$ profile appearing near $\iota/2\pi$ = 1 position is still visible for both the 6-O and 7-O islands. The radial range of the $\iota/2\pi$ profile flattening is also indicated with shaded area.

Since the ergodic layer outside LCFS is thick in R_{ax} = 3.90 m configuration, the plasma volume with low temperatures is large. The CIII emission can be then also measured with sufficient intensity in R_{ax} = 3.90 m as shown in Fig. 6.16 (d), while the CIV-VI emissions are always strong as shown in Fig. 6.18 (e)–(g). The vertical profiles of CIII–CV in attached plasmas without RMP denoted with dashed line have a clear peak near the top and bottom edges as well as the result of R_{ax} = 3.75 m, while the CVI in Fig. 6.18 (g) with dashed line has no such a peak. The CIII and CIV profiles also have an enhanced intensity in the vicinity of inboard or outboard side X-points at $-300 \leq Z \leq 300$ mm. The up-down asymmetry is not observed for the profiles of CV and CVI because the toroidal magnetic field of the discharge is in clockwise direction, i.e., B_t = 2.54 T.

When the plasma detachment occurs by supplying the RMP field, the profile of CIII–CVI completely changes due to the formation of m/n = 1/1 magnetic island and modification of stochastic magnetic field lines in the ergodic layer. For both the 6-O and 7-O island cases a new edge peak appears in the CIII and CIV profiles at the island location near Z = ±400 mm, while the original edge peak still remains at Z ~ 420 mm. Furthermore, the CIII and CIV emissions are also enhanced in the vicinity of edge X-points at $-400 \leq Z \leq -250$ mm for the 6-O island case and at $-300 \leq Z \leq 300$ mm for both the 6-O or 7-O island cases. On the other hand, the CV radially moves inside the plasma at the detachment phase with keeping the same vertical profile shape. This change is basically caused by the change in the T_e profile shown in Fig. 6.16 (b).

It is already known that the CIII and CVI are localized in the temperature range of T_e = 15–20 eV [33]. The flattened electron temperature at the island location also ranges in T_e = 10–20 eV in the detachment phase [see Fig. 6.16 (b)], of which the result is also seen in Ref. [12]. This is a main reason why the CIII and CIV intensities are increased at the detachment phase. The intensity of CV is also stronger during the detachment phase as well as the CIII and CIV intensities, while the intensity of CVI decreases. This indicates an enhancement of the impurity screening effect similar to the R_{ax} = 3.75 m case. It is therefore concluded that the CIII–CV emissions located near the island are selectively enhanced by the effect of supplied RMP field, whereas the CVI emission decreases.

The vertical profiles of CIII–CVI measured at R_{ax} = 3.90 m are compared between clockwise (solid lines) and counter-clockwise (dashed lines) B_t fields. The result is shown in Fig. 6.19. Similar to the previous result at R_{ax} = 3.75 m shown in Fig. 6.11, up-down asymmetry is also observed in the CV and CVI vertical profiles. The simulation result normalized at Z = 0 mm is denoted with dotted lines. The simulation shows a good agreement with the experiment when the value of $D_{Z\perp}$ = 4.0 m^2/s, which is 20 times larger than $D_\perp$ = 0.2 m^2/s, is adopted. Therefore, this indicates larger impurity cross-field transport in the R_{ax} = 3.90 m configuration. The large difference between the experiment and the simulation for CVI profiles originates in the same reason as the former result in Fig. 6.11.

6.5.3 2-D distribution of carbon line emissions

The 2-D distribution of carbon emissions is studied to deeply understand further detailed structural change in the edge carbon radiation during the plasma detachment phase. The 2-D distribution of CIII–VI is measured at the flattop during t = 6–8 s in Fig. 6.14 for attached plasmas without RMP and detached plasmas with 6-O and 7-O islands as well as the R_{ax} = 3.75 m case. The result is shown in Fig. 6.20. Trajectories of

inboard and outboard X-points and island O-point are indicated with dashed-dotted, long-dashed and dotted lines, respectively. The radial location of $\iota/2\pi = 1$ is also indicated with short-dashed line.

In the attached plasma without RMP, the CIII and CIV shown in Figs. 6.20 (a) and (d) are dominantly emitted in the top and bottom edges and the vicinity of outboard X-point denoted with long-dashed line. In contrast with $R_{ax} = 3.75$ m, the CIII and CIV are only enhanced along a trajectory parallel to the outboard X-point at the upper half region. The CV and CVI emissions are considerably uniform. In order to understand these 2-D distributions the simulation is done with EMC3-EIRENE for attached plasmas without RMP, as shown in Fig. 6.21. Two enhanced trajectories parallel to the outboard X-point appear in the simulation for CIII and CIV emissions shown in Figs. 6.21 (a) and (d), respectively. The upper trajectory in the simulation can be also seen in the measured CIII and CIV 2-D distributions [see Figs. 6.20 (a) and (d)], whereas the lower trajectory almost disappears in the measurement. Although the reason for the asymmetric trajectory observed in the experiment is now unclear, it strongly suggests the necessity of additional concern regarding the physical mechanism in the simulation, e.g., particle drift. The simulation of the CVI 2-D distribution in Fig. 6.21 (j) does not include the emission inside the LCFS as mentioned above.

The simulation is also carried out for three different impurity diffusion coefficients of $D_{Z\perp} = 0.2$, 1.0 and 4.0 m^2/s, as shown in Fig. 6.21. In order to determine the diffusion coefficient the CIV profile perpendicular to the X-point trajectory is compared between the measurement and the simulation. Here, the coordinate x perpendicular to the outboard X-point trajectory is defined as the reference point of (Y, Z) = (–100 mm, 100 mm), which is denoted by arrow in Fig. 6.21 (d). The measured perpendicular profile is plotted with simulated profiles in Fig. 6.22 as a function of x. The measured profile seems to be wide and the simulated profile is gradually wider as $D_{Z\perp}$ increases. Then, the experiment shows a good agreement with the simulated profile assumed $D_{Z\perp} = 4.0$ m^2/s. The impurity diffusion coefficient in the stochastic magnetic field layer obtained in the present analysis is 20 times bigger than the bulk ion diffusion coefficient which is obtained from radial density profile in the plasma edge.

In addition, it is clear in Fig. 6.21 that the length of the two outboard trajectories appearing in the 2-D distribution of CIII and CIV is sensitive to the diffusion coefficient. In order to explain why the length of two outboard trajectories changes against the diffusion coefficient, the poloidal distributions of magnetic field connection length, L_c, and simulated CIV emissivity at different toroidal angle, ϕ are plotted in Figs. 6.23 and 6.24, respectively. As the toroidal angle moves from the horizontally elongated plasma position at $\phi = 18°$ to the vertically elongated plasma cross section at $\phi = 0°$ or 36°, the magnetic field structure near outboard edge X-point becomes gradually asymmetric. The reason is explained in detail in Ref. [22]. One of the two divertor legs at the

outboard X-point tends to have longer L_c, i.e., upper divertor leg at $\phi = 9°$ and lower divertor leg at $\phi = 27°$ in Fig. 6.23.

The effect of impurity diffusion on the 2-D distribution of CIV is shown for two different $D_{Z\perp}$ of 0.2 and 4.0 m^2/s in Figs. 6.24 (a)–(c) and (d)–(f), respectively. The two arrows denote the vertical observation range. It is clearly shown that the CIV emissivity at outboard side is much stronger than at inboard side in the $R_{ax} = 3.90$ m configuration and the CIV distributes in radially wider region when the $D_{Z\perp}$ is large. If the $D_{Z\perp}$ is larger at the shorter L_c region in the vicinity of the outboard X-point, the radially diffused carbon ions immediately move toward the divertor plates and the emission intensity is resultantly weaker. The difference in the CIV emissivity between upper and lower sides of the outboard X-point is expressed in Figs. 6.24 (d) and (f) which correspond to the horizontal position of Y = –140 and 140 mm in the 2-D plot, respectively. In addition, the chord integration length in CIV emissions above (below) the outboard X-point is longer than that below (above) the outboard X-point at $\phi = 16°$ ($\phi = 20°$). Therefore, the carbon intensity near outboard X-point becomes different between upper and lower sides as explained above. As a result, the CIII and CIV emissions are weaker in upper X-point trajectory at Y = 140 mm and lower trajectory at Y = –140 mm as shown in Fig. 6.21, when the $D_{Z\perp}$ is large. We thus understand that the length of the X-point trajectory seen in Fig. 6.21 is a function of diffusion coefficient. When we compare the CIII distribution in Figs. 6.21 (a)–(c) with Fig. 6.20 (a) and the CIV distribution in Figs. 6.21 (d)–(f) with Fig. 6.20 (d), the simulation with $D_{Z\perp} = 4.0$ m^2/s also seems to have a good agreement with the experiment.

Although the reason why the cross-field impurity transport in the fully stochastic magnetic field layer is so large is unclear at present, the Larmor radius of partially ionized carbon ions is at least larger than that of protons as the bulk ion, i.e., $\rho(C^{2+})/\rho(p) = 1.7$ and $\rho(C^{3+})/\rho(p) = 1.15$. A magnetic field deformation due to the plasma pressure seems to be very important because the effect is enhanced in the plasma edge [33]. An anomalous transport may be also important. The blob can create a perpendicular convective flux near the X-point with velocities of 0.1–1 km/s in LHD which are clearly smaller than those of the blob in tokamaks, e.g., 2.5 km/s [34]. In addition, the direction of E×B force is frequently changeable in the stochastic magnetic field layer of LHD because the gradients of magnetic field strength and magnetic field curvature are considerably different due to the presence of helical ripple. Since the perpendicular CIV profile is symmetric as seen in Fig. 6.22, the particle drift does not seem to sufficiently contribute to the large impurity diffusion coefficient.

When the plasma detachment occurs by supplying the RMP, the CIII and CIV largely change their 2-D distributions and intensities. As shown in Figs. 6.20 (b), (c), (e) and (f), the CIII and CIV intensities are drastically large at the top and bottom edges

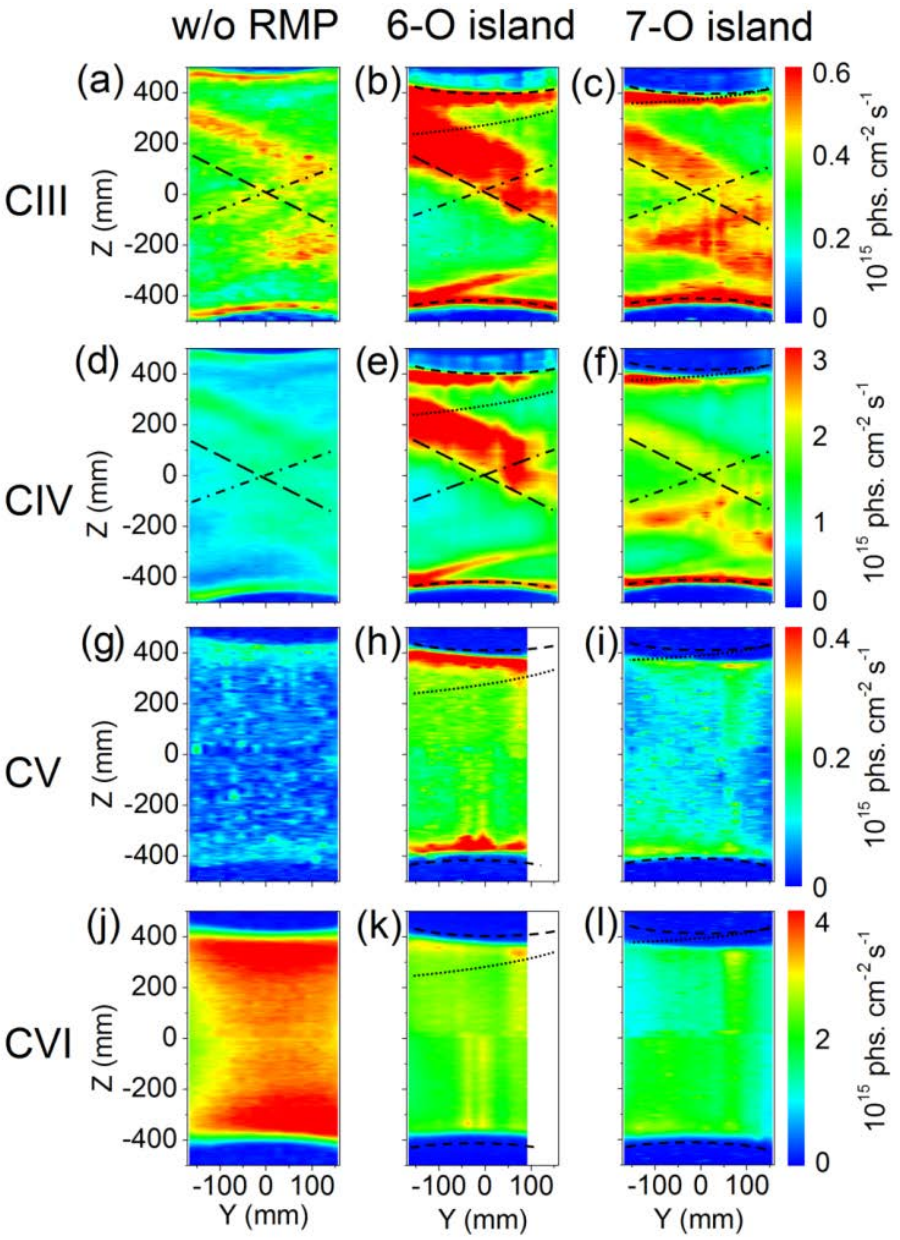

Fig. 6.20 2-D distributions of CIII (386.203 Å) at R_{ax} = 3.90 m in discharges (a) without RMP, (b) with 6-O island and (c) with 7-O island, CIV (384.174 Å) in discharges (d) without RMP, (e) with 6-O island and (f) with 7-O island, CV (40.27 Å) in discharges (g) without RMP, (h) with 6-O island and (i) with 7-O island and CVI (33.73 Å) in discharges (j) without RMP, (k) with 6-O island and (l) with 7-O island. Trajectories of outboard X-point, inboard X-point and island O-point are indicated with long dashed, dotted-dashed and dashed lines, respectively. The radial location of $\iota/2\pi = 1$ is indicated with dashed line.

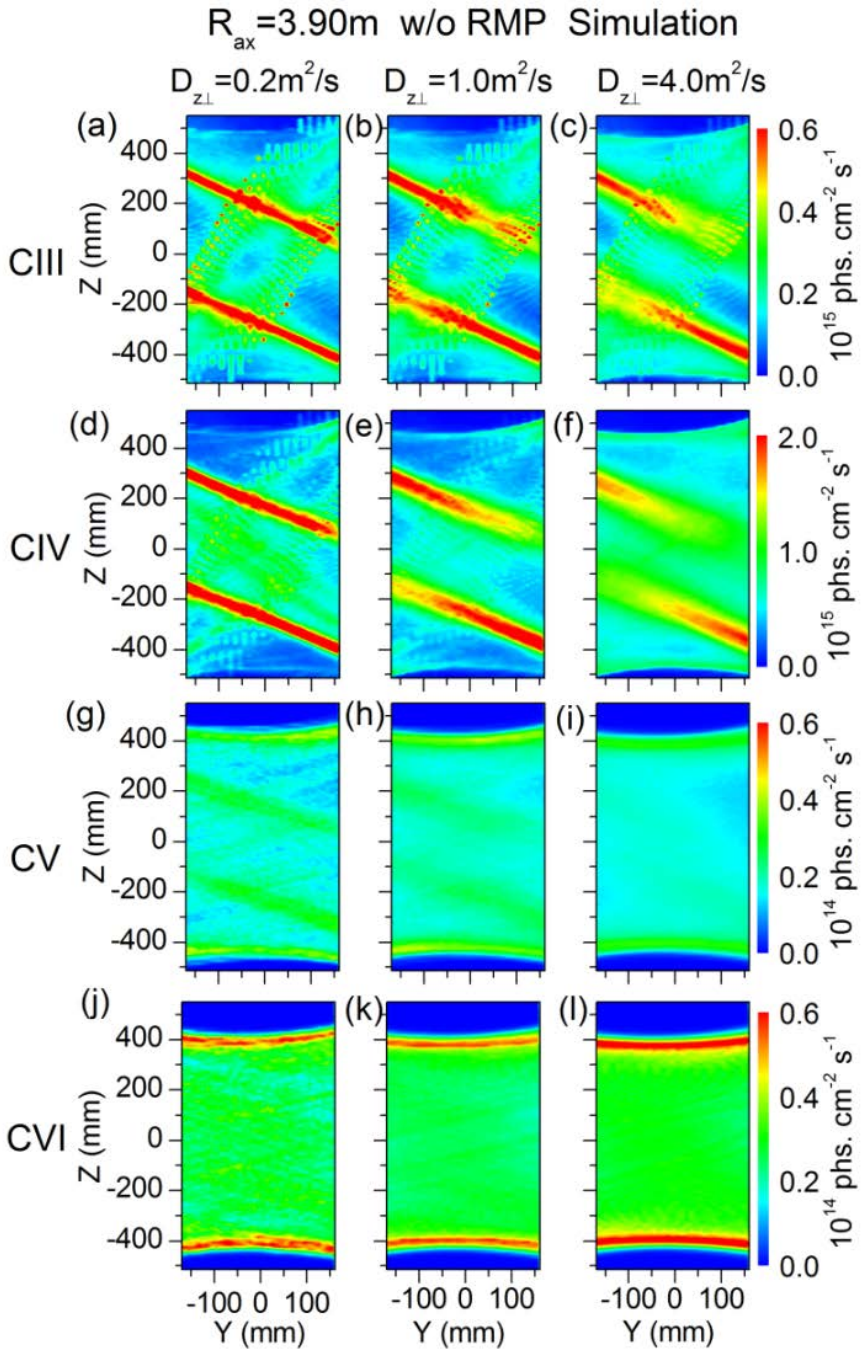

Fig. 6.21 2-D emissivity distributions simulated with EMC3-EIRENE in R_{ax}=3.90 m without RMP for (a) CIII (386.203 Å), (d) CIV (384.174 Å), (g) CV (40.27 Å) and (j) CVI (33.73 Å) at impurity diffusion coefficient of $D_{Z\perp}$ = 0.2 m^2/s, (b) CIII, (e) CIV, (h) CV and (k) CVI at $D_{Z\perp}$ = 1.0 m^2/s and (c) CIII, (f) CIV, (i) CV and (l) CVI at $D_{Z\perp}$ = 4.0 m^2/s. Trajectories of outboard and inboard X-point are indicated with long dashed and dotted-dashed lines, respectively. Coordinate x denoted in (d) defines direction perpendicular to the outboard X-point trajectory as a reference point of (Y, Z) = (–100 mm, 100 mm) on the trajectory.

and along the outboard X-point. In addition, the intensities also become stronger at the upper-left corner in each figure, and those areas are close to the island location for both the 6-O and 7-O islands [also see Figs. 6.18 (d) and (e)]. The island can enhance the edge carbon emissions, of which the result is similar to the CVI case in R_{ax} = 3.75 m [see Fig. 6.10 (f) and Fig. 12 (i)]. The result also suggests that the RMP can create a sufficiently large island even in the ergodic layer. In the case of R_{ax} = 3.90 m, however, a new emission trajectory parallel to the inboard X-point appears in the CIII and CIV 2-D distribution in the lower half of the figures. In particular, it is clear for the CIII distribution in Figs. 6.20 (b) and (c). This suggests that the magnetic field structure in the ergodic layer is considerably modified by the external RMP field. In contrast, the 2-D distributions of CV and CVI do not obviously change even in the detached plasma, while the CV emission is stronger in the plasma edge and CVI emission becomes weaker. The reduction of the CVI emission suggests an enhancement of the edge impurity screening as well as the result of R_{ax} = 3.75 m configuration.

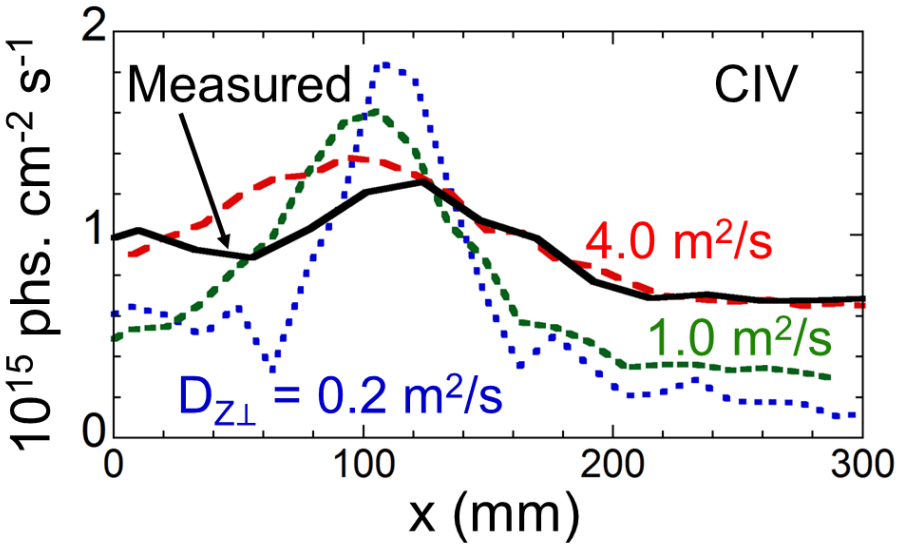

Fig. 6.22 Measured (solid line) and simulated CIV profiles as functions of x which is denoted in Fig. 6.21 (d). Simulations are carried out for three different impurity diffusion coefficients of $D_{Z\perp}$ = 0.2 (dotted line), 1.0 (short-dashed line) and 4.0 m^2/s (long-dashed line).

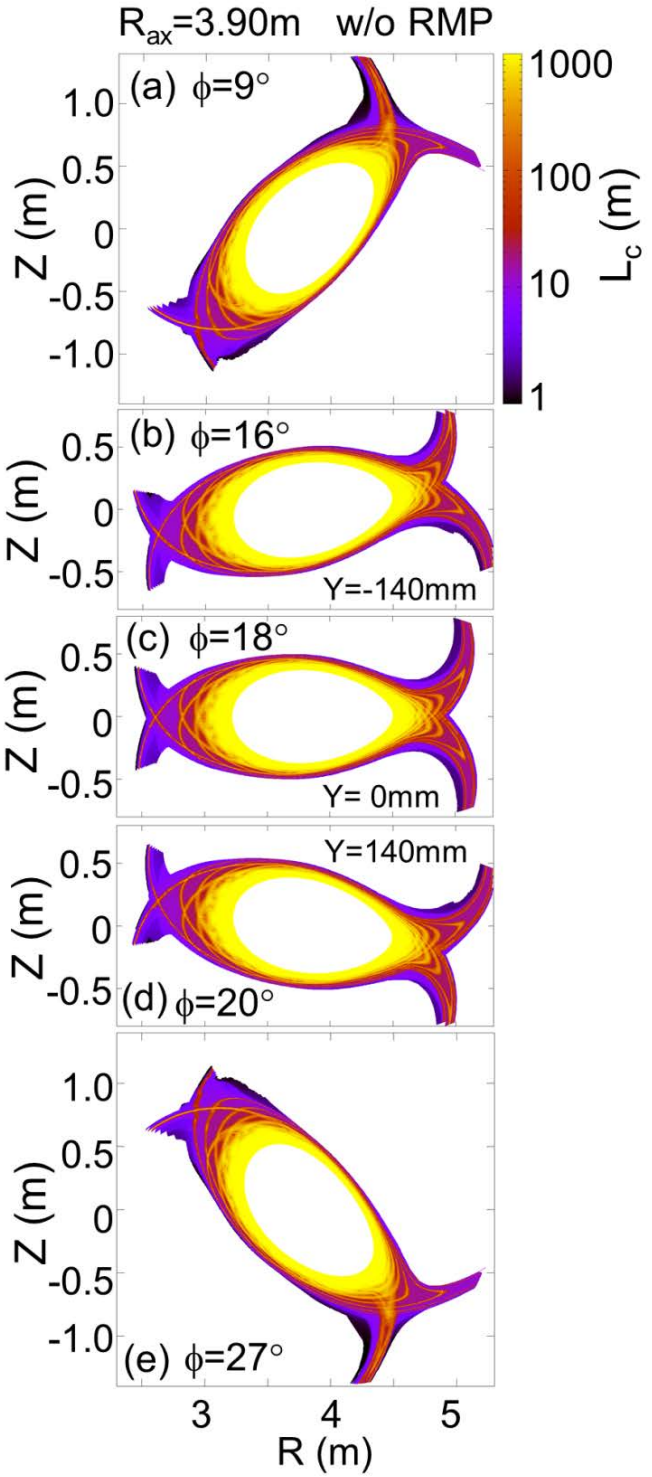

Fig. 6.23 Connection length, L_c, in the ergodic layer at R_{ax} = 3.90 m without RMP against five different toroidal angles of (a) ϕ = 9°, (b) ϕ = 16°, (c) ϕ = 18°, (d) ϕ = 20° and (e) ϕ = 27°. The poloidal cross section at toroidal angle of ϕ = 16°, 18° and 20° corresponds to the horizontal position of Y = –140 mm, 0 and 140 mm in the plot of 2-D distribution, respectively.

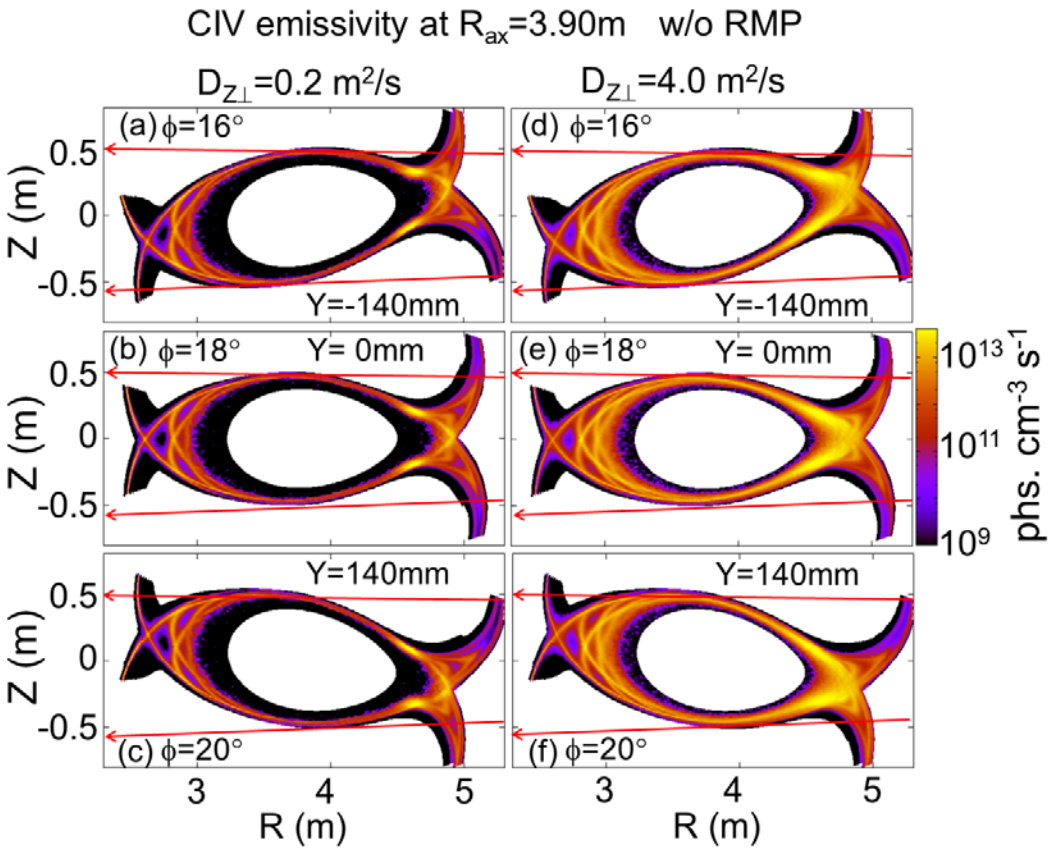

Fig. 6.24 Simulated poloidal distributions of CIV (384.174 Å) emissivity in the ergodic layer of R_{ax} = 3.90 m configuration without RMP at toroidal angle of (a) ϕ = 16°, (b) ϕ = 18° and (c) ϕ = 20° with impurity diffusion coefficient of $D_{Z\perp}$ = 0.2 m^2/s and (d) ϕ = 16°, (e) ϕ = 18° and (f) ϕ = 20° with $D_{Z\perp}$ = 4.0 m^2/s. Observation chords of EUV_Long2 spectrometer are indicated with arrows in each figure.

6.6 Summary

Vertical profiles and 2-D distributions of impurity carbon ions (CIII–CVI), from which the radiation is dominant in the plasma edge, have been studied in LHD to investigate the emission structure during RMP-assisted detachment and the effect of m/n = 1/1 magnetic island on the edge impurity distribution. The experiment is carried out in two different magnetic axis positions of R_{ax} = 3.75 m and 3.90 m in which the m/n=1/1 magnetic island is located in the edge of core plasma inside the LCFS and in the ergodic layer outside the LCFS, respectively. In the R_{ax} = 3.75 m configuration the CIV and CV emitted in the ergodic layer do not obviously change in supplying the RMP field as well as the intensities. The CVI mainly emitted inside the LCFS is enhanced only in the vicinity of the island O-point, while the intensity itself is decreased due to the enhanced impurity screening. Therefore, the formation of plasma detachment using the RMP field seems to be difficult in the case of R_{ax} = 3.75 m configuration because the effect of magnetic island is limited only in the edge region of the core plasma. The CIII-CVI emissions at R_{ax} = 3.75 m are simulated with 3-D edge plasma transport code, EMC3-EIRENE for attached plasmas without RMP because the code cannot treat the stochastic magnetic field layer with external magnetic field at present. These simulation results confirm that the poloidal distributions of CIII and CIV are entirely non-uniform enhancing the intensity in the vicinity of inner and outer X-points, whereas the CV and CVI intensities show a uniform poloidal distribution. It is also found that the cross-field impurity diffusion, $D_{Z\perp}$, is roughly 5 times larger than that of the bulk plasma ($D_{\perp}$ = 0.2 m^2/s) in the R_{ax} = 3.75 m configuration.

In the R_{ax} = 3.90 m configuration, on the other hand, the plasma detachment occurs when the m/n = 1/1 island is formed in the vicinity of the LCFS including the ergodic layer. It is found that the CIII and CIV are significantly enhanced in the vicinity of island O-point and both inboard and outboard edge X-points during the plasma detachment phase, while the CVI emission decreases due to the enhancement of edge impurity screening. 2-D distributions of carbon ions are also simulated with EMC3-EIRENE in the R_{ax} = 3.90 m configuration without RMP. The results confirm that the non-uniform poloidal distributions of CIII and CIV are enhanced in the vicinity of outboard X-points. Although two trajectories along the outboard edge X-point appear in the simulation, only a trajectory at upper side is observed in the experiment. It is also found that the impurity cross-field transport is more significant in the R_{ax} = 3.90 m configuration than that in the R_{ax} = 3.75 m configuration. The comparison of the 2-D distribution between the experiment and simulation gives the value of $D_{Z\perp}$ = 4.0 m^2/s for R_{ax} = 3.90 m. The simulation study with stochastic magnetic field structure taken the plasma pressure into account will be carried out in the near future in order to well explain the present experimental result.

References

[1] ITER Physics Basis. Chapter 4: Power and particle control, Nucl. Fusion, **39**, 2391 (1999).

[2] M. Shimada, D. J. Campbell, V. Mukhovatov, M. Fujiwara, et. al., Nucl. Fusion **47** S1–17 (2007).

[3] A. Loarte, B. Lipschultz, A. S. Kukushkin, et. al., Nucl. Fusion **47** S203–63 (2007).

[4] Y. Shimomura, M. Keilhacker, K. Lackner, et. al., Nucl. Fusion, **23**, 869 (1983).

[5] O. Gruber, A. Kallenbach, M. Kaufmann, et. al., Phys. Rev. Lett. **74**, 4217 (1995).

[6] F. Reimold, M. Wischmeier, M. Bernert, et. al., Nucl. Fusion **55**, 033004 (2015)

[7] T. W. Petrie, M. R. Wade, N. H. Brooks, et. al., J. Nucl. Mater. **363–365**, 416–420 (2007)

[8] T. Nakano, N. Asakura, H. Kubo, et. al., J. Nucl. Mater. **438**, S291–S296 (2013)

[9] A. Huber, S. Brezinsek, M. Groth, et. al., J. Nucl. Mater. **438**, S139-S147 (2013).

[10] B. Lipschultz, B. Labombard, J. L. Terry, et. al., Fusion Sci. Technol. **51** 369–89 (2007).

[11] N. Asakura, H. Hosogane, S. Tsuji-Iio, et. al., Nucl. Fusion **36**, 795 (1996).

[12] M. Kobayashi, S. Masuzaki, I. Yamada, et. al., Phys. Plasmas **17**, 056111 (2010).

[13] P. Grigull, K. McCormick, Y. Feng, et. al., J. Nucl. Mater. **313–316**, 1287 (2003).

[14] Y. Feng, F. Sardei, J. Kisslinger, et. al., Nucl. Fusion **45**, 89 (2005).

[15] S. Morita, C. F. Dong, M. Kobayashi, et. al., Nucl. Fusion **53**, 093017 (2013).

[16] C. F. Dong, S. Morita, M. Goto, et. al., Rev. Sci. Instrum. **81**,033107 (2010).

[17] E. H. Wang, S. Morita, M. Goto, et. al., Rev. Sci. Instrum. **83**, 043503 (2012).

[18] H. M. Zhang, S. Morita, T. Oishi, et. al., Jpn. J. Appl. Phys. **54**, 086101 (2015).

[19] M. B. Chowdhuri, S. Morita, M. Kobayashi, et. al., Phys. Plasmas **16**, 062502 (2009).

[20] A. Komori, H. Yamada, S. Sakakibara, et. al., Nucl. Fusion **49**, 104015 (2009).

[21] N. Ohyabu, T. Watanabe, H. Ji, et. al., Nucl. Fusion **34**, 387 (1994).

[22] S. Morita, E. H. Wang, M. Kobayashi, et. al., Plasma Phys. Control. Fusion **56,** 094007 (2014).

[23] M. B. Chowdhuri, S. Morita, M. Goto, et. al., Rev. Sci. Instrum. **78**, 023501 (2007) and Erratum: **84,** 109901 (2013).

[24] M. B. Chowdhuri, S. Morita and M. Goto, Appl. Opt. **47**, 135-146 (2008)

[25] T. Oishi, S. Morita, X. L. Huang, et. al., Plasma Fusion Res. **10**, 3402031 (2015).

[26] X. L. Huang, S. Morita, T. Oishi, et. al., Rev. Sci. Instrum. **85**, 043511 (2014).

[27] C. F. Dong, S. Morita, M. Goto, et. al., Rev. Sci. Instrum. **82**, 113102 (2011).

[28] Y. Feng, F. Sardei, J. Kisslinger, et. al., Contrib. Plasma Phys. **44**, 57 (2004).

[29] D. Reiter, M. Baelmans, and P. Boerner, Fusion Sci. Technol. **47**, 172 (2005).

[30] S. Y. Dai, M. Kobayashi, G. Kawamura, et. al., to be published on Contrib. Plasma Phys.
[31] S. Y. Dai, M. Kobayashi, G. Kawamura, et. al., Nucl. Fusion **56**, 066005 (2016).
[32] H. M. Zhang, S. Morita, T. Oishi, et. al., on Plasma Fusion Res. **11**, 2402019 (2016).
[33] Y. Suzuki, K.Y. Watanabe, H. Funaba, et al., Plasma Fus. Res. **4**, 036 (2009).
[34] H. Tsuchiya, T. Morisaki, V. P. Budaev, et al., Plasma Fusion Res. **5**, S2078 (2010).

Chapter 7

Summary

A space-resolved extreme-ultraviolet (EUV) spectrometer has been developed to study the edge impurity transport by measuring two-dimensional (2-D) distribution of impurity spectral lines emitted from stochastic magnetic field layer in which all the impurity ions have an entire non-uniform density distribution. The 2-D distribution can be measured by horizontally scanning the space-resolved spectrometer during 8–10 s at a steady phase in long pulse discharges. The full top-to-bottom 2-D distribution of impurity line emissions is completed by superimposing a few 2-D distributions measured at different vertical positions. In Large Helical Device (LHD), however, high-performance plasmas have been produced with high-power negative-ion-source-based NBI (n-NBI) at short-pulse operation of 2 s. Upgrade of the space-resolved EUV spectrometer system was then required for completing the 2-D distribution measurement within the short pulse length. The performance improvement of the spectrometer has been carried out by installing a high-frame-rate CCD and PET filter, increasing the horizontal scanning speed and adopting an intensity normalization method.

Since the high-frame-rate CCD can be operated with a relatively short sampling time of 50 ms for the 2-D measurement, the horizontal spatial resolution is significantly improved. With increase in the horizontal scanning speed, the 2-D distribution measurement is applicable to the NBI discharge with short pulse length. The intensity normalization method is adopted for data analysis of the 2-D distribution of impurity line emissions. For the purpose the temporal behavior of the same line emissions as the 2-D distribution measurement is measured with another EUV spectrometer with high-time resolution of 5 ms. A blurred image influenced by temporal intensity variation during a discharge and shot-to-shot intensity variation among two or three discharges becomes almost clear in the superimposed full 2-D distribution. A 0.5-μm-thick PET filter is installed in front of an entrance slit of the space-resolved EUV spectrometer to reduce the spike noise induced by high-energy neutral particles in NBI discharges. The PET filter can perfectly block the neutral particles originating in 40 keV positive-ion-source-based NBI (p-NBI) and also slightly change the direction of the neutral particles originating in 180 keV n-NBIs. As a result, the spike noise is almost eliminated from the EUV spectrum in the NBI discharges.

Thus, the 2-D intensity distribution of impurity line emissions in the stochastic magnetic field layer is excellently observed with good image quality for helium, carbon and iron, and a detailed structure of the 2-D distribution along X-point trajectory is also clearly observed in the NBI discharge. As mentioned above, the present upgraded system has shown a sufficient performance for the edge impurity transport study. In addition, the upgraded space-resolved EUV spectrometer system is necessary again for the absolute intensity calibration on the basis of the profile measurement of visible and EUV bremsstrahlung continua because several components including the CCD are fully modified. The calibration factor is then obtained as a function of wavelength in the range of 60–440 Å. As a result, it is confirmed that the calibration factor of the present upgraded system is basically identical to that of the original system.

A poloidal distribution of the local emissivity of impurity line emissions is evaluated by analyzing the 2-D distribution against magnetic flux surfaces geometrically extended outside last closed flux surface (LCFS), which are calculated with a three-dimensional (3-D) equilibrium code, VMEC. The inner and outer boundaries of the edge impurity locations are estimated from the vertical profile measured at different toroidal positions. The observation chord length passing through a poloidal emission contour is calculated on the basis of the radial thickness of the impurity emission location. The poloidal distributions of CIV, CVI, FeXV and FeXVIII with different ionization energies can be thus reconstructed into the local emissivity distribution. An entirely non-uniform poloidal distribution is obtained for the CIV emissivity, while the FeXVIII emissivity distribution is almost a function of the magnetic surface. It is experimentally confirmed that the poloidal distribution becomes gradually uniform as the ionization energy of impurity ions increases and the radial position of impurity ions moves from the ergodic layer toward the plasma core. The non-uniform poloidal distribution of the CIV emissivity is well explained by a simulation with three-dimensional (3-D) edge plasma transport code, EMC3-EIRENE.

A steadily sustained detached plasma has been achieved in LHD without external impurity gas feed by only supplying the resonance magnetic perturbation (RMP) field with m/n = 1/1 mode at outwardly shifted plasma axis position of R_{ax} = 3.90 m where the magnetic resonance exists in the stochastic magnetic field layer. Radiation power from intrinsically existing carbon ions is studied to clarify the physical mechanism triggering the RMP-assisted detachment. Resonance lines of CIII (977.02 Å, $2s2p–2s^2$), CIV (1548.2 Å, 2p–2s), CV (40.27 Å, $1s2p–1s^2$) and CVI (33.73 Å, 2p–1s) measured by vacuum ultraviolet (VUV) and EUV spectrometers are used to estimate the radiation power from C^{2+}–C^{5+} ions because the carbon is the most abundant impurity element in LHD. The partial carbon radiation at each ionization stage of C^{2+} to C^{5+} ions, $P_{rad}(C^{q+})$, is estimated from the absolute intensity of such resonance lines for attached and detached plasmas. In order to obtain the $P_{rad}(C^{q+})$, the ratio of the $P_{rad}(C^{q+})$ to the resonance line emissivity is calculated in advance as a function of electron temperature

using an ADAS atomic code. The electron temperature at a radial location where the carbon ion exists is determined from the line intensity ratio method. It is found that the P_{rad} (C^{3+}) localized near a radial location of $\iota/2\pi = 1$ in the stochastic magnetic field layer is much stronger than P_{rad} (C^{2+}), P_{rad} (C^{4+}) and P_{rad} (C^{5+}) for both the attached and detached plasmas. The P_{rad} (C^{3+}) extremely increases against the total radiation power, P_{rad}, during the plasma detachment phase, i.e., P_{rad} (C^{3+})/P_{rad} ~ 40%, while it is only 8% to the P_{rad} in the attached plasma. Therefore, the P_{rad} (C^{3+}) plays a key role in the enhancement of edge radiation during the RMP-assisted detached plasma phase.

In order to examine an effect of the RMP field on the edge impurity distribution at the plasma detachment, the vertical profile of edge impurity ions is measured during the plasma detachment phase with the space-resolved EUV spectrometer. It is found that the radial position of the top and bottom edge peaks appeared in both the CIII and CIV vertical profiles shifts radially inside after the detachment transition and the peak shift in the radial position is different between the top and bottom edges, while the CV and CVI position do not radially change at all even in the detachment phase. The sudden change in the top edge peak (ΔZ_{Top}) is much larger than that of the bottom edge peak (ΔZ_{Bottom}), i.e., ΔZ_{Top} ~ 80 mm and ΔZ_{Bottom} ~ 20 mm. The difference between ΔZ_{Top} and ΔZ_{Bottom} observed here indicates a clear evidence of newly appeared m/n = 1/1 magnetic island in the plasma edge during the plasma detachment phase. The result concludes that a big magnetic island can be created by the RMP field even if the magnetic resonance exists in the stochastic magnetic field layer.

The vertical profile and 2-D distribution of edge impurity carbon emissions of CIII to CVI are studied during the RMP-assisted plasma detachment phase. In particular, the 3-D structure of carbon ion distribution is carefully analyzed based on the measured 2-D distribution with magnetic field structure in the stochastic magnetic field layer. As a result, it is found that the CIII and CIV emissions in the stochastic magnetic field layer drastically increase near the island O-point and in the vicinity of both the inboard and outboard X-points during the RMP-assisted detachment phase, while those emissions are enhanced only in the vicinity of the outboard X-point in attached plasmas without RMP. The result clearly indicates an enhancement of edge carbon radiation and a considerable change in the magnetic field lines connecting to the divertor plates. The temperature flattening seen in the edge temperature profile, which suggests the appearance of a big magnetic island, can also support those experimental results. In contrast, the CVI emission located at radially inner side of the island entirely decreases the intensity during the detachment phase. It strongly suggests an enhancement of the impurity screening based on the density gradient force along magnetic field lines. The measured carbon 2-D distribution is also analyzed with EMC3-EIRENE for attached plasmas without RMP. It is found that the cross-field diffusion of carbon ions is about

20 times larger than that of the bulk ions in the stochastic magnetic field layer at R_{ax} = 3.90 m configuration. It may suggest a specific character of thicker stochastic magnetic field layer and effect of larger Gyro radius of partially ionized carbon ions compared to bulk hydrogen ions.

Acknowledgements

This thesis is completed on the basis of studying space-resolved EUV spectroscopy for 2-D distribution measurement in LHD at National Institute for Fusion Science (NIFS) during the past three years. I have gotten enormous helps from many people during the present work. I would like to express my sincere thanks and appreciations to all these people.

At first, I would like to express my earnest and most sincere gratitude to my supervisor, Prof. Shigeru Morita. I am very grateful to have the chance to learn EUV spectroscopy under the guidance of Morita-sensei. I have learned enormous valuable knowledges and skills in this field with his insightful suggestions and guidance in the past three years. In addition, I also have learned a lot of things from his scientific attitude as an experimental physicist. This thesis could be finished under his insightful instructions and patient promotion during the past three years. Furthermore, I am also very thankful for his generous help in my personal life in Japan. Without these helps, I could not concentrate my attention in the study. I have benefited for my whole life from his diligence and dedication in both work and life.

I am also extremely grateful to Prof. Motoshi Goto for his professional and considerable supports in acquisition work on spectral data during the experiment. I have also gotten a lot of valuable suggestions and comments from him about the data analysis. I am also deeply grateful to Dr. Tetsutarou Oishi and Dr. Xianli Huang who have kindly helped me in acquiring the spectral data and data analysis. Discussions with them could give me a lot of insights on the impurity transport study. I also very appreciate them for their helps in my personal life.

I am deeply grateful to Prof. Masahiro Kobayashi who has given me a lot of valuable suggestions and comments on the edge impurity distribution in detached plasmas. I am also thankful for Prof. Izumi Murakami for her help on the spectral intensity calculation using ADAS atomic code, with which one of the most import parts in the present thesis could be completed. I also express my thanks to Dr. Shuyu Dai for his help on the simulation of 2-D edge impurity distribution. I would also like to give my appreciation to Dr. Yoshiro Narushima for his help in calculation of magnetic field structures.

I heartily appreciate Dr. Hao Wang, Dr. Xiaodi Du and Dr. Haiying Fu, Dr Haishan Zhou and Dr. Tingfeng Ming for their supports and encouragements during the past there years. I am also very grateful to Mr. Shaofei Geng, Mr. Yue Xu, Mr. Hailin Bi, Mr. Takahiro Bando, Mr. Makoto Ohno, Mr. Xiang Ji, Mr. Liu Yang, Mr.

Theerasarn Pianpanit, Ms. Botz Huang, Ms. Zhijun Wang, Mr Gaowei Zhang and Mr. Junki Morimoto for their helps and friendships.

I wish to express my thanks to all members of LHD experimental group for their technical supports during experiments on the impurity transport study. I would also like to express my gratitude to all staffs of NIFS and SOKENDAI (the Graduate University for Advanced Studies) for their kind supports. I would like to express my special thanks to YUKWAI and Research Assistant system in NIFS for the financial supports which have been made on an ongoing basis during my PhD work over the past three years in Japan.

Finally, I wish to express my great gratitude to my parents and sisters. Empathically provided their supports and encourages could give me a great motivation to accomplish the present thesis work.

Publications

[1]. “Performance improvement of two-dimensional EUV spectroscopy based on high-frame-rate CCD and signal normalization method in Large Helical Device”
Hongming Zhang, Shigeru Morita, Tetsutarou Oishi, Motoshi Goto and Xianli Huang
Japanese Journal of Applied physics, **54** (2015) 086101.

[2]. “Evaluation of poloidal distribution from edge impurity emissions measured at different toroidal positions in Large Helical Device”
Hongming Zhang, Shigeru Morita Tetsutarou Oishi, Masahiro Kobayashi, Motoshi Goto and Xianli Huang
Plasma and Fusion Research, **10** (2015) 3402038.

[3]. “Estimation of total carbon radiation at each ionization stage of C^{2+} to C^{5+} ions in Large Helical Device”
Hongming Zhang, Shigeru Morita, Tetsutarou Oishi, Motoshi Goto and Xianli Huang
Plasma and Fusion Research, **11** (2016) 2402019.

[4]. “Application of a space-resolved EUV spectrometer to magnetic island observation during plasma detachment in stochastic magnetic field layer of LHD”
Hongming Zhang, Shigeru Morita, Tetsutarou Oishi, Motoshi Goto, Xianli Huang and Yang Liu
Submitted to Review of Scientific Instruments.

[5]. “Vertical profiles and two-dimensional structures of intrinsically existing carbon impurity in detached hydrogen plasmas assisted by RMP field of Large Helical Device”
Hongming Zhang, Shigeru Morita, Tetsutarou Oishi, Shuyu Dai, Masahiro Kobayashi, Gakushi Kawamura, Izumi Murakami, Yoshiro Narushima, Xianli Huang, Motoshi Goto and Yang Liu
Submitted to Physics of Plasmas.